



Giulia Simão Barreto de Sousa

**Development and characterization of
high-density polyethylene composites
reinforced with soapstone waste**

Dissertação de Mestrado

Thesis presented to the Programa de Pós-Graduação em Engenharia de Materiais e de Processos Químicos e Metalúrgicos da PUC-Rio in partial fulfillment of the requirements for the degree of Master em Engenharia Química e de Materiais.

Advisor: Prof. José Roberto Moraes d'Almeida

Rio de Janeiro
September 2021



Giulia Simão Barreto de Sousa

**Development and characterization of
high-density polyethylene composites
reinforced with soapstone waste**

Thesis presented to the Programa de Pós-Graduação em Engenharia de Materiais e de Processos Químicos e Metalúrgicos da PUC-Rio in partial fulfillment of the requirements for the degree of Master em Engenharia Química e de Materiais. Approved by the Examination Committee.

Prof. José Roberto Moraes d'Almeida

Advisor

Departamento de Engenharia Química e de Materiais –
PUC-Rio

Prof. Sidnei Paciornik

Decano

Centro Técnico Científico – PUC-Rio

Adib Kalantar Mehrjerdi, PhD

Faculdade de Têxteis, Engenharia e Negócios – Universidade de
Boras

Prof. Laura Hecker de Carvalho

Departamento de Engenharia de Materiais – UFCG

Rio de Janeiro, September the 10th, 2021

All rights reserved.

Giulia Simão Barreto de Sousa

Graduação em Engenharia Mecânica pela Universidade do Estado do Rio de Janeiro (UERJ) em 2019.

Ficha Catalográfica

Sousa, Giulia Simão Barreto de

Development and characterization of high-density polyethylene composites reinforced with soapstone waste / Giulia Simão Barreto de Sousa; advisor: José Roberto Moraes d'Almeida. – Rio de Janeiro: PUC-Rio, Department of Engenharia Química e de Materiais, 2021.

v., 148 f: il. color. ; 30 cm

Dissertação (mestrado) - Pontifícia Universidade Católica do Rio de Janeiro, Departamento de Engenharia Química e de Materiais.

Inclui bibliografia

1. Engenharia Química – Teses. 2. Engenharia de Materiais – Teses. 3. Pedra Sabão;. 4. Polietileno;. 5. Compósitos particulados;. 6. Propriedades mecânicas;. 7. Reologia;. I. d'Almeida, José Roberto M.. II. Pontifical Catholic University of Rio de Janeiro. Departamento de Engenharia Química e de Materiais. III. Título.

CDD: 620.11

Aos meus pais, Luís e Giuliana por todo carinho, apoio e incentivo. Vocês são meus maiores exemplos.

Aos meus irmãos, Gutinho e Felipe, pelo suporte e parceria. A vida teria muito menos graça sem vocês.

A minha segunda mãe, Nete, por ter ajudado a me criar com tanto amor e carinho. Devo muito do que eu sou a você.

Aos meus amigos, em especial Juliana, Carolina, Anna e Lucas X. por estarem do meu lado nos momentos mais importantes. Vocês são parte de mim.

A Bruno, por tanto apoio e pela leveza que você traz. A vida é muito mais bonita com você.

Acknowledgments

I would like to first thank my advisor for all the patience and incentive given over the elaboration of this work.

I would also like to thank all the colleagues that were essential for the elaboration of this work. Specially professor Sidnei Paciornik and PhD students Geovane Almeida, Camila Souza and Bruno Jordão.

This study was financed in part by the Coordenação de Aperfeiçoamento de Pessoal de Nível Superior - Brasil (CAPES) - Finance Code 001.

This study was financed in part by the National Council for Scientific and Technological Development (CNPq) [grant number 158192/2019-2].

Abstract

Sousa, Giulia Simão Barreto de; d'Almeida, José Roberto M. (Advisor). **Development and characterization of high-density polyethylene composites reinforced with soapstone waste.** Rio de Janeiro, 2021. 148p. Master's Thesis – Department of Engenharia Química e de Materiais, Pontifical Catholic University of Rio de Janeiro.

A novel sustainable material was developed using a mineral waste as filler for polymeric composites. Soapstone is a mineral typically found in abundance in communities that rely heavily on artisanal crafts as a source of income and which are often in a situation of social vulnerability. Rock recovery in those activities is low and the waste disposal is done with little control, which can be hazardous to the environment and the health of the local residents. Thus, to use this residue to reinforce the properties of a polymer with a wide range of applications, such as polyethylene, can lead to positive economical, social and environmental returns. A thorough characterization of the residue was done with automated image analysis, X-ray diffraction, infrared, and Raman spectroscopy. The waste particles were incorporated into a high-density polyethylene (HDPE) matrix in three compositions: 10, 20 and 30 wt%. X-ray microtomography was used to quantify the filler volume fraction, void content, and the microstructural homogeneity of the composites. It was found that the soapstone particles have a strong tendency of forming clusters in the HDPE matrix, however, statistical analysis revealed that the volumetric filler distribution was homogeneous throughout the samples. Rheological, tensile and creep tests assessed the influence of the particles on the polymer's processing conditions and practical mechanical behavior. A relevant increase in viscosity and shear stress was observed at lower shear rates for higher filler loadings. The addition of soapstone waste particles successfully decreased creep strain and increased both yield strength and elastic modulus of HDPE. However, the incorporation of higher amounts of filler altered the fracture mechanism and considerably decreased ductility and creep rupture time of the polymer. The relationship between the microstructure and the macroscopic mechanical behavior was investigated by fitting tensile test data with macro-mechanical models from the literature, which allowed the quantification of the interfacial bonding.

Keywords

Soapstone waste; Polyethylene; Particulate composites; Mechanical properties; Rheology;

Resumo

Sousa, Giulia Simão Barreto de; d'Almeida, José Roberto M.. **Desenvolvimento e caracterização de compósitos de polietileno de alta densidade reforçados com resíduos de pedra sabão**. Rio de Janeiro, 2021. 148p. Dissertação de Mestrado – Departamento de Engenharia Química e de Materiais, Pontifícia Universidade Católica do Rio de Janeiro.

Um novo material sustentável foi desenvolvido utilizando um resíduo mineral como carga para compósitos poliméricos. A pedra-sabão é um mineral extensamente utilizado na fabricação de artesanato e manufaturas, atividades que representam a maior fonte de renda em comunidades marcadas por vulnerabilidade social. Estas atividades geram uma quantidade considerável de resíduos, que muitas vezes são descartados de forma indevida, causando danos ao meio ambiente e à saúde dos habitantes. Portanto, utilizar esse resíduo para reforçar um polímero com ampla gama de aplicações como o polietileno, pode promover ganhos econômicos, sociais e ambientais. A caracterização do resíduo foi feita com análise de imagens, difração de raios-X e espectroscopia de infravermelho e Raman. Partículas de resíduo foram incorporadas à uma matriz de polietileno de alta densidade (PEAD) em três proporções em peso: 10, 20 e 30%. Microtomografia de raios-X foi utilizada para quantificar as frações volumétricas de carga e de vazios, e a homogeneidade microestrutural dos compósitos. Foi observado que as partículas de pedra-sabão tendem a formar aglomerados na matriz de PEAD. Entretanto, análises estatísticas revelaram uma distribuição volumétrica de carga homogênea nas amostras. Ensaio de reologia, tração e fluência avaliaram a influência das partículas nas condições de processamento e no comportamento mecânico do polímero. Em taxas pequenas de cisalhamento, houve um aumento relevante de viscosidade e tensão cisalhante para concentrações altas de carga. A adição das partículas reduziu a deformação por fluência e aumentou de forma efetiva a tensão de escoamento e o módulo elástico do PEAD. No entanto, a incorporação de frações maiores de carga alterou o mecanismo de fratura e diminuiu consideravelmente a ductilidade do polímero. A relação entre a microestrutura e o comportamento macroscópico foi investigada através do ajuste numérico de pontos experimentais a modelos macro mecânicos da literatura, o que permitiu uma quantificação da adesão interfacial.

Palavras-chave

Pedra Sabão; Polietileno; Compósitos particulados; Propriedades mecânicas; Reologia;

Table of contents

1	Introduction	18
2	Literature Review	21
2.1	Soapstone	21
2.1.1	Production	23
2.1.2	Characterization	25
2.2	Polyethylene	31
2.2.1	High Density Polyethylene	33
2.3	Particulate Polymer Composites	35
2.3.1	Rheological Behavior	36
2.3.2	Mechanical Behavior	42
2.3.3	Creep Behavior	50
2.4	Mechanical Models for Polymeric Composites	57
2.4.1	Tensile Properties	58
2.4.1.1	Theories for Young's Modulus	58
2.4.1.2	Theories for Strength	61
2.4.2	Viscoelastic Models	65
2.5	Characterization Techniques	70
2.5.1	Particle Analysis	71
2.5.1.1	Automated Image Analysis	74
2.5.2	X-Ray Diffraction	76
2.5.2.1	Talc Crystallographic Data	78
2.5.3	FTIR and Raman Spectroscopy	79
2.5.3.1	Soapstone Infrared and Raman Bands	84
2.5.3.2	HDPE Infrared and Raman bands	86
2.5.4	X-Ray Microtomography	88
2.5.4.1	Microstructural parameters	92
3	Experimental	94
3.1	Materials	94
3.2	Methods	95
3.2.1	Filler Characterization	95
3.2.2	Preparation of Composites	96
3.2.3	Composites Characterization	97
4	Results	101
4.1	Filler Characterization	101
4.1.1	Particle Analysis	101
4.1.2	X-ray Diffraction	103
4.1.3	Spectroscopy of the Soapstone Powder	105
4.2	Composites Characterization	107
4.2.1	Spectroscopy	107
4.2.2	Rheology	110
4.2.3	X-ray Microtomography	112

4.2.4	Tensile Tests	121
4.2.5	Creep Tests	126
5	Conclusions	132
A	Statistical Analysis	145
A.1	Test of Homogeneity: variability of reinforcement on composites	145
A.2	One-way ANOVA: differences between mechanical properties	146
A.3	One-way ANOVA: differences between creep rates	147

List of figures

Figure 2.1	Crystalline structure of the talc mineral [24, 25].	22
Figure 2.2	Major Brazilian deposits of talc, including soapstone. Adapted from [5].	24
Figure 2.3	XRD of the soapstone waste from Congonhas, MG [7].	26
Figure 2.4	Cumulative particle size distribution of soapstone residue from Bandeiras, MG [5].	28
Figure 2.5	XRD patterns of talc samples, curve 1 - unground sample, curve 2 - ground sample [34].	29
Figure 2.6	SEM micrographs of (a) unground and (b) ground talc samples [34].	29
Figure 2.7	Results of DTA and TG of talc samples measured during heating and subsequent cooling in air - unground sample [34].	30
Figure 2.8	Results of DTA and TG of talc samples measured during heating and subsequent cooling in air - ground sample [34].	30
Figure 2.9	(a) SEM image of talc platelets obtained from an unpol- ished soapstone after mechanical scraping. SEM magnification 1000 x. (b) Size distribution of talc platelets [35].	31
Figure 2.10	X-ray spectrum of talc platelets from unpolished soap- stone [35].	31
Figure 2.11	Polyethylene structure [37].	32
Figure 2.12	Shear viscosity as a function of shear rate for talc-HDPE compounds at 160°C [48].	38
Figure 2.13	Thermogravimetric analysis of HDPE/talc composites [43].	39
Figure 2.14	Apparent shear viscosity of HDPE-talc composites as a function of the apparent shear rate at varying filler concentra- tions [43].	40
Figure 2.15	Apparent shear viscosity of HDPE/talc composites as a function of the filler content at varying temperatures and loads [43].	40
Figure 2.16	The comparison of shear stress and apparent shear rate of neat HDPE and HDPE/talc composite for 10 %wt. talc under 190 and 220 °C in logarithm scale [43].	41
Figure 2.17	Effects of the talc concentration on the die swell of HDPE at varying loads (190 °C) [43].	42
Figure 2.18	Effects of the talc content on the die swell of HDPE at different temperatures (load 12.16 kg) [43].	42
Figure 2.19	General photograph of the post extrudate: (a) composite with 15 wt% talc at 190 °C/5 kg load and (b) HDPE base material at 220 °C/12.16 kg load [43].	43
Figure 2.20	Evolution of (a) deformation at break and (b) ultimate tensile strength of HDPE/talc composites as a function of talc content [52].	44

Figure 2.21 (a) Particle size distribution and (b) micrograph of commercial talc HAR T84 from Luzenac, France used in the HDPE composites [13].	45
Figure 2.22 Tensile strength at yield and at break for talc-filled HDPE/CB composites [13].	45
Figure 2.23 Mechanical properties of the HDPE/talc composites as a function of filler and treatment: (a) Tensile strength (b) Elongation at break [14].	46
Figure 2.24 Elastic modulus of the HDPE/talc composites as a function of filler and treatment [14].	47
Figure 2.25 Void content as function of filler treatment in the HDPE/talc composites [14].	47
Figure 2.26 SEM morphologies of the talcs under 1kx of magnification (a) TN, (b) NTC and (c) NTA [53].	49
Figure 2.27 XRD patterns of natural microtalc (TN), semi-crystalline synthetic nanotalc (NTC) and amorphous synthetic nanotalc (NTA) used in the HDPE composites [53].	50
Figure 2.28 Typical creep curve of strain versus time at constant load. The minimum creep rate $\Delta\epsilon/\Delta t$ is the slope of the linear segment in the secondary region. Rupture time t_r is the total time to rupture [37].	51
Figure 2.29 Schematic illustration of the four types of creep rupture behaviour in HDPE [59].	53
Figure 2.30 Schematic of the molecular alignment during cold drawing of a semicrystalline polymer. The strong alignment of the tie chains is highlighted. [60].	53
Figure 2.31 (a) Morphology of the air-cooled specimens, degenerated spherulites are indicated by arrowheads. (b) Morphology of the water-quenched specimens [59].	54
Figure 2.32 Strain vs. time curve for one of the specimens HDPE tested by Silva [61].	55
Figure 2.33 Compliance comparison between as-received and aged HDPE [62].	56
Figure 2.34 Fitting of the Nielsen equation for the relative modulus vs. filler concentration for: + Noryl-talc; \square ABS-talc, \diamond PP-SiC, \times modified PP-aluminum flake, \triangle PP-aluminum flake, \blacktriangle PP-steel fibers [49].	60
Figure 2.35 Fitting for the relative tensile strength of polymers with non-metallic fillers. + Noryl-talc, \square ABS-talc, \diamond PP-SiC [49].	63
Figure 2.36 Fitting procedure for HDPE composite: (o) atapulgite, (\triangle) atapulgite + silane, (\square) CaCO ₃ , (*) sisal [51].	64
Figure 2.37 Standard Linear Solid Model schematic representation [76].	66
Figure 2.38 Burgers Model schematic representation [76].	67

Figure 2.39 Comparison between the viscoelastic models and the creep test experimental strain-time data (in blue) for one HDPE specimen. In red the Three Parameters model, in black the Four Parameters model and in yellow the Stretched Burgers model [61].	69
Figure 2.40 Comparison between the viscoelastic models for the HDPE specimens as received and after aging in oil derivatives [62].	70
Figure 2.41 Cumulative distribution. Adapted from [79].	72
Figure 2.42 Histogram of a density distribution. Adapted from [79].	72
Figure 2.43 Density distribution. Adapted from [79].	73
Figure 2.44 Example of number and volume particle size distributions for the same sample. Adapted from [82].	73
Figure 2.45 Conversion of a particle image into a 2D binary projection for size and shape analysis [82].	74
Figure 2.46 Illustration of length and width on a needle shaped particle image [82].	75
Figure 2.47 Diagram of an object (area A) and its corresponding convex hull (area B) [82].	75
Figure 2.48 X-ray diffraction on a crystal [37].	76
Figure 2.49 X-ray powder diffractometer (scanning type): principle of finding the diffracted intensity at Bragg angle [86].	77
Figure 2.50 Monoclinic crystalline system. Adapted from [89].	78
Figure 2.51 Theoretical X-ray diffractogram of talc [24, 25].	79
Figure 2.52 X-ray diffractogram of talc mineral from Murphy, North Carolina, USA [90].	80
Figure 2.53 Portion of the electromagnetic spectrum [94].	81
Figure 2.54 Simple modes of vibrational motion in a molecule [94].	81
Figure 2.55 Schematic illustration of Raman and Rayleigh scattering and infrared absorption [95].	83
Figure 2.56 Example: complementary infrared and Raman spectra of chloroform [95].	84
Figure 2.57 Raman spectrum of talc crystal (a) in the 1200 cm^{-1} to 0 cm^{-1} region and (b) in the low-frequency lattice and OH stretch regions with expanded scale [21].	85
Figure 2.58 Infrared spectrum (attenuated total reflectance) of talc mineral from the RUFF database [90].	86
Figure 2.59 Raman spectrum (785 nm laser) of talc mineral from the RUFF database [90]. Unoriented sample.	87
Figure 2.60 Comparison of FTIR spectra obtained in transmission and ATR modes of plastics: polycarbonate (PC), polyethylene (PE), polyethylene terephthalate (PET), polypropylene (PP), polystyrene (PS), polysulfone (PSu), Polytetrafluoroethylene (PTFE), and polyvinyl chloride (PVC) [98]	89
Figure 2.61 FTIR analysis of two polyethylene samples, asphalt binder and binder blends [99].	89
Figure 2.62 Schematic illustration of X-ray CT acquisition and reconstruction process. [100]	90

Figure 2.63	Illustration of the incident and acquired X-ray represented as a ray passing through the object. (a) the acquired intensity $I(x,z)$ is modeled as a line integral of X-ray absorption along the ray path. Total absorption along the path is calculated through measurements of both I_0 and I . (b) to (d) show images that illustrate the stage of X-ray absorption measurement. (b) is a map of $I(x,z)$, (c) is a map of I_0 and (d) is the corrected radiograph, $\tau(x,z)$, calculated using Eq. (2-34) [100]	91
Figure 3.1	(a) HDPE pellets and (b) soapstone waste powder used in this work.	94
Figure 3.2	Schematics of the characterization techniques utilized in this work.	95
Figure 3.3	(a) Automated image analysis equipment and (b) interior of the equipment showing the dispersed powder after the analysis.	96
Figure 3.4	(a) Extruder and (b) injection molding machine used to produce the composite specimens.	97
Figure 3.5	(a) Mold used in the composites production and (b) composite specimens with three compositions after production.	97
Figure 3.6	Micro CT used to characterized the composites microstructure.	98
Figure 3.7	70/30 sample positioned in the micro CT rotation stage.	98
Figure 3.8	Parallel plate rheometer used for rheology tests.	99
Figure 3.9	Testing machine used for tensile and creep tests.	99
Figure 4.1	Particle size of the soapstone waste powder: (a) number distribution and (b) histogram of CE diameter.	101
Figure 4.2	Particle size of the soapstone waste powder: histogram of SE volume.	102
Figure 4.3	Particle shape of the soapstone waste powder: histogram of (a) HS circularity and (b) Feret ratio.	103
Figure 4.4	Example: soapstone particle and the corresponding values for the size and shape parameters measured.	103
Figure 4.5	X-ray spectrum of the soapstone waste. Talc peaks identified with the corresponding diffraction angle.	104
Figure 4.6	FTIR-ATR spectrum of the soapstone waste.	106
Figure 4.7	Raman spectrum of the soapstone waste.	106
Figure 4.8	FTIR-ATR spectrum of the HDPE pellets used to manufacture the composites.	107
Figure 4.9	FTIR-ATR spectrum of the 70/30 composites.	109
Figure 4.10	Comparison between the FTIR-ATR spectra of the 70/30 composites, the HDPE pellets and the soapstone filler.	109
Figure 4.11	Viscosity versus shear rate curves in logarithm scale.	110
Figure 4.12	Shear stress versus shear rate curves logarithm scale.	112
Figure 4.13	2D slice 70/30 sample showing the pixel intensity histogram (a) before and (b) after the application of the Non-Local Means filter.	113
Figure 4.14	2D slice 70/30 sample (a) before and (b) after pre-processing.	113

Figure 4.15 Segmentation of (a) particles (in green) and (b) voids (in red) in the 70/30 sample. The polymer matrix is shown only on the bottom half in gray color.	114
Figure 4.16 3D rendering of 90/10 composite sample. Images show the particles colored according to (a) volume and (b) mean feret diameter scales. The polymer matrix is shown only on the bottom half in gray color.	115
Figure 4.17 3D rendering of 80/20 composite sample. Images show the particles colored according to (a) volume and (b) mean feret diameter scales. The polymer matrix is shown only on the bottom half in gray color.	116
Figure 4.18 3D rendering of 70/30 composite sample. Images show the particles colored according to (a) volume and (b) mean feret diameter scales. The polymer matrix is shown only on the bottom half in gray color.	117
Figure 4.19 3D rendering with orthogonal views of the 70/30 composite sample. Voids identified in the central region of the sample.	118
Figure 4.20 Mean feret diameter histograms of the soapstone filler identified in (a) 90/10, (b) 80/20 and (c) 70/30 samples, respectively.	119
Figure 4.21 3D rendering of a composite sample divided into twelve equal-sized subsets. The particles are colored according to the nomenclature.	120
Figure 4.22 Stress-strain curves of a representative specimen of each material (HDPE and 90/10, 80/20 and 70/30 composites).	122
Figure 4.23 (a) Yield and (b) tensile strength box-plots.	123
Figure 4.24 (a) Strain to failure and (b) tenacity box-plots.	123
Figure 4.25 Relative E modulus versus filler content of the HDPE/soapstone composites. Error bars represent the 95% confidence interval.	124
Figure 4.26 Yield tensile strength versus filler content of the HDPE/soapstone composites.	126
Figure 4.27 Specimens of each composition after creep testing.	128
Figure 4.28 Strain-time curves for (a) neat HDPE, (b) 90/10, (c) 80/20 and (d) 70/30 composites. The * symbol was use to indicate that the specimen did not ruptured.	129
Figure 4.29 Example of determination of the stationary creep region: (a) strain-time curve and (b) first derivative of the strain-time curve indicating the time range in which the creep rate was stationary.	130

List of tables

Table 2.1	Distribution of the Brazilian market of talc and pyrophyllite [29].	23
Table 2.2	World mine production and reserves of talc [28].	25
Table 2.3	Particle size distribution of soapstone waste obtained in Congonhas, MG [7].	26
Table 2.4	Density and surface area of soapstone from Cachoeira do Brumado e Bandeiras, MG [23].	26
Table 2.5	Particle size distribution of soapstone from Cachoeira do Brumado e Bandeiras, MG [23].	27
Table 2.6	Minerals identified in the XRD of the soapstone form Cachoeira do Brumado, MG [23].	27
Table 2.7	Minerals identified in the XRD of the soapstone form Bandeiras, MG [23].	27
Table 2.8	Comparison between HDPE and LDPE characteristics [38].	33
Table 2.9	HDPE properties [38].	34
Table 2.10	Mechanical properties of linear HDPE, Ziegler HDPE and LDPE [38].	34
Table 2.11	Thermal degradation and residue for HDPE/talc composites [43].	39
Table 2.12	Mechanical Properties of Talc/CB HDPE Composites [13].	45
Table 2.13	Mechanical properties of HDPE/talc composites [53].	49
Table 2.14	Mean creep rate obtained for HDPE under 118N constant load at room temperature [61].	55
Table 2.15	Rates of steady-state creep for as-received and aged HDPE [62]	56
Table 2.16	Materials and conditions used for the experimental creep test [57]	57
Table 2.17	Shape Factors for Several Filler Type [49].	59
Table 2.18	Maximum packing fraction of selected fillers [49].	60
Table 2.19	Calculated Coefficients for Upper and Lower Bound Equations [49].	62
Table 2.20	Ultimate tensile strength (MPa) of HDPE particulate composites [51].	64
Table 2.21	Values of the parameters adjusted to the modified eq. 2-15 for HDPE [51].	65
Table 2.22	Parameters obtained for the viscoelastic models for the HDPE specimens [61].	68
Table 2.23	Parameters obtained for the viscoelastic models for the HDPE specimens [62].	69
Table 2.24	Values of the lattice constants and β angle for talc [24, 88].	78
Table 2.25	Raman and infrared peaks of talc mineral [21].	85
Table 2.26	Lattice Modes of n-alkanes and polyethylene for the orthorhombic structure [96].	87

Table 2.27	Experimental and calculated frequencies of polyethylene for the orthorhombic structure [96].	88
Table 3.1	Properties of the HDPE used in this work [103]	94
Table 3.2	Creep tests setting.	100
Table 4.1	Shape parameters of the soapstone particles.	102
Table 4.2	Talc peaks detected in the soapstone X-ray spectrum and the corresponding theoretical values.	104
Table 4.3	Observed FTIR and Raman bands in the soapstone spectra and their assignments.	105
Table 4.4	Comparison of the observed FTIR bands on the filler, matrix and composites and their assignments.	108
Table 4.5	Values for the coefficients of the power law for each composite.	112
Table 4.6	Size measurements of soapstone particles identified in different HDPE composite samples. (Uncertainties represent the standard deviation).	114
Table 4.7	Classification of the soapstone particles in different HDPE composite samples.	118
Table 4.8	Particle clustering parameters, void and filler content of the composite samples.	120
Table 4.9	Comparisons between local fractions and the total volume fraction of particles of the composite samples.	121
Table 4.10	Mechanical properties of unfilled and filled HDPE specimens determined by the tensile test.	123
Table 4.11	Creep test conditions.	126
Table 4.12	HDPE specimens creep response under constant load of 132N, at room temperature (23 ± 2 °C).	127
Table 4.13	Mean strain to failure and rupture time for the HDPE/soapstone composites. (Uncertainties indicate the standard deviation).	129
Table 4.14	Mean steady creep rate in the 1h-2h interval for each composition. (Uncertainties represent the standard deviation).	130
Table A.1	Two-way tables for the local volume fraction of particles in each composite sample.	146
Table A.2	Test of homogeneity considering the fraction of particles in subset (ξ_p^{sub}) as measurement of filler distribution.	146
Table A.3	Test of homogeneity considering the local volume fraction of particles (Φ_p^{sub}) as measurement of filler distribution.	146
Table A.4	One-way ANOVA results: significance of difference between the mean mechanical properties. Degrees of freedom between groups: 3; degrees of freedom within groups: 28.	147
Table A.5	Creep rate values for each specimen of each composition. Degrees of freedom between groups: 3; degrees of freedom within groups: 28.	147

List of Abbreviations

ABS - acrylonitrile-butadiene-styrene
ATR - attenuated total reflection
CB - carbon black
CT - computed tomography
DTA - differential thermal analysis
FTIR - Fourier-transform infrared spectroscopy
HA - hydroxyapatite
HDPE - high density polyethylene
HS circularity - High Sensitivity circularity
KV - Kelvin-Voigt Model
LDPE - low density polyethylene
LLDP – linear low density polyethylene
NTA - amorphous synthetic nanotalc
NTC - semi-crystalline synthetic nanotalc
PA12 - polyamide 12
PE - polyethylene
PMMCs - particulate polymer matrix composites
PP - polypropylene
RHDPE - recycled high-density polyethylene matrix
SEM - scanning electron microscopy
SW - soapstone waste
TG - thermogravimetry
TN - natural microtalc
UHMWPE – ultra high molecular weight polyethylene
ULDPE– ultra low density polyethylene
XRD - X-ray diffraction

1 Introduction

Nowadays, one of the main challenges in materials science is to counterbalance the need for environmental preservation with the global industry demands. Due to their non-biodegradable alkaline nature and their highly wasteful exploitation and production processes, stone waste is generally considered as a highly polluting waste, that can represent a health hazard and an environmental issue [1]. Accordingly, there is a growing scientific interest in using such waste materials as alternative fillers for polymeric materials [2]. Fillers are often incorporated into polymers in order to reduce costs and/or improve required properties for specific applications. Recent studies reveal a growing tendency of substituting commercial standard fillers for industrial or mineral waste particulates, which can bring both economic and environmental advantages [1, 2, 3].

The soapstone is a soft, metamorphic rock existent in various geological environments and used for both ornamental and construction purposes [4, 5]. The soapstone gradually changes over long periods of time, in the presence of carbon dioxide and water (carbonation), from hard dense serpentine to talc-rich steatite [6]. The composition of the soapstone can vary depending on the region and on the geological formation that took place, but according to the definition proposed by Huhta and Kärki [4], to be classified as soapstone the rock must contain between 35% and 75% of talc mineral and less than 35% of hard silicates (such as olivine, pyroxene, serpentine and amphiboles).

In Brazil, the major production of this mineral occurs in the Ouro Preto region of Minas Gerais state and the main destination of the soapstone is in local production of craftsmanship, vases and other decorating utensils [7]. These activities are linked with social development, since they are the main source of income in many local families [8]. However, they also generate a considerable amount of waste (approximately 10%-15% rock recovery), which is disposed carelessly, often causing environmental problems [5]. In fact, there are studies that associate the talc dust inhalation to diverse patterns of irreversible pulmonary diseases amongst humans and animals [6, 9, 10]. Therefore there is a need not only for the characterization of the material, but for the study of sustainable destinations for the waste generated in those activities.

A possible destination to the soapstone waste is as reinforcement for polyethylene composites. After all, in the literature, there is a large number of studies that report gain in mechanical strength and stiffness by incorporating commercial talc particles into polyolefins [11, 12, 13, 14]. In general, the improvement in mechanical strength by incorporating fillers into thermoplastics is accompanied by a loss in ductility, since the particles cause a reduction in chain mobility, usually decreasing elongation at break [13]. The addition of particles can also increase the shear viscosity, and consequentially, alter the polymer processing conditions [15]. Accordingly, a compromise must be made between improved mechanical properties in the solid state, the loss in ductility and the increased difficulty of melt processing [16]. The modification of the properties is determined not only by the interaction between the matrix and filler, but also by the morphology formed during processing [17]. Therefore, it is important to study the influence of the addition of fillers on the flow properties of the neat polymer in order to optimize and control process conditions.

The macroscopic behavior of a particulate reinforced composite is intrinsically dependent of the microstructure formed during processing. In regard to mechanical behavior, two very relevant factors are the particle distribution and the interfacial adhesion between particles and matrix. Particle distribution is often not uniform in these type of composites, instead, the particles are clustered in some local regions, forming agglomerates throughout the material. Agglomeration of the reinforcement phase can have a negative effect on the practical behavior, in fact, particle clustering has been shown to have deleterious effects on tensile strength, flow stress, ductility and fatigue performance [18]. In addition, the mechanical strength of a composite material is fundamentally dependent on the load transfer between filler and matrix phases, thus, it is dependent of interfacial adhesion.

The objective of this work is to assess the use of soapstone residue as reinforcement for high-density polyethylene (HDPE) composites. The motivation is not only to decrease the powder discharge from the workshops, but to allow an alternative source of income, as the artisans could sell the waste for profit. This work was divided in three steps. First, the characterization of the soapstone waste was done with automated image analysis, X-ray diffraction, infrared and Raman spectroscopy. Then, HDPE composites were manufactured using the waste as a disperse phase. The composites were fabricated in three HDPE/soapstone compositions by weight: 90/10, 80/20 and 70/30. Finally, the composites were characterized. Microstructural characterization was performed with infrared spectroscopy and X-ray microtomography. Tensile, creep and rheological properties were measured in order to determine the

influence of the soapstone particles in the polymer mechanical behavior and processing conditions. Furthermore, in order to better understand and predict the practical behavior of this novel material, the microstructural aspects and macroscopic behavior were linked by fitting the experimental data into theoretical and semi-empirical models from the literature.

This work is divided as follows: chapter 2 - a review of the scientific literature pertinent to the work; chapter 3 - the materials and methods used are described in detail, chapter 4 - results and discussion; and chapter 5 - conclusions and suggestions to future works.

2

Literature Review

2.1

Soapstone

Steatite, commercially known as soapstone, is a metamorphic rock used in both ornamental and construction purposes [5]. Talcous rocks, such as the soapstone, come from limestones and ultra-basic igneous rocks with MgO and SiO₂ above 20 and 50%, respectively [19]. These stones have been formed during medium-grade orogenic metamorphism accompanied with metasomatic interactions involving external H₂O-(± CO₂)-rich fluids [20]. The composition of the soapstone can vary depending on the region and on the geological formation that took place, but according to the definition proposed by Huhta and Kärki [4], to be classified as soapstone the rock must contain between 35% and 75% of talc mineral and less than 35% of hard silicates (such as olivine, pyroxene, serpentine and amphiboles).

Talc is a layered silicate with ideal composition of Mg₃(Si₂O₅)₂(OH)₂. As a compositionally and structurally ordered mineral, the talc is of recent scientific interest because it can, in some ways, serve as a prototype for the trioctahedral 2:1 layer silicates [21]. The natural composition of the talc can also vary, containing impurities such as iron and nitrogen [22].

The crystalline structure of the talc consists of octahedral structures of magnesium hydroxide between tetrahedral layers of silicon–oxygen [23]. The crystallographic data reported by Gruner [24] was imported by the author into the VESTA software in order to obtain a better visualization of the talc's crystalline structure [24, 25]. The resulting image is shown in Fig. 2.1.

According to the geographic location, the talc can be found in its natural state in three major forms: lamellar, granular and acicular. For commercial standards, the most adequate is the lamellar form [23]. Regarding its texture, the soapstone can be found as powder, massive or as a compact rock [5].

Talc is a filler-type industrial material and according to the application, it must have certain properties and characteristics in terms of size distribution, morphology, mineralogy, purity and other factors [5]. For instance, it's high melting point, chemical inertia, low electrical conductivity, low hygroscopy

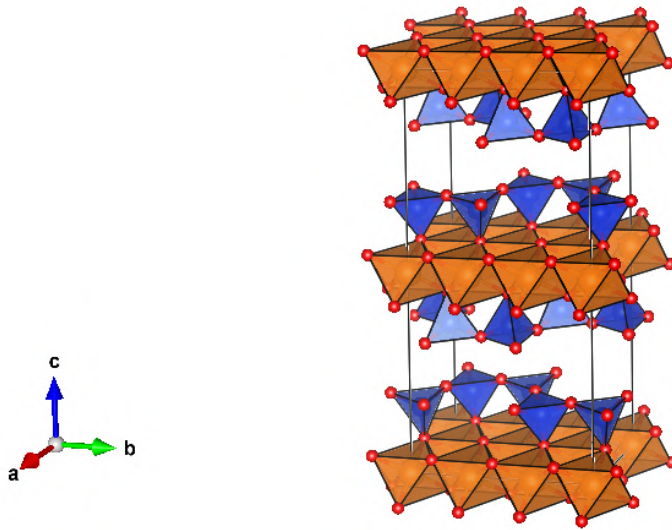


Figure 2.1: Crystalline structure of the talc mineral [24, 25].

and capacity of absorbing oils are responsible for talc's role in the textile and cosmetics industries. In the rubber industry, talc is used in the vulcanization process and in the production of insulating ducts for wiring [19]. When pure (over 90%) is used in the pharmaceutical industry and, in the case of variable purity, it is used as feed-stock for electric ceramics [19]. Some other applications of the talc are in agribusiness, in construction and in the ceramic industry, as a magnesium source for controlling thermal expansion [8].

In respect to physical characteristics, the soapstone is chemically resistant to both alkaline and acid substances and has an excellent temperature resistance, being able to withstand temperature changes from way below zero to above 1000°C without considerable degradation [8]. Soapstone rock is often used as building stone and dimension stone [5].

Historically, steatite is present in the daily life of mankind since the Early Middle ages. Archaeological studies have revealed fragments of pots made from soapstone that date between the 9th and 10th century [26]. The use of soapstone in construction date to the beginning of the 15th century in Europe, when it started to be vastly applied in the architecture of palaces and monuments. Locally, the soapstone is largely found in monuments and building of Minas Gerais historical cities. Antônio Francisco Lisboa, popularly known as Aleijadinho, a famous sculptor and architect from Colonial Brazil, made most of his work out of soapstone [8]. Another example of the applicability of this mineral can be found in the "Christ Redeemer" monument, in Rio de Janeiro, that is made of concrete and covered by a soapstone mosaic. This mineral was

chosen for coverage because of its durability and easy use [27].

2.1.1 Production

Worldwide, Brazil is one of the ten largest talc producers, corresponding to approximately 10% of the global production (data from 2019) [28]. Table 2.1 shows the distribution of talc and pyrophyllite market in Brazil between 2014 and 2016 [29]. Figure 2.2 shows the deposits of talc, including soapstone, around the country. The major production occurs in the Ouro Preto region of Minas Gerais state, where there are several soapstone quarries that exploit this rock as dimension stone. These cities have rich deposits of talc that are extracted as by-products and sold to ceramic industries. The rough blocks are exported to European and North American countries, where they are cut into building stones. Only at Bandeiras, a sub-region of Ouro Preto, the annual production in 2012 was of 4,800 tons of soapstone and 2,400 tons of talc. During the exploitation only 30% of the rock is recovered, the remaining 70% is composed of small blocks that are destined to artisan workshops that manufacture pans and souvenirs [5].

Table 2.1: Distribution of the Brazilian market of talc and pyrophyllite [29].

		Unit	2014	2015	2016
Production ⁽²⁾	Crude	(t)	531,938	481,687	494,157
	Beneficiated	(t)	164,351	160,864	162,870
	Total	(t)	696,289	642,551	657,027
Imports	Beneficiated	(t)	13,775	9,764	7,384
		(10 ³ US\$-FOB)	7,505	5,050	3,690
Exports	Beneficiated	(t)	10,560	12,553	12,570
		(10 ³ US\$-FOB)	6,148	6,954	6,047
Apparent Consumption ⁽¹⁾	Beneficiated	(t)	167,566	158,075	157,684
Prices ⁽³⁾		(US\$/t)	582	554	481

⁽¹⁾ Apparent Consumption: production + imports – exports; ⁽²⁾ talc + pyrophyllite;

⁽³⁾ average export price of natural talc-steatite concentrate.

The craftsmanship and manufactures are linked with social development since these activities foment the local economies in many cities within the region of Minas Gerais [8]. However, the harness of the soapstone can be hazardous to the environment, the health of the workers and the nearby residents. The global recovery of soapstone exploited in quarries is only 40 wt%, so approximately 60 wt% of the rock is discharged as residue. In addition, artisan workshops produce a large quantity of soapstone powder (approximately 10-15% rock recovery), which is discarded careless, often causing environmental problems. [5]. So there is a need not only for the characterization of the material, but for the study of sustainable destinations for the waste generated in those activities. The advantages are not only to decrease the environmental impact of powder discharge, but also to allow an



Figure 2.2: Major Brazilian deposits of talc, including soapstone. Adapted from [5].

alternative source of income, as these artisans can sell this powder for profit [5].

In Europe, talc and/or soapstone quarries can be found mainly in France, Italy, Finland, Norway and Sweden. The Nordic countries, in general, have a very active mineral industry. The main commodities mined are carbonate rocks, quartz, feldspar, apatite, olivine and talc [30]. Finland is the second largest talc producer in Europe, second only to France, and it fits amongst the ten largest producers globally [28]. In 2012, 110,000 tons of Finnish soapstone were produced, generating 60-75 wt% of waste [31]. The Finnish natural stone industry's mainstream is the advanced production of soapstone products, that represent approximately 50% of the total stone industry turnover (200 million euros). In 2006, the total output of usable soapstone was around 185,000 tons, of which 50,300 tons of soapstone products were manufactured. In Sweden, ground talc is used as a filler in roofing and soapstone is produced as block stone for interior fireplaces and heat-resistant cooking plates [30]. Soapstone has been quarried and used in Norway from the Stone Age onward. At the time, it was used to make net sinkers, small clubs and animal figurines. At the Bronze Age, it was applied as raw material for casting moulds. It also became a relevant material for decorative stone in churches and other town buildings in the Medieval Period. Nowadays, the demand for soapstone consists mainly in the fireplace industry and for restoration of medieval churches [32].

During 2019, the total sales (domestic and export) of talc by the United States (U.S.) were estimated to be 570,000 tons, valued at \$120 million. Talc produced and sold in the U.S. was used in paint (23%), ceramics (including automotive catalytic converters) (20%), paper (15%), plastics (12%), rubber (4%), roofing (3%), and cosmetics (2%). The remaining 21% was for export, insecticides, refractories, and other miscellaneous uses. The amount of talc recycled was considered insignificant by comparison with the production numbers [28].

Currently, China is the largest producer of talc globally, with India being a far second. The estimated world mine production and reserves of talc, according to the Mineral Commodity Summaries (2020), are listed in Tab. 2.2. [28].

Table 2.2: World mine production and reserves of talc [28].

	Mine Production ⁽¹⁾		Reserves ⁽¹⁾
	2018	2019	
United States (crude)	650	630	140,000
Brazil (crude and beneficiated) ⁽²⁾	660	650	45,000
Canada (unspecified minerals)	210	210	NA
China (unspecified minerals)	1,800	1,800	82,000
Finland	380	370	Large
France (crude)	450	450	Large
India ⁽²⁾	920	950	130,000
Italy (includes steatite)	170	170	NA
Japan ⁽²⁾	160	160	100,000
Korea, Republic of ⁽²⁾	350	350	100,000
Other countries (includes crude) ⁽²⁾	815	820	Large
World total (rounded)⁽²⁾	6,600	6,600	Large

⁽¹⁾ Data in thousand metric tons; ⁽²⁾ includes pyrophyllite. NA: not available

2.1.2 Characterization

Assis et al. [7] measured granulometry, thermal behavior and mineralogical characteristics of soapstone powder produced in Congonhas, MG. The particle size distribution was obtained by sieving (48 to 400 mesh) and the mass percentage for each size range is listed in Tab. 2.3. The mineralogical characterization was done with X-Ray Diffraction (XRD) (Fig. 2.3) and revealed crystalline phases coherent with talc mineral. The thermal gravimetric analyses revealed high temperature stability. During the experiment, the soapstone waste remained stable up to 1500°C, showing only one degradation process (mass loss of 9%) between 500°C and 800°C [7].

Table 2.3: Particle size distribution of soapstone waste obtained in Congonhas, MG [7].

Particle Size (μm)	PPS Mass (%)
0-32	3.7
32-45	5.2
38-53	11.9
63-90	21.5
125-180	27.5
250-355	30.2

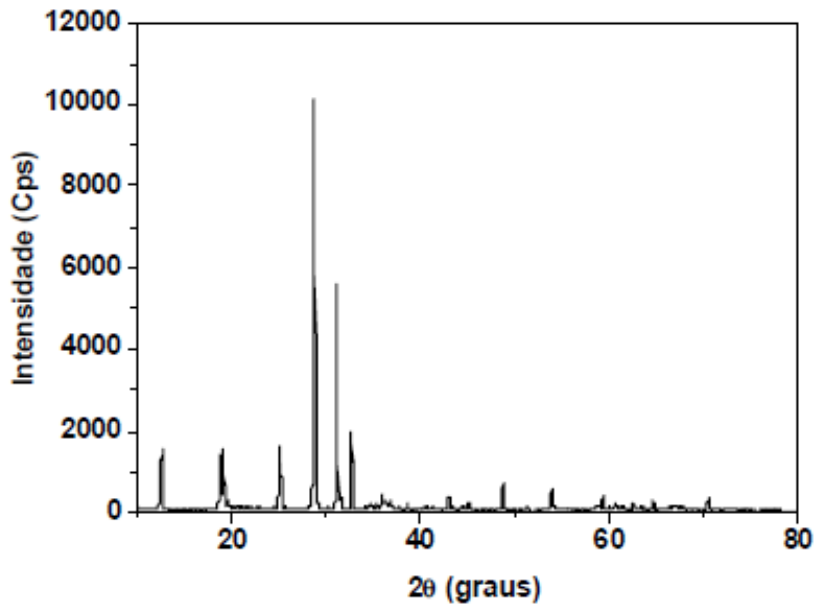


Figure 2.3: XRD of the soapstone waste from Congonhas, MG [7].

In his work, Rodrigues [23] did the characterization of soapstone residues from Cachoeira do Brumado (S01) and Bandeiras (S02 to S05). The density was determined by a helium pycnometer and the surface area was obtained by a gas adsorption analyzer. The results are listed in Tab. 2.4 [23].

Table 2.4: Density and surface area of soapstone from Cachoeira do Brumado e Bandeiras, MG [23].

Sample	Surface Area (m^2/g)	Specific Mass (g/cm^3)
S01	2.397	2.952
S02	1.014	2.729
S03	0.816	2.730
S04	0.944	2.837
S05	0.469	2.734

The granulometric characterization of the residue was done in duplicate by wet sieving of previously homogenized and quartered samples. The sieving process was done with Tyler series sieves starting at $1700 \mu\text{m}$ (10#). The fraction under $37 \mu\text{m}$ (400#) was analyzed in a laser granulometer. The D_{80} dimension and the percentages under 37 and $10 \mu\text{m}$ for each sample are listed

in Tab. 2.5. Later, the granulometric fractions were homogenized, quartered and pulverized. The pulverized product was analysed by XRD. The minerals identified in the sample from Cachoeira do Brumado are listed in Tab. 2.6, while the results for the Bandeiras samples are listed in Tab. 2.7 [23].

Table 2.5: Particle size distribution of soapstone from Cachoeira do Brumado e Bandeiras, MG [23].

Sample	D ₈₀ (μm)	Fraction < 37 μm (%) Wet sieving	Fraction < 10 μm (%) Laser granulometer
S01	742	26.4	5.26
S02	710	20.8	3.48
S03	1084	13.5	2.19
S04	558	36.2	5.63
S05	1575	14.4	2.36

Table 2.6: Minerals identified in the XRD of the soapstone form Cachoeira do Brumado, MG [23].

Soapstone from Bandeiras	
Mineral	Formula
talc	$\text{Mg}_3\text{Si}_4\text{O}_{10}(\text{OH})_2$
tremolite	$\text{Ca}_2\text{Mg}_5(\text{Si}_8\text{O}_{22})(\text{OH})_2$
dolomite	$\text{Ca,Mg}(\text{CO}_3)_2$
magnetite	Fe_3O_4
ilmenite	FeTiO_3
magnesite	MgCO_3
nimite	$(\text{Ni, Mg, Al})(\text{Si, Al})\text{O}(\text{OH})$
quartz*	SiO_2

* Identified only in the fractions smaller than 149 μm (100#).

Table 2.7: Minerals identified in the XRD of the soapstone form Bandeiras, MG [23].

Soapstone from Bandeiras	
Mineral	Formula
talc	$\text{Mg}_3\text{Si}_4\text{O}_{10}(\text{OH})_2$
kaolinite	$\text{Si}_2\text{Al}_2\text{O}_5(\text{OH})_4$
chlorite-serpentine	$(\text{Mg, Al})_6(\text{Si, Al})_4\text{O}_{10}(\text{OH})_8$
nimite	$(\text{Ni, Mg, Al})(\text{Si, Al})\text{O}(\text{OH})$

In another work, Rodrigues et al. [5], characterized and purified soapstone powder from an artisan workshop in Bandeiras-Santa Rita de Ouro Preto, MG. The objective of the study was to identify potential applications for the residues and purified products. The size distribution, obtained by sieving, is represented in Fig. 2.4 [23].

The mineralogical composition was determined by X-ray diffraction and the minerals identified, with their respective basal spacing values were:

- talc (9.205; 3.1021; 4.641; 2.4826; 1.5550; 1.3881 Å);
- kaolinite (7.062; 3.7221; 3.5540; 3.1021; 2.2261; 2.1874; 2.0035; 1.8067; 1.6702; 1.5550 Å);
- chlorite-serpentine (13.94; 7.062; 4.641; 3.554; 2.8453 Å);

- nimitite (13.94; 7.062; 4.7156; 3.5540; 2.8453 Å);
- magnesite (2.8453; 2.3294; 2.0829; 1.3881 Å);
- dolomite (2.8453; 2.1874; 2.0035 Å) [5].

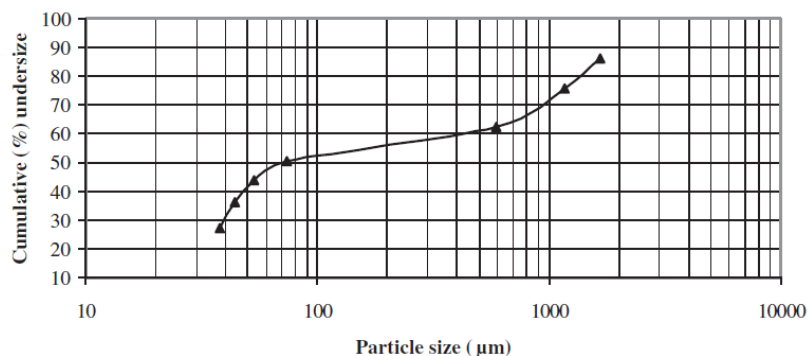


Figure 2.4: Cumulative particle size distribution of soapstone residue from Bandeiras, MG [5].

The minerals sulphides (pyrite, arsenopyrite, pentlandite) and oxides (magnetite/hematite) were identified in soapstone from the Bandeiras region in previous studies done by Lima et al. [33]. However, these minerals were not detected in the X-ray patterns of the size fractions done by Rodrigues et al. [5], probably due to their small proportion in the sub-samples analysed, according to the authors [5].

In order to assess an undergoing restoration of the "Christ Redeemer" monument in Rio de Janeiro city, Ribeiro et al. [27] provided a technological characterization of soapstone that covered the statue. As mentioned before, the statue is made of concrete and covered by a steatite mosaic. Because of its location, on top of the Corcovado Hill, surrounded by a tropical forest and close to the sea, the soapstone is exposed to many environmental factors that can cause degradation throughout the years. The goal of the work was to study the material, determine inherent pathologies, check problems imposed by the environment and validate the effects of applying water repellent to make the restoration work more efficient and lasting. As part of the study, petrographic and mineralogical characterization were performed in the soapstone tesserae that composed the mosaic. The minerals observed in both techniques were: talc, chlorite, calcite and tremolite [27].

Balek et al. [34] reported the effects of grinding on the microstructure and thermal behavior of the talc mineral. X-ray diffraction (Fig. 2.5) revealed that grinding produced structural alteration, blurring the [001] basal reflections. Scanning electron microscopy (SEM) micrographs (Fig. 2.6) revealed

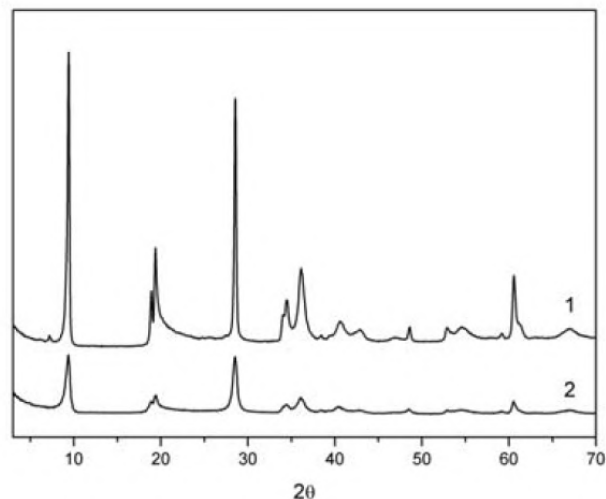


Figure 2.5: XRD patterns of talc samples, curve 1 - unground sample, curve 2 - ground sample [34].

that grinding caused a reduction in particle size and changes in their shape. Differential thermal analysis (DTA) and thermogravimetry (TG) measurements were performed and are shown in Fig. 2.7 and 2.8. From the TG results of the ground talc sample, it followed that a mass loss took place in the range from 30°C up to 150°C. Only a small mass loss was observed in this temperature range with the unground sample [34].

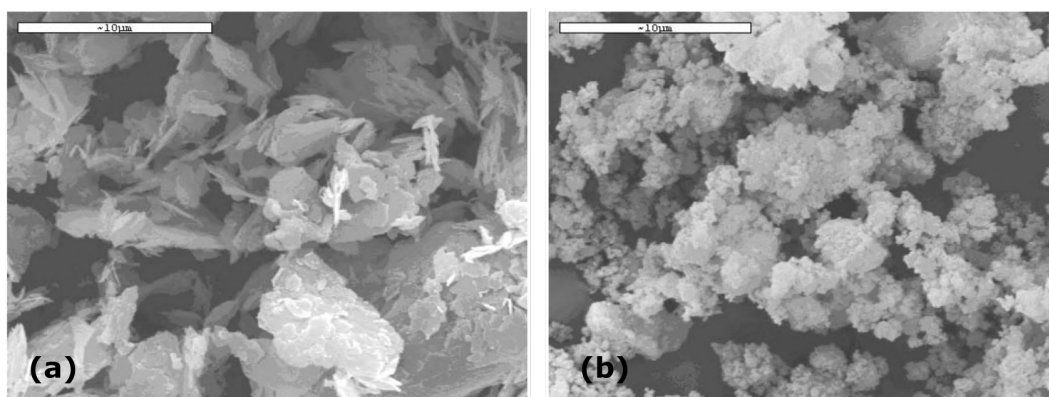


Figure 2.6: SEM micrographs of (a) unground and (b) ground talc samples [34].

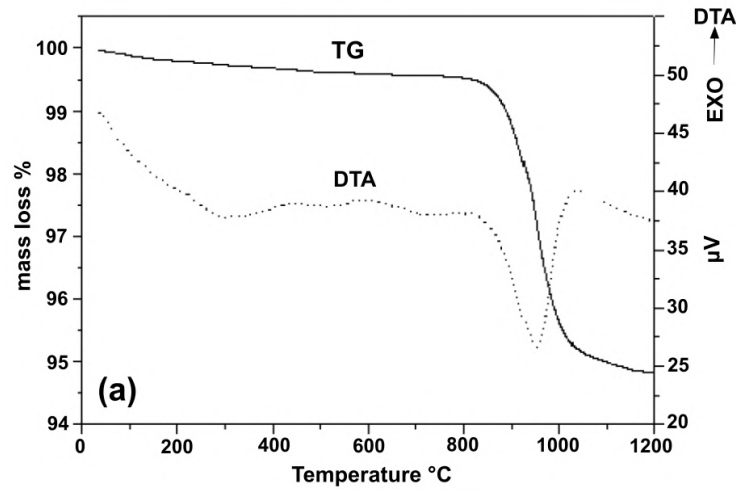


Figure 2.7: Results of DTA and TG of talc samples measured during heating and subsequent cooling in air - unground sample [34].

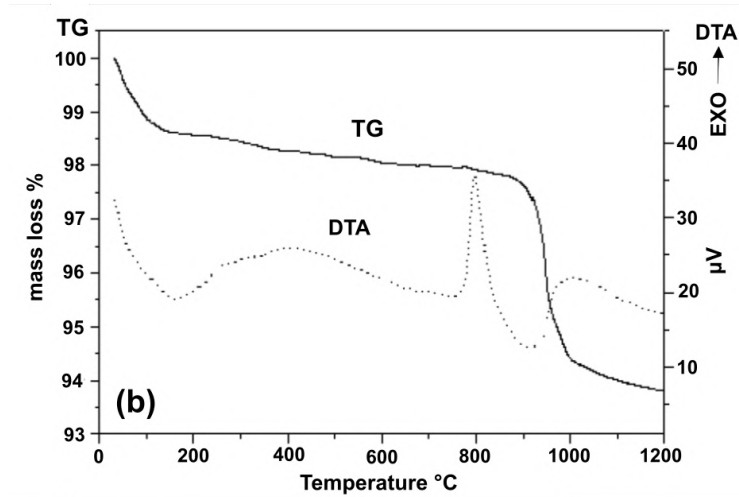


Figure 2.8: Results of DTA and TG of talc samples measured during heating and subsequent cooling in air - ground sample [34].

Based on the fact that the talc from soapstone is composed of bio-compatible elements, Mota et al. [35] incorporated the talc into hydroxyapatite (HA) coatings in order to improve mechanical properties without reducing the bio-compatibility of the material. Talc flakes were obtained from unpolished soapstone, purchased in Ouro Preto, Brazil. The particle size distribution and SEM image of talc platelets after mechanical scraping are shown in Fig. 2.9. The X-ray diffraction of the talc from the unpolished soapstone is shown in Fig. 2.10. The overall results from this research showed the HA/talc composites presented enhanced mechanical properties and bio-compatibility tests confirmed that composite coatings were bio-compatible and induced

cellular proliferation and bone maturation [35].

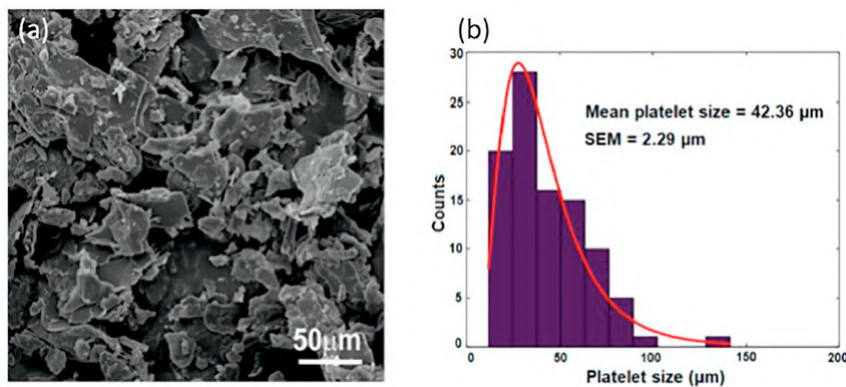


Figure 2.9: (a) SEM image of talc platelets obtained from an unpolished soapstone after mechanical scraping. SEM magnification 1000 x. (b) Size distribution of talc platelets [35].

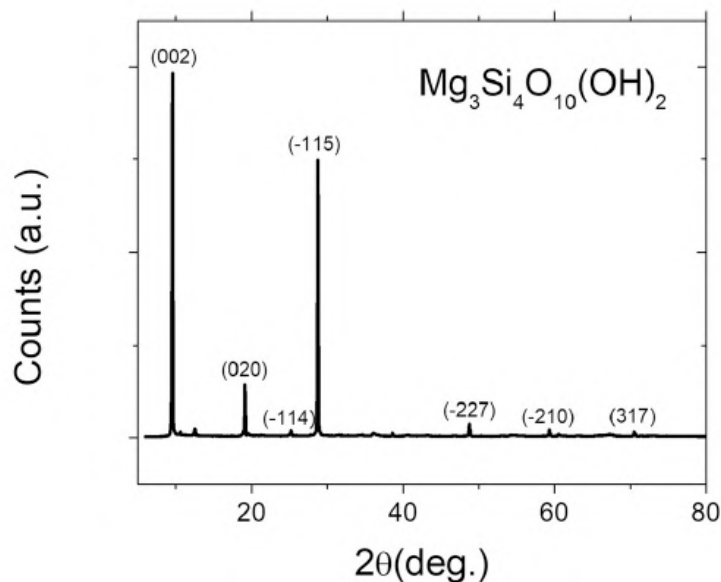


Figure 2.10: X-ray spectrum of talc platelets from unpolished soapstone [35].

2.2 Polyethylene

Polyethylene (PE) was discovered in 1933 by Reginald Gibson and Eric Fawcett and is part of the polyolefins family, a class of polymers synthesised from olefinic monomers, i.e., non-cyclic monomers that present at least one double bond between carbon atoms [36]. Polyethylene, in particular, is formed from the ethylene monomer, $CH_2=CH_2$, resulting on the polymeric structure illustrated in Fig. 2.11 [37]. Polyolefins represent approximately 60% of the

global demand for thermoplastics, with polyethylene being responsible for around 40%. In Brazil, polyolefins represent around 65%, from which 43% of the demand is for polyethylene [38].

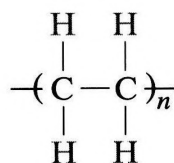


Figure 2.11: Polyethylene structure [37].

Polyethylene is a semi-crystalline flexible polymer and its properties are substantially influenced by the relative fractions of amorphous and crystalline phases. In general, some characteristics that are responsible for its large range of applications in the plastic industry are toughness, easy processing, low moisture absorption, as well as chemical, abrasion and impact resistance [36]. Under normal conditions, depending on the additives used, polyethylene is not toxic and can be utilized for food and pharmaceutical packaging [38]. Other applications of PE can be found in construction, transport, electronics, recreational, amongst others [36].

PE properties are sensible to the polymerisation method and to the reaction conditions, which allows a tailor-made range of products. The polymer chain length and the degree of crystallinity are strictly linked to the mechanical properties and can be tailored by controlling the amount of reactants in the reactor [36]. For instance, it is known that long-chain branching in polymers has a strong influence on the molecular weight distribution and hence on polymer properties, particularly rheological and film properties such as haze and gloss [36].

The polymerization of ethene can be released by radical initiators at high pressure, as well as by organometallic coordination catalysts. The processing can be done in solution or in bulk [39]. For pressures above 100 MPa, ethene itself acts as a solvent. Both low- and high-molecular-weight polymers up to 10^6 g/mol can be synthesized by either organometallic coordination or high pressure radical polymerization [39]. However, the structure obtained is different for each method. Radical initiators result in somewhat branched polymer chains, whereas organometallic coordination catalysts synthesize linear chains [39].

PE is often classified by its density and by the type of process used in its manufacture. According to the reaction conditions and the catalytic system utilized, five types of polyethylene can be produced [38]:

- Low density polyethylene (LDPE);
- High density polyethylene (HDPE);
- Linear low density polyethylene (LLDP);
- Ultra high molecular weight polyethylene (UHMWPE);
- Ultra low density polyethylene (ULDPE).

The major difference between LDPE and HDPE lies in the type of chain formed in the polymerization process. The linear chains of HDPE provide more efficient orientation, alignment and packing of chains. Hence, van der Waals forces are stronger and the density, as well as the crystallinity of these polymers are higher, as can be seen in Tab. 2.8. On the other hand, LDPE presents long branches in its structure, which results in smaller crystallinity and worse mechanical properties when compared to HDPE [38].

Table 2.8: Comparison between HDPE and LDPE characteristics [38].

	LDPE	HDPE
Type of polymerization	Radical	Coordination
Polymerization pressure (atm)	High 1000 - 3000	Low 1 - 30
Reaction temperature (°C)	High 100 - 300	Low 50 - 100
Type of chain	Branched	Linear
Density (g/cm³)	Low 0.91 - 0.94	High 0.94 - 0.97
Crystallinity (%)	Low 50 - 70	High up to 95
Melt temperature (°C)	Low 110 - 125	High 130 - 135

In the present work, HDPE was used as matrix for the composites manufactured. The choice was based on applicability, price, chemical resistance and easy acquisition of the material.

2.2.1 High Density Polyethylene

The discovery of organometallic catalysts done by Ziegler and the application of this catalytic system in the synthesis of stereo-regular polyolefins done by Natta led to the current large production volume of linear polyolefins such as HDPE [36]. The first catalytic system to provide satisfactory results was a combination of triethyl-aluminum and titanium tetrachloride [38]. Other coordination catalysts are often employed. In general, they all contain a transition metal that is soluble or insoluble in hydrocarbons, supported by silica, alumina, or magnesium chloride. Currently, mainly Ziegler and Phillips catalysts, as well as some metallocene catalysts are used industrially [39].

Under Ziegler-Natta catalysts, the polymerization of ethene occurs under a pressure range of 10 to 15 atm and temperature range of 20 °C to 80 °C, in a paraffinic-hydrocarbon media, in the presence of an alkyl aluminum compound and Ni, Co, Zr or Ti salt [38].

In the Phillips process, the polymerization occurs under low pressure, around 50 atm, and temperatures under 100 °C. An alumina supported catalyst, consisting of chromium oxide and activated by a base, is employed. When compared with the polyethylene obtained by Ziegler-Natta, the product is less branched and, consequentially, has higher density due to higher crystallinity [38].

In general, linear polyethylene is highly crystalline (above 90%) and presents less than one side chain per 200 carbon atoms in the main chain. Its melting temperature for the crystalline phase is 132°C and its density is in the 0.95 g/cm³ to 0.97 g/cm³ range. The mean numeric molecular weight is located between 50,000 and 250,000 [38]. The mechanical properties of HDPE are listed in Tab. 2.9. Table 2.10 presents a comparison between linear HDPE, Ziegler HDPE and LDPE [38].

Table 2.9: HDPE properties [38].

Property	Highly linear	Low-branched
Density (g/cm ³)	0,962 - 0,968	0,950 - 0,960
Refractive index	1,54	1,53
Melt temperature (°C)	128 - 135	125 - 132
Thermal conductivity (W/m.K)	0,46 - 0,52	0,42 - 0,44
Yield point (MPa)	28 - 40	25 - 35
Elastic modulus (MPa)	900 - 1200	800 - 900
Tensile strength (MPa)	25 - 45	20 - 40
Shear strength (MPa)	20 - 38	20 - 36

Table 2.10: Mechanical properties of linear HDPE, Ziegler HDPE and LDPE [38].

Property	Linear HDPE, 1 CH ₃ /1000 carbons	Ziegler HDPE, few branches, 3 CH ₃ /1000 carbons	LDPE, highly-branched, 20 CH ₃ /1000 carbons
Melt flow index (MFI)	5 - 11	0,9 - 6	1 - 7
Density (g/cm ³)	0,966 - 0,968	0,955 - 0,970	0,918 - 0,918
Yield point (MPa)	31 - 33	29 - 29	6,2 - 11,5
Yielding strain (%)	9 - 9	20 - 20	100 - 800
Tensile Strength (MPa)	20 - 30	22 - 30	8,5 - 10,5
Maximum strain (%)	900 - 990	1000 - 1000	500 - 500
Elastic Modulus (MPa)	1400 - 1550	900 - 1000	400 - 500
Impact strength (kJ/m ²)	9 - 50	20 - 30	Does not break

The mechanical properties of HDPE are highly influenced by the molecular weight. Low-molecular-weight HDPE are fragile and break without necking. In the commercial range typical for HDPE, the necking phenomenon is always present during yielding deformation. Impact resistance is also influenced by the molecular weight. Low-weight samples are fragile, but as the molecular weight is increased to a range of 5×10^5 to 1×10^6 there is a considerable improvement in the impact resistance [38].

HDPE has vast applicability in the modern industry, from the manufacture of day-to-day products such as pipes, tanks, toys, films for packaging and

kitchenware objects to more advanced applications such as radiation shielding, corrosion-resistant wall coverings and prosthetic devices [36].

2.3 Particulate Polymer Composites

Since the early 1960s, there has been an increasing demand for materials that combine low density with higher mechanical properties in many industrial fields such as aerospace, energy and civil construction [40]. To fit this demand, the manufacture of composite materials has gain increasing attention. Composites are based on the concept of combining different materials to satisfy the user requirements and to achieve a performance unattainable by the individual constituents [40].

Filled polymers are the simplest type of composite materials, which consist of a polymeric matrix as the continuous phase in which fillers (disperse phase) are incorporated [41]. The addition of rigid particles to polymers can produce a number of desirable effects such as an increase in stiffness, a reduction in the thermal expansion and an improvement in creep resistance and fracture toughness [42].

Currently, there is a growing tendency of substituting commercial standard fillers for industrial or mineral waste particulates, for both economic and environmental purposes. For instance, by incorporating waste glass powder into a recycled high-density polyethylene matrix (RHDPE), Sadik et al. [3] obtained a fully recyclable composite material with improved mechanical properties and high thermal stability, that can be used as cost-effective automobile dashboard material. With the addition of a maleic anhydride compatibilizer, the RHDPE/glass waste composites presented an increase of up to 29.26% in tensile strength and up to 126.8% in elastic modulus in comparison to the neat recycled polymer [3]. In another study, Sahu et al. [1] showed that stone waste is a promising material for improving the properties of polymeric green composites. Stone waste powder was incorporated into an epoxy matrix, obtaining a moisture resistant, electrical insulating composite material with high mechanical strength that can be used for electrical insulating and advanced construction materials applications [1].

Recent studies showed that talc is a promising particulate to enhance the impact strength and thermo-physical characteristics and can significantly reduce the post-extrusion swelling of high density polyethylene (HDPE) [13, 14, 43]. It is also generally accepted that mineral particles can reduce the rate of diffusion, and hence the permeability of gases and vapors through polymeric materials, which is essential for the making of containers for hydrocarbons,

such as car gas tanks [17]. Studies have also shown good results for HDPE filled with rock waste as a low cost, non-toxic, mechanical resistant alternative for 3D-printed orthopedic prostheses [44].

The enhanced performance combined with cost reduction justify the important role that talc-filled thermoplastics play in the modern industry, especially in the automotive industry. However, the improvement in mechanical strength by incorporating fillers into thermoplastics is generally accompanied by a loss in ductility, since the particles cause a reduction in chain mobility, usually decreasing elongation at break [13]. The addition of particles can also increase the shear viscosity, and consequentially, alter the polymer processing conditions [15]. Accordingly, a compromise must be made between improved mechanical properties in the solid state, the loss in ductility and the increased difficulty of melt processing.

In Section 2.3.1, the concepts that regard the rheology of filled polymers and results from previous works were reviewed. Tensile and creep behaviors of similar composites in the literature are reviewed in Sections 2.3.2 and 2.3.3, respectively.

2.3.1 Rheological Behavior

Rheology is concerned with the description of the mechanical properties of various materials under the various deformation conditions, when they simultaneously exhibit the ability to flow and accumulate recoverable deformations [45]. In this context, there are three ideal types of materials: viscous materials (that dissipate all the external work applied during deformation), elastic materials (that absorb all the external work applied) and viscoelastic materials (that present both behaviors) [46].

Most polymeric materials present a viscoelastic behavior during flow, which means they behave both as elastic solids and viscous liquids. However, in many situations during processing, the viscous characteristics are predominant and thus the elasticity effects may be disregarded [46]. Experimentally, it is observed that most polymer melts present Newtonian behavior only when the shear rates applied are very low or very high. At intermediate shear rates, the relation between the shear stress and the shear rate is not constant, and this behavior is called non-Newtonian viscosity. Both Newtonian and non-Newtonian viscosity are a quantification on the material resistance to flow [45, 46].

In the non-Newtonian region, the viscosity can be expressed by the Power Law, according to the following expression:

$$\eta = K\dot{\gamma}^{n-1} \quad (2-1)$$

where n is the non-Newtonian index and K is the consistency of the polymer melt [47]. The value of n is a measure of the “pseudoplasticity” of the polymer:

- $n = 1$: Newtonian fluid (constant viscosity);
- $n < 1$: pseudoplastic behavior (viscosity decreases as the shear rate increases);
- $n > 1$: dilatant behavior (viscosity increases as the shear rate increases).

The pseudoplastic behavior is the most common amongst polymer melts and it is due to the unfolding and orientation of the polymeric chains as the shear rate increases [46].

In thermoplastics filled with inorganic particles, which is the interest of study of the present work, the appearance of new properties is determined not only by the two different materials but also by the interaction between the matrix and fillers and by the morphology formed during the processing [17]. Composites are characterized by an internal structure, that is associated with the state of orientation and distribution of the fillers. At the low shear range, the rheological behavior is mostly governed by this structure, which is determined by the balance between the restoring forces and shear forces [15]. The important factors which influence this balance are the type of filler/polymer, the size and the surface area of the filler, the surface treatment of the filler, and more importantly, the concentration of the particles.

A wide range of solid particulates are used as reinforcement agents for thermoplastics, including carbon black, various types of fibers, and various naturally occurring minerals. The mineral particles include calcite and various silicates. While fibers are known to induce an anisotropic character to the material, some inorganic particles, such as carbon black and calcite, are usually isotropic. Talc and mica, however, are examples of naturally occurring anisotropic mineral particles. Essentially both are two-dimensional sheets layered with other minerals, which particles are usually constituted of different-sized flakes [48, 49].

In general, the addition of particles increases the shear viscosity and this effect is much more pronounced at low shear rates and it diminishes with increasing shear rate [15]. This happens because at high shear rates, the structure is broken down by the shear forces and the effect of the particles on the viscosity is decreased, as the dissipation due to individual particles starts to be the dominant factor. The pseudoplasticity of the system is usually increased by increasing filler concentration [15].

The internal structure, processing conditions and the rheological behavior of the composite are all interrelated. Therefore, an understanding of these interactions is needed in order to control and optimize process conditions and product performance.

In an investigation of the of the orientation of talc particles in flow and the rheological properties of talc-thermoplastic compounds, Suh et al. [48] evaluated the steady state shear viscosity, as a function of shear rate, of talc-HDPE composites at 160°C. The resulting curve is shown in Fig.2.12. Two commercial talcs with different particle sizes were used in the study: talc-1 (1.5 μm) and talc-2 (7.5 μm). From the results it was inferred that talc particles increased the level of the shear viscosity especially in the low shear rate region. The shear viscosity of talc-thermoplastic melts increased with increasing particle loading and with decreasing particle size [48].

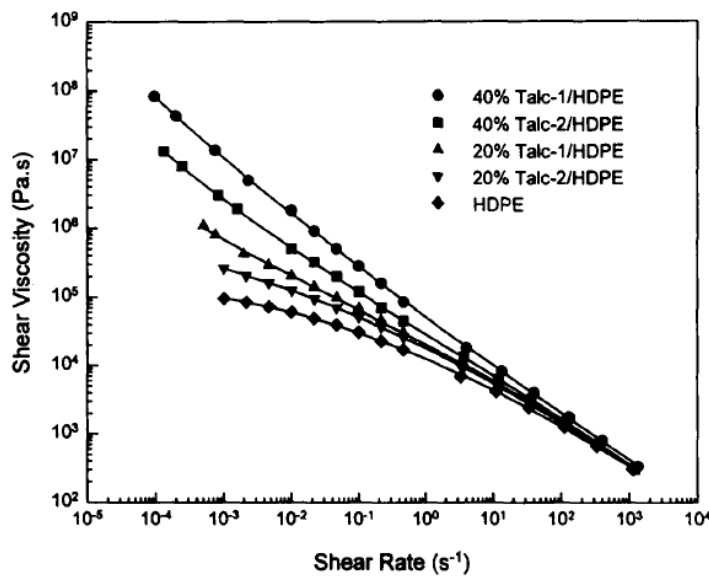


Figure 2.12: Shear viscosity as a function of shear rate for talc-HDPE compounds at 160°C [48].

In another paper, Mehrjerdi et al. [43] investigated the effect of talc on the rheological and extrudate swell properties of HDPE. The HDPE studied is commercially used in extruded pipes. Commercial talc, with density of 2.77 g/cm^3 and median particle diameter (D_{50}) of 2.3 μm was used as filler. Three fractions of filler were used in the composites: 5, 10 and 15 wt%. Thermogravimetric analysis (Figure 2.13) was performed after compounding and confirmed that the residues values at 650 °C are in good agreement with the amount of talc loaded into the samples, since only the polymer is expected to degrade at this temperature range. The onset temperature of mass change

(T_5), the 50% loss temperature (T_{50}), and the percentage residues at 650 °C for the composites are listed in Table 2.11. [43].

Table 2.11: Thermal degradation and residue for HDPE/talc composites [43].

Property	HDPE	5 wt%	10 wt%	15 wt%
Temperature for 5% weight loss (°C)	320	345	404	377
Temperature for 50% weight loss (°C)	424	430	441	449
Residue at 650 °C (%)	0.16	4.99	10.15	14.88

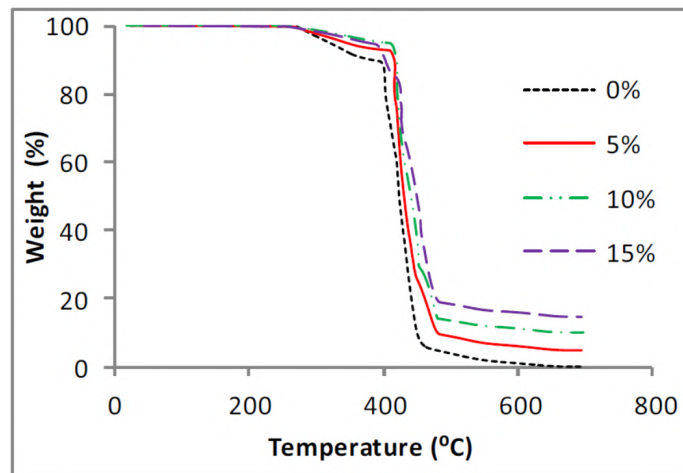


Figure 2.13: Thermogravimetric analysis of HDPE/talc composites [43].

Mehrjerdi et al. [43] performed melt rheological analysis on the HDPE/talc composites using a melt indexer. Three different temperatures were tested: 190 °C, 200 °C and 220 °C; with three levels of load: 5 kg, 10.1 kg and 12.16 kg. Since in the melt indexer measurements are done in a constant shear stress rather than constant shear rate, the rheological characteristics of the neat HDPE and 10 wt% composite were confirmed using a capillary rheometer at 190 °C and 220 °C. The experiments were performed at a shear rate range of 1-10000 s⁻¹ [43].

The melt indexer results are shown in Fig. 2.14, where is possible to notice the dependence of the apparent shear viscosity on the apparent shear rate at 190°C. It is possible to observe that all the materials presented a pseudoplastic (shear-thinning) behavior and that, despite the addition of talc filler, the viscosity remained constant with respect to the filler concentration up to 15%. The authors attributed this unexpected behavior to the morphology of the talc particles. As mentioned before, talc is composed of three disc-shaped layers and these layers are attracted to each other by van der Waals forces and are able to slip over each other easily. When shear forces are applied, the particles have the ability to slide past each other and have a lubricating function in the melt flow [43]. Figure 2.15 shows the effect of talc concentration

on the viscosity of the HDPE composites at varying temperatures and loads. It can be seen that, for a constant load, as the temperature increases, the viscosity decreases. However, the most dominant factor was, in fact, the load. For higher load values, the viscosity drops considerably.

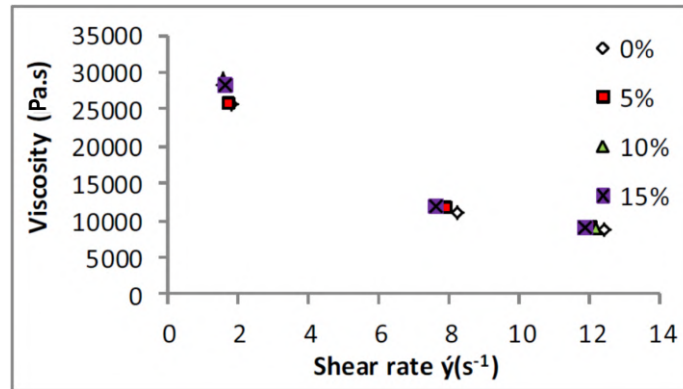


Figure 2.14: Apparent shear viscosity of HDPE-talc composites as a function of the apparent shear rate at varying filler concentrations [43].

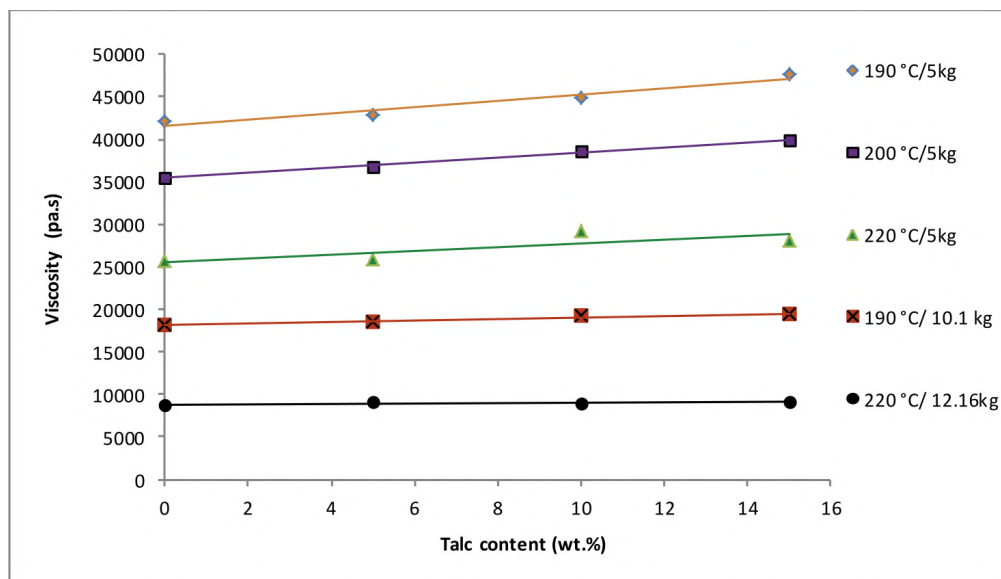


Figure 2.15: Apparent shear viscosity of HDPE/talc composites as a function of the filler content at varying temperatures and loads [43].

Figure 2.16 shows the apparent shear stress at the die wall versus shear rate at 190 °C and 220 °C for the 10wt.% talc-HDPE composite and neat HDPE by capillary rheometer [43]. The relationship between the melt shear stress with the apparent shear rate is represented by the power law model and the value of the power-law index, being that less than unity (0.3033), confirms the pseudoplastic nature of the melt composites [43].

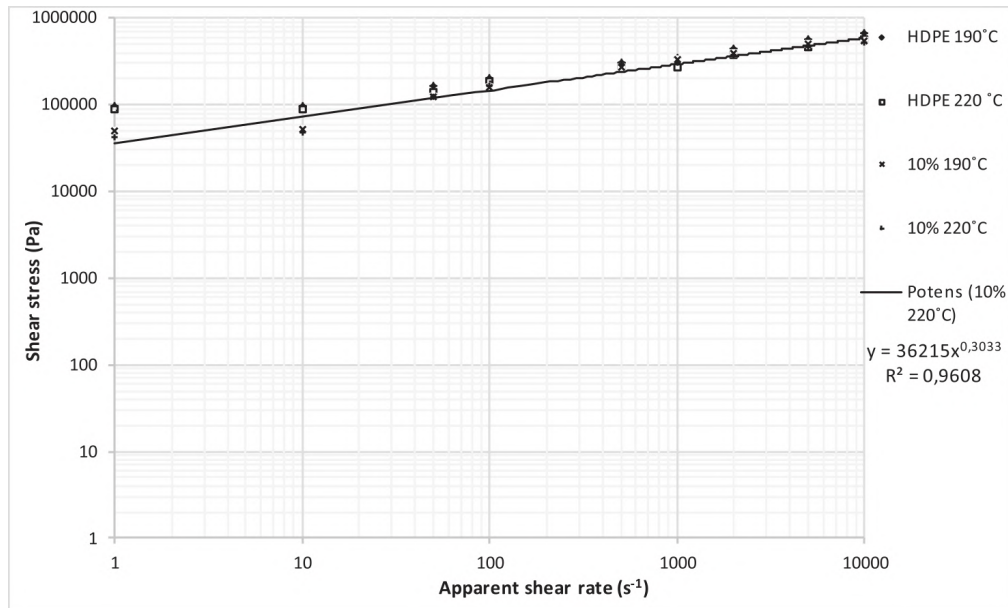


Figure 2.16: The comparison of shear stress and apparent shear rate of neat HDPE and HDPE/talc composite for 10 %wt. talc under 190 and 220 °C in logarithm scale [43].

Mehrjerdi et al. [43] also investigated the influence of talc particles on the post-extrusion swelling effect of HDPE. This effect, also known in the literature as die swell or Barus effect, is a consequence of the elasticity property of the polymer [43]. During the extrusion, the molten polymer is forced by shear forces through a die and afterwards, due to melt elasticity, can expand and become larger than the die size. This phenomenon is relevant in polymer processing because can involve bending and even fracture of the material [43]. Figures 2.17 and 2.18 show the relationship between the die swell and the talc filler content for the HDPE composites. According to these results, the authors concluded that the addition of talc had a strong dominant effect on the reduction of the elasticity of the melt composite, and consequently on the post-extrusion swelling of HDPE. Figure 2.19 shows a comparison of two cut-offs of the post extruded samples with 15 wt% talc and neat HDPE, where the effect of the talc particles on the reduction of the swelling can be confirmed visually [43].

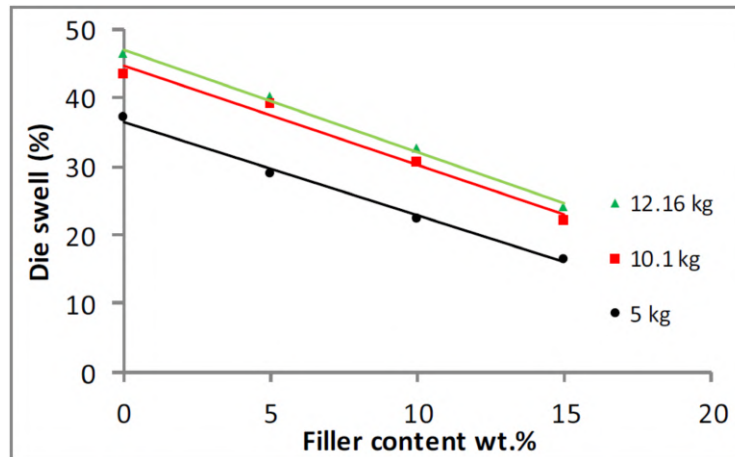


Figure 2.17: Effects of the talc concentration on the die swell of HDPE at varying loads (190 °C) [43].

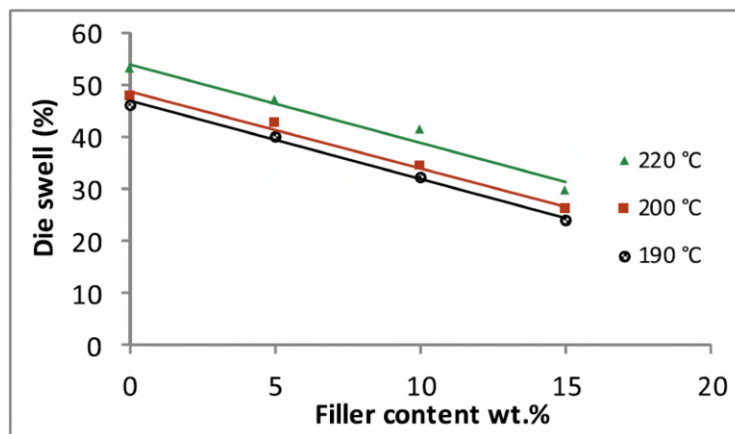


Figure 2.18: Effects of the talc content on the die swell of HDPE at different temperatures (load 12.16 kg) [43].

2.3.2 Mechanical Behavior

Fillers are often added to polymers in order to improve mechanical properties such as tensile and compressive strength, abrasion resistance, toughness, amongst others. The enhancement of those properties depends on the interaction mechanism between phases and, consequently is fundamentally dependent on filler-matrix adhesion. In the case of good matrix-filler adhesion, stress is transferred between phases through shear, the particles tend to restrain movement of the matrix phase and, as a consequence, an increase in the matrix strength is observed [50, 37]. This effect is generally accompanied by a loss in ductility, since the particles cause a reduction in chain mobility, usually decreasing elongation at break [13].

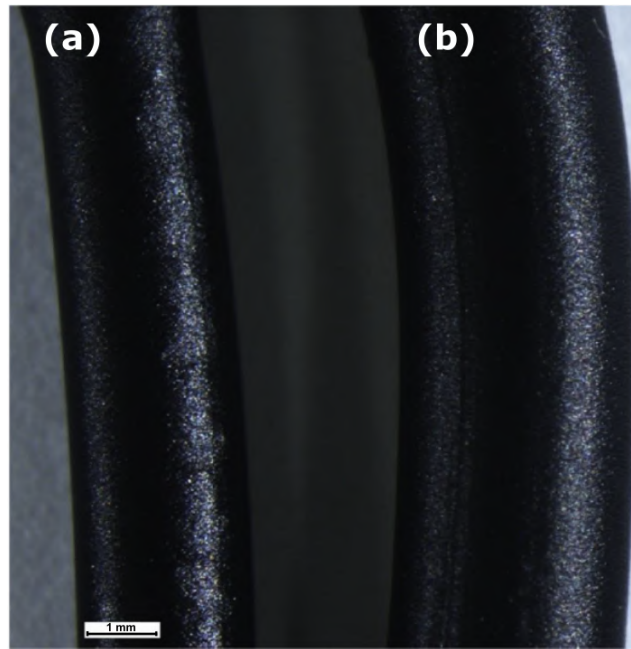


Figure 2.19: General photograph of the post extrudate: (a) composite with 15 wt% talc at 190 °C/5 kg load and (b) HDPE base material at 220 °C/12.16 kg load [43].

Besides the interfacial bonding, other parameters that influence the mechanical behavior of this type of composites are the properties of the individual phases, their respective volume fractions, as well as geometric parameters such as size, shape and distribution of the particles in the matrix [51].

In the literature, no information was found regarding the characterization of HDPE filled with soapstone particles. However, there is a variety of papers that report the characterization of HDPE composites filled with commercial talc particles. Since the soapstone is mainly composed by talc mineral, the results reported in these papers can give some insights to the expected experimental behavior of the composites analysed in the present work.

Karrad et al. [52] determined the mechanical properties of talc filled HDPE. Untreated commercial talc from Luzenac (France), with median diameter of 2.39 μm and density of 2.78 g/cm^{-3} was used with 5, 10, 20 and 30 vol% concentrations. The resulting strain and strength at break as function of filler content is shown in Fig. 2.20. It can be observed that the strength of the polymer decreased with filler addition, which, was linked to lack of adhesion at the filler-matrix interface and to the existence of strong stress concentrations at the interface due to the lamellar character of the talc used. The latter was confirmed by Scanning Electron Microscopy (SEM) images. By analysing the evolution of the deformation at break as a function of talc fraction, one can

observe an increase in this property up to a fraction of 4 vol%, followed by a decay for higher values of talc content. As mentioned before, an decrease in this property is expected when incorporating mineral fillers into thermoplastic polymers. However, the opposite effect was observed, especially for lower concentrations of filler. The authors linked this phenomenon to the formation of cavities generated by the lack of interfacial adhesion. It was suggested that interfacial debonding could blunt the tip of a possible crack and prevent or, at least slow down, further propagation [52].

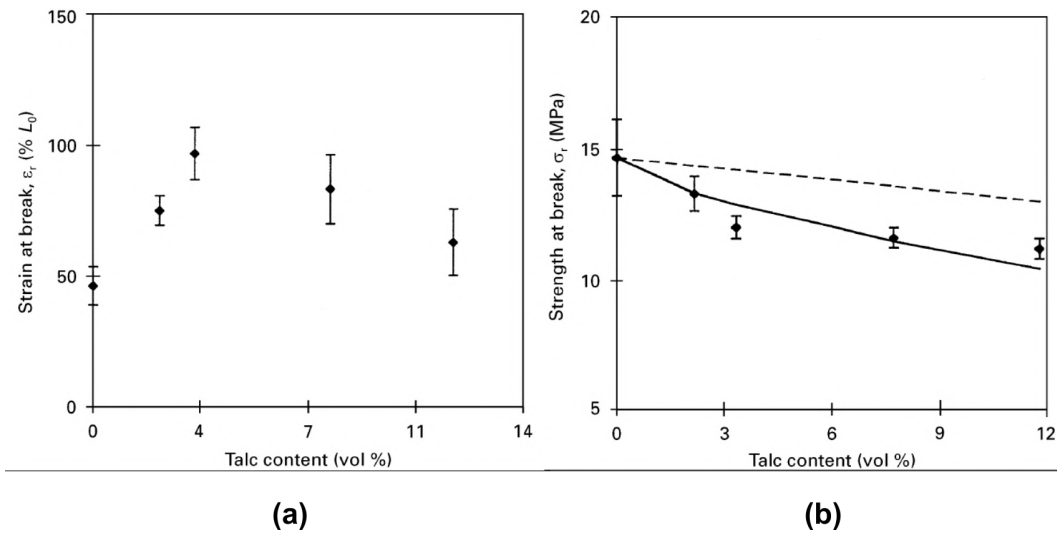


Figure 2.20: Evolution of (a) deformation at break and (b) ultimate tensile strength of HDPE/talc composites as a function of talc content [52].

Mehrjerdi et al. [13] characterized the physical, mechanical and thermo-physical properties of HDPE modified with talc. First, the filler, a commercial talc from Luzenac (France), was characterized through image analysis. The particle size distribution and micrograph of the particles are shown in Fig. 2.21. The particle size distribution was obtained with a Malvem Mastersizer and the mean particle size obtained was $11.14 \pm 0.02 \mu\text{m}$. In the micrograph it was possible to observe the plate-shape morphology of the particles and, by image-processing measurements, the diameter of the particulates was calculated. The median diameter found was $10.2 \mu\text{m}$, which was coherent with the results from the Mastersizer method [13].

Different weight fractions of talc (up to 35 wt%) were compounded with an HDPE matrix containing 2.5 wt% of carbon black (CB). The samples without talc were referred as PE_c . The composites were then processed by injection moulding to obtain specimens for testing. In order to investigate the effect of CB, a sample of the same neat HDPE resin without CB, referred as PE_n , was also tested. The results indicated that CB causes a

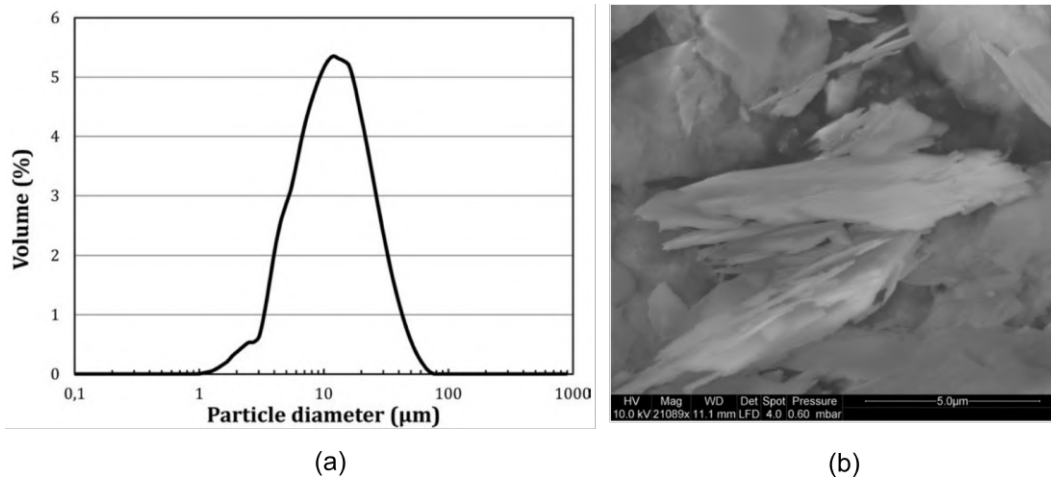


Figure 2.21: (a) Particle size distribution and (b) micrograph of commercial talc HAR T84 from Luzenac, France used in the HDPE composites [13].

significant decrease in the toughness, while talc not only enhances the thermal conductivity and thermo-physical properties of the composites but can also play a role in compensating for the negative effects of CB on impact resistance. The mean mechanical properties are listed in Tab. 2.12 and the tensile strength at yield and at break are plotted in Fig. 2.22 [13].

Table 2.12: Mechanical Properties of Talc/CB HDPE Composites [13].

Blend	Strain at yield (%)	Stress at yield (MPa)	Stress at break (MPa)	E Modulus (MPa)
PE _n	22 ± 1.9	26 ± 0.3	13.3 ± 0.2	660.5 ± 16.8
PE _c	20.4 ± 1.1	25.1 ± 0.5	13.1 ± 0.2	695.8 ± 20.0
5	16.9 ± 2.4	24.5 ± 0.1	12.3 ± 0.1	774.2 ± 31.1
8	20.9 ± 1.1	24.6 ± 0.1	12.3 ± 0.0	988.3 ± 18.9
12	15.1 ± 0.7	25.3 ± 0.2	12.7 ± 0.1	1,057.9 ± 57.9
15	12.9 ± 0.7	25.8 ± 0.1	12.9 ± 0.1	1,201.8 ± 15.4
25	9.7 ± 0.9	26.5 ± 0.3	13.3 ± 0.1	1,680.9 ± 51.7
35	7.1 ± 0.5	28.6 ± 0.2	14.3 ± 0.1	2,231.1 ± 38.7

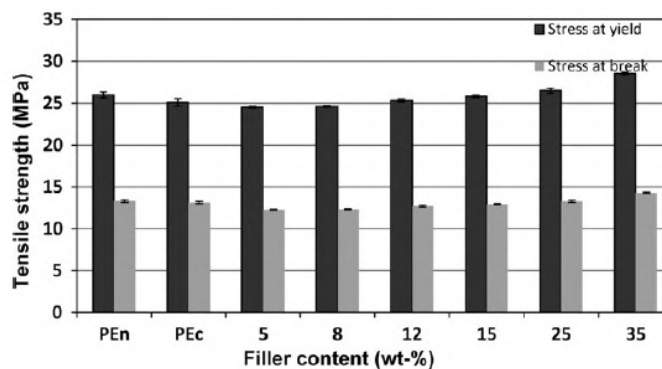


Figure 2.22: Tensile strength at yield and at break for talc-filled HDPE/CB composites [13].

In subsequent study, Mehrjerdi et al. [14] investigated the effects of a titanate coupling agent on the mechanical properties, moisture absorption, and thermal conductivity of the talc/carbon black-filled HDPE. Commercial talc from Luzenac (France) with density of 2.78 g/cm^{-3} and median diameter (D_{50}) of $10.5 \mu\text{m}$ was used as filler. Isopropyl tri(dioctyl)phosphate titanate powder was used as coupling agent. Tensile tests results (Figures 2.23 and 2.24) indicate that the addition of the coupling agent resulted in an increase in stiffness and tensile strength for most cases [14]. Comparing with the untreated samples, the samples treated with the coupling agent presented average increases of 11% for tensile strength and 24% for tensile modulus. However, the addition of the coupling agent also resulted in loss of ductility and there was an average decrease of 28% of elongation at break when the coupling agent was added [14].

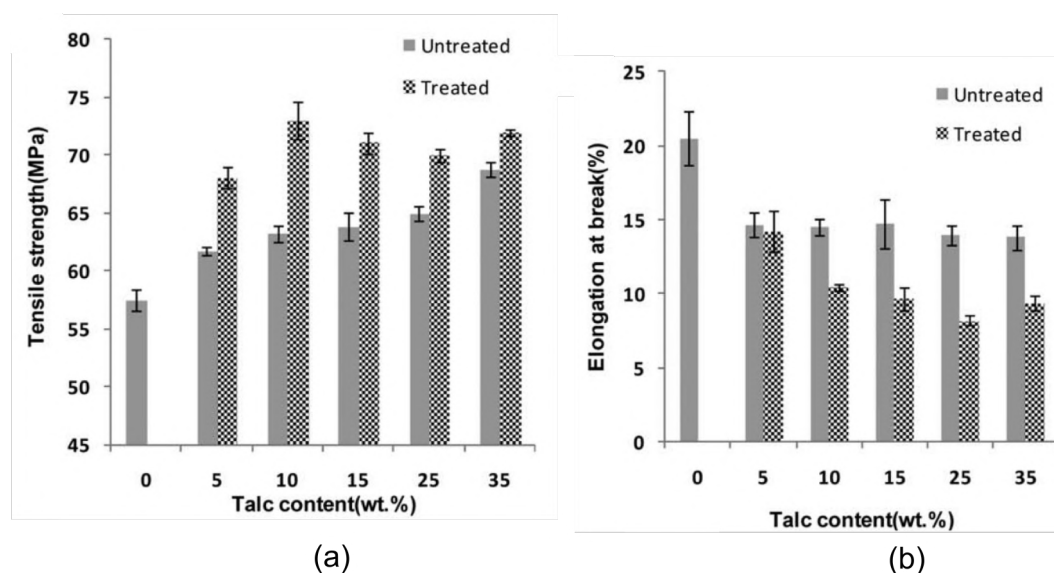


Figure 2.23: Mechanical properties of the HDPE/talc composites as a function of filler and treatment: (a) Tensile strength (b) Elongation at break [14].

The improvements in the tensile strength and stiffness of the composites were explained by the mechanism of reaction of titanate with the inorganic filler. The titanate agent reacts with hydroxyl groups on the surface of the inorganic filler, resulting in the formation of a titanium monomolecular layer on the talc surface, which increases the compatibility of the filler/matrix [14]. However, according to the authors these improvements are due not only to better bonding between matrix and filler, but also to better dispersion and deagglomeration of the particles promoted by the coupling agent. By replacing water of hydration present at the talc surface with organo-functional titanate, the filler/matrix interface becomes more compatible and the dispersion of

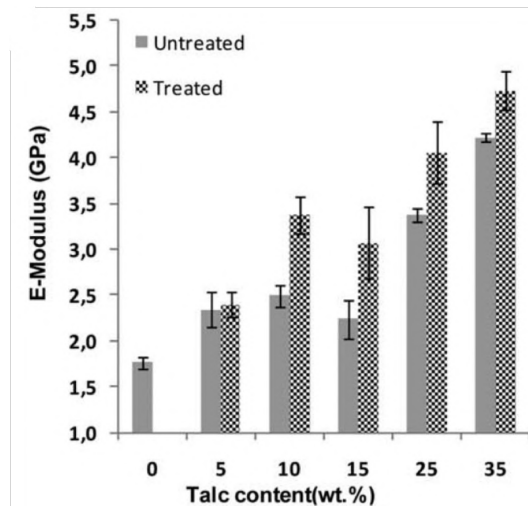


Figure 2.24: Elastic modulus of the HDPE/talc composites as a function of filler and treatment [14].

filler particles is enhanced [14]. The incompatibility between filler and matrix is responsible for the formation of micro-voids in the composites. The void content as a function of filler (Fig. 2.25) in the untreated and treated samples was calculated by comparing the measured density with the theoretical density considering no voids.

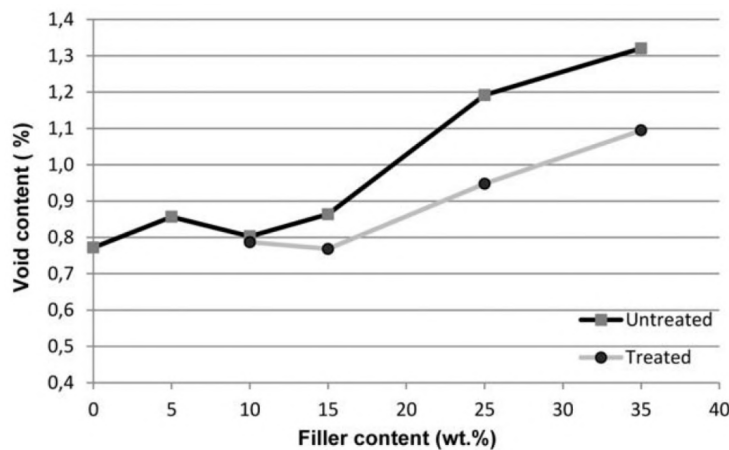


Figure 2.25: Void content as function of filler treatment in the HDPE/talc composites [14].

It was noticed that the void content in the composites decreased in the presence of the titanate coupling agent at all talc loadings. In addition, other analysis performed on the samples revealed that the coupling agent had a negligible effect on the thermal conductivity, thermal diffusivity, and specific heat capacity of the composites [14].

In a more recent study, Savini et al. [53] investigated the effect of the incorporation of microtalc and nanotals at low concentration levels in a HDPE matrix. Three types of talc were used as fillers: natural microtalc (TN), semi-crystalline synthetic nanotalc (NTC) and amorphous synthetic nanotalc (NTA). According to the authors, the main difference between natural talc and synthetic talc is in the crystallinity. Synthetic talc is generated from the precipitation process of the chemical reaction of sodium metasilicate with magnesium acetate, forming a semi-crystalline or even an amorphous material, according to the process variables used. Synthetic talc, due to the structure formed, has a hydrophilic character, while natural talc is a hydrophobic material. Other major differences between both materials are: the particle size, which is micrometric for natural talc and nanometric or sub-micrometric for the synthetic ones; and specific surface areas, which are considerably lower in the natural particles than in the synthetic ones [53].

The morphology of the different types of talc particles was observed by SEM images (Fig. 2.26) and by XRD diffraction analysis (Fig. 2.27). TN talc exhibited a first intense peak at $2\theta = 9.4^\circ$ ($d = 0.94$ nm) and a second peak at $2\theta = 28.3^\circ$ ($d = 0.32$ nm), in addition to several secondary peaks. The more intense and narrower reflections observed in this spectrum indicate a greater degree of crystallinity. Meanwhile, the NTC presented tenuous, wider and less intense diffraction peaks, which indicates low crystallinity. The NTA, a totally amorphous nanotalc, with only short-range order, did not show diffraction peaks [53].

The HDPE composites were made with 1% by mass of talc and the mechanical properties obtained by tensile testing are listed in Tab. 2.13. The results indicated that the incorporation of the micro-tals at low concentrations decreased the tensile strength of HDPE, but in the case of the NTA, it resulted in an interesting balance between stiffness/ductility. The incorporation of only 1 mass% (equivalent to 0.52 vol%) of the NTA caused an increase of 4.5% in the elastic modulus, along with a gain of 50.0% in elongation at break, against a moderate reduction of 3.9% in tensile strength. The incorporation of TN and NTC, however, did not improve the ductility of HDPE, in fact, the TN caused a decrease of 10.8% in elongation at break. The elastic modulus of HDPE presented slight increases of 1.4% and 0.5% with the addition of TN and NTC, respectively. However, both fillers caused a reduction of tensile strength by 7.5% and 5.6%, respectively.

The reduction in the tensile strength of all composites studied by Savini et al. [53] indicated a weak interaction between HDPE and the micro-tals. According to the authors, the hydrophilic/polar characteristic of synthetic tals

possibly resulted in low chemical affinity with the nonpolar matrix of HDPE. In the case of natural talc (TN), which exhibits nonpolar behavior, the decrease in strength was related to the low specific surface area of the filler, that at this low concentration level, did not form an efficient interaction mechanism with the matrix [53].

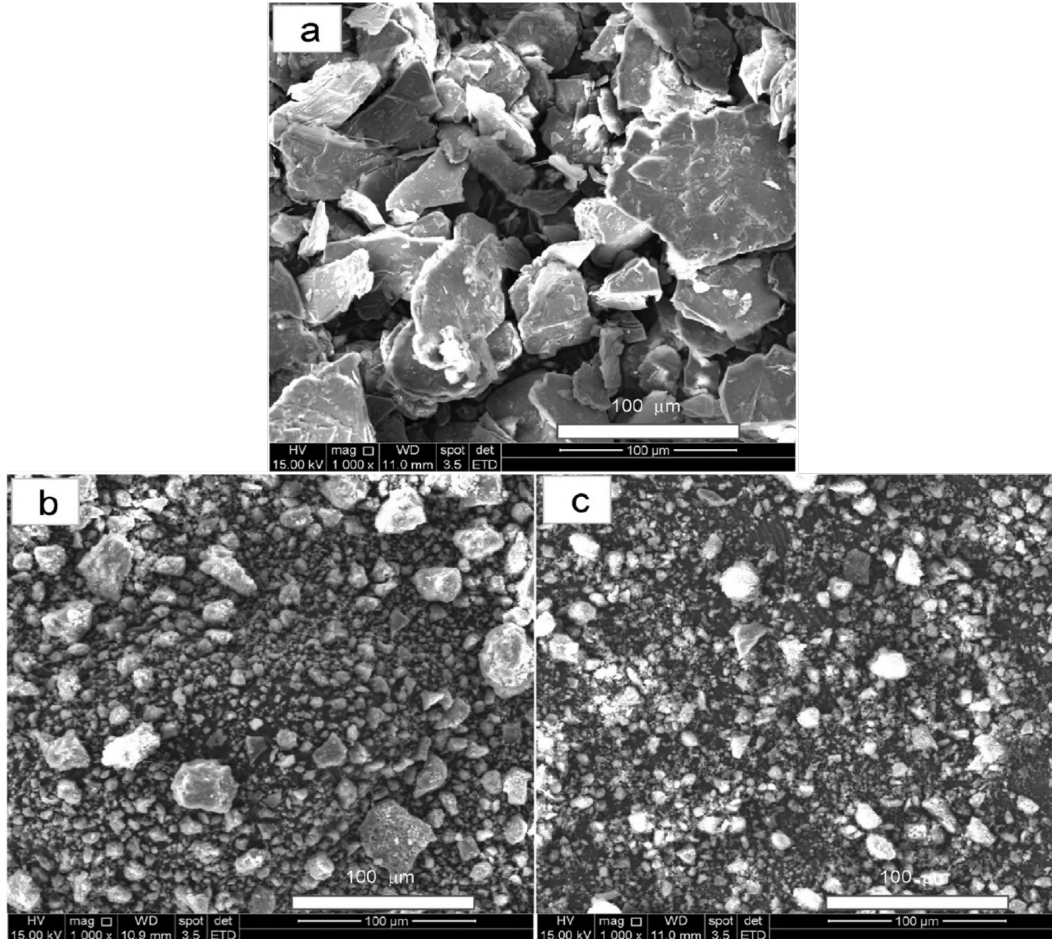


Figure 2.26: SEM morphologies of the talcs under 1kx of magnification (a) TN, (b) NTC and (c) NTA [53].

Table 2.13: Mechanical properties of HDPE/talc composites [53].

Samples	Tensile modulus (MPa)	Tensile strength (MPa)	Elongation at break (%)
HDPE	426 ± 25	25.3 ± 0.6	158 ± 23
HDPE/TN	432 ± 39	23.4 ± 0.7	141 ± 14
HDPE/NTC	428 ± 42	23.9 ± 0.3	158 ± 26
HDPE/NTA	445 ± 26	24.3 ± 0.2	237 ± 30

In summary, it can be noted that the resulting mechanical behavior of talc-filled polyethylene is not only dependent of filler content, but it is intrinsically related to the morphology of the particles, its distribution throughout the matrix and the amount of interfacial bonding formed between matrix and filler during the compounding of the composites.

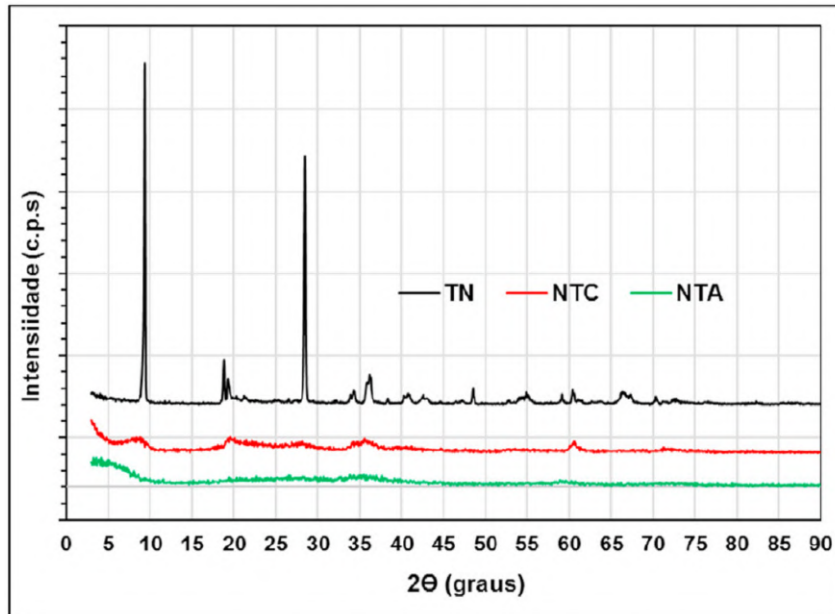


Figure 2.27: XRD patterns of natural microtalc (TN), semi-crystalline synthetic nanotalc (NTC) and amorphous synthetic nanotalc (NTA) used in the HDPE composites [53].

2.3.3 Creep Behavior

Creep is a time- and temperature-dependent phenomenon characterized by a slow, continuous deformation of a material under constant load or stress [54]. Since it can occur at stress levels significantly lower than the yield strength, the creep phenomenon has a great impact on the dimensional stability and load-bearing capacity of end-products [54, 55]. Thermoplastics, unlike metallic materials, are susceptible to creep failure even at room temperature, depending on the polymer's glass transition temperature (T_g) [56]. Therefore, assessment of durability is an essential step in the design of plastic products, as to prevent premature failures and to avoid intolerably large deformations [55, 57].

In general, creep testing consists on submitting the specimen to constant load or tension (usually tensile tension) while the strain is measured as a function of time. The tests are conducted under constant temperature. Constant-load tests are more often applied because they generate information that can be directly used in engineering practice. Constant-tension tests are applied for research purposes in order to have a better understanding of the mechanisms behind the creep phenomenon [37]. In general, the assessment of the creep life-time of a material requires long duration tests, which presents practical limitations. However, it is possible to predict the long-term practi-

cal conditions by extrapolating the data from short-term creep tests, obtained under accelerated testing conditions, such as higher temperature, stress, and humidity [57]. This extrapolation can be obtained by representative viscoelastic models, which will be revised in Section 2.4.2.

The typical creep response to a constant stress applied at time $t = 0$ is shown in Fig. 2.28. An instantaneous deformation (ϵ_0) proportional to the applied stress is observed after the application of the stress and this is followed by a progressive increase in strain [54]. In theory, creep behavior can be divided into three stages: primary, secondary and tertiary. In the first stage, the material undergoes deformation at a decreasing rate, followed by a steady-state linear deformation stage, known as secondary creep stage, for which the experimental data is typically of most interest. [57]. In the case of semi-crystalline polymers such as polyethylene, the primary stage is caused by the realignment of the amorphous phase and the elongation (partly elastic and partly delayed elastic) is reversible. In the secondary stage, steady creep takes place, in which molecular chains slide along each other, causing irreversible elongation at minimum creep rate. Finally, in the tertiary stage, molecular chains start to break, local stresses increase and the creep rupture process is accelerated [54].

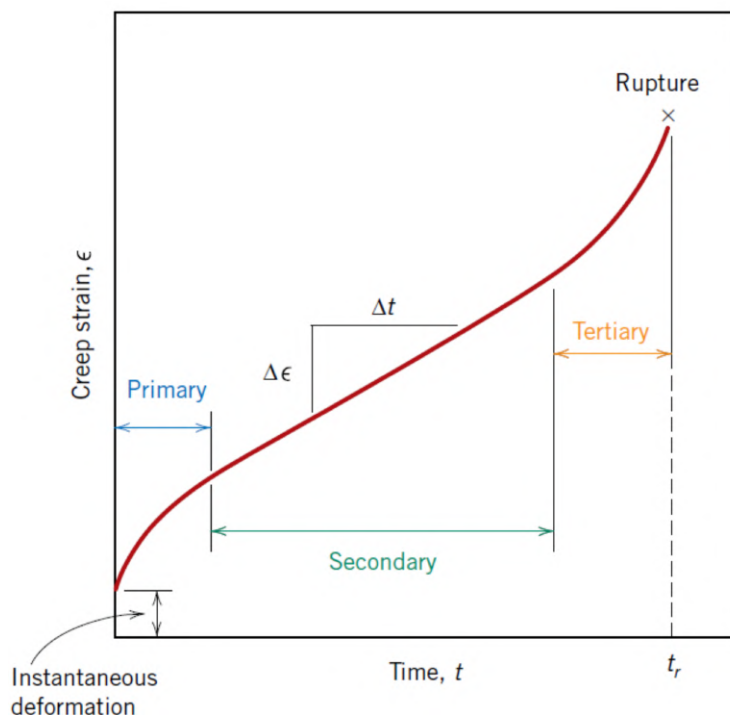


Figure 2.28: Typical creep curve of strain versus time at constant load. The minimum creep rate $\Delta\epsilon/\Delta t$ is the slope of the linear segment in the secondary region. Rupture time t_r is the total time to rupture [37].

The creep behavior of polyolefins is substantially influenced by the mor-

phology formed during processing. The creep properties of polyethylene in particular are influenced by the presence of long chains which make the material softer and less creep resistant. However, it was found that long chains can increase the resistance to brittle failure under very long-term creep conditions [54]. Additionally, the processing conditions can substantially influence creep response, since the obtained degree of crystallinity influences the deformation mechanism that takes place. Nitta et al. [58] observed that, at temperatures well above T_g and creep strains below the yield point of the material, the creep behavior of HDPE is controlled by the deformation of the amorphous phase and an increase on the amorphous phase fraction enhances the overall molecular mobility of HDPE. In contrast, creep at high stress is controlled by the deformation of the crystalline phase, with less molecular mobility, which can lead to a different failure mechanism.

In general, the failure mechanism in a sample of polyethylene varies widely with the conditions of stress and temperature, the molecular weight distribution, the environment and the previous thermal history of the polymer [59]. The failure mechanism is traditionally described as occurring in either a brittle or ductile manner. However, Hin et al. [59] further divided the rupture behavior of HDPE into four types, shown in Fig. 2.29, according to the amount of tertiary creep, necking and cold drawing which take place during the failure process. In Type A, failure occurs in a ductile manner, the specimens show macro-necking and generally the total strain to rupture exceeds 35%. Type A tertiary creep was further subdivided into Type A1 and Type A2 creep rupture on the basis that a specimen exhibiting Type A1 failure presents the prolongation of the macro-neck (cold drawing) after yielding and only subsequently fractures, as can be seen in the specimen showed in Fig. 2.29. Meanwhile, Type A2 rupture fractures immediately after macro-necking with no intervening cold drawing. Microscopically, cold drawing is characterized by the continuation of molecular alignment, as shown in Fig. 2.30, that results in the orientation of the crystalline units in the neck region [60].

Brittle creep rupture is characterized by a low strain to failure, no macro-necking formation and a plane of fracture perpendicular to the tensile axis. The classification into type B or C was based on whether tertiary creep was a feature of the brittle failure process. Specimens which ruptured at a low strain (typically below 13% longitudinal strain) and show no tertiary creep were classified as Type C failures, whereas specimens which demonstrated some tertiary creep but otherwise behave in a brittle manner were classified as Type B creep rupture failures [59].

By analysing HDPE samples processed with different cooling conditions,

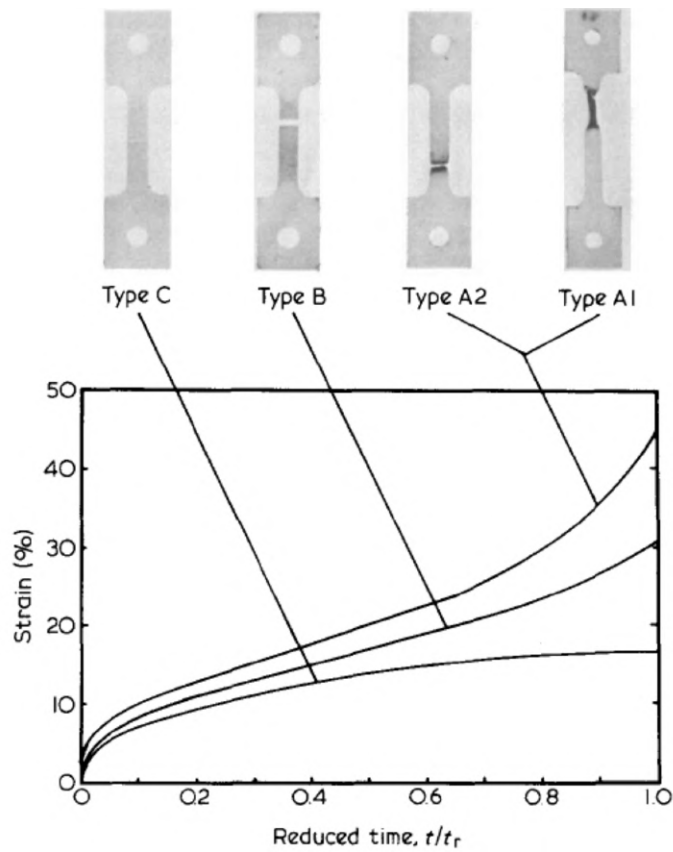


Figure 2.29: Schematic illustration of the four types of creep rupture behaviour in HDPE [59].

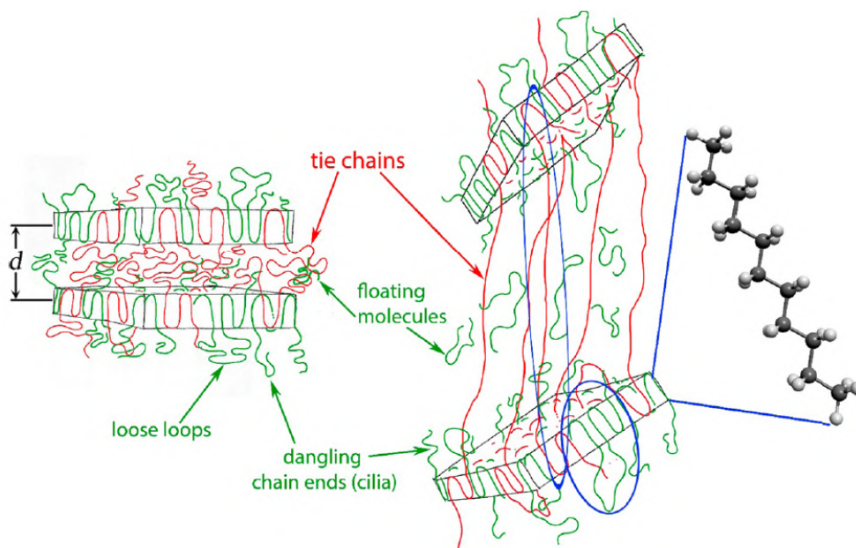


Figure 2.30: Schematic of the molecular alignment during cold drawing of a semicrystalline polymer. The strong alignment of the tie chains is highlighted. [60].

Hin et al. [59] observed that creep rupture exhibited by HDPE is substantially dependent on the morphology, which is in turn a function of molecular weight and crystallization conditions. Compressed molded HDPE specimens were either left to cool to room temperature, or water quenched to 70°C. The different cooling processes led to considerable differences in morphology, as shown in Fig. 2.31. The morphology of the air-cooled was formed by degenerated spherulitic structures while the water-quenched specimens were formed by a banded spherulitic structure. The air-cooled specimens presented only brittle creep rupture for all stress levels. For the water-quenched specimens at high (greater than 22 MPa) and low (less than 14MPa) stresses only brittle creep rupture was observed. However, at intermediate stress levels (between 14 and 22 MPa) both brittle and ductile creep rupture were observed. For the same stress level the air-cooled (degenerated spherulitic) material gave longer rupture time than the water-quenched (banded spherulitic) material [59].

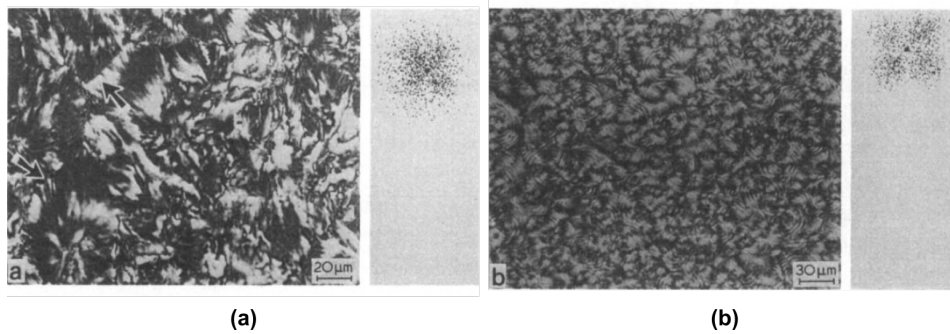


Figure 2.31: (a) Morphology of the air-cooled specimens, degenerated spherulites are indicated by arrowheads. (b) Morphology of the water-quenched specimens [59].

In his study of HDPE/PA12 blends, Silva [61] analysed the creep behavior of five neat HDPE specimens at room temperature and under constant load of 118N, which corresponded to approximately 50% of the yield stress (≈ 12 MPa) of the material. The tests lasted 24 hours. Figure 2.32 exhibits the characteristic creep behavior obtained, as can be seen the specimens did not present tertiary creep or rupture under the test conditions. The mean value obtained for the instantaneous strain ($t=0$) was 0.050 ± 0.005 mm/mm. The author also determined the creep rate in a series of time intervals in order to evaluate whether the stationary creep was achieved. The values obtained are listed in Tab. 2.14, where is possible to observe that, from the 8h-12h interval onward, the values have very small variations, hence the stationary creep was achieved by 8h of test under 118N [61].

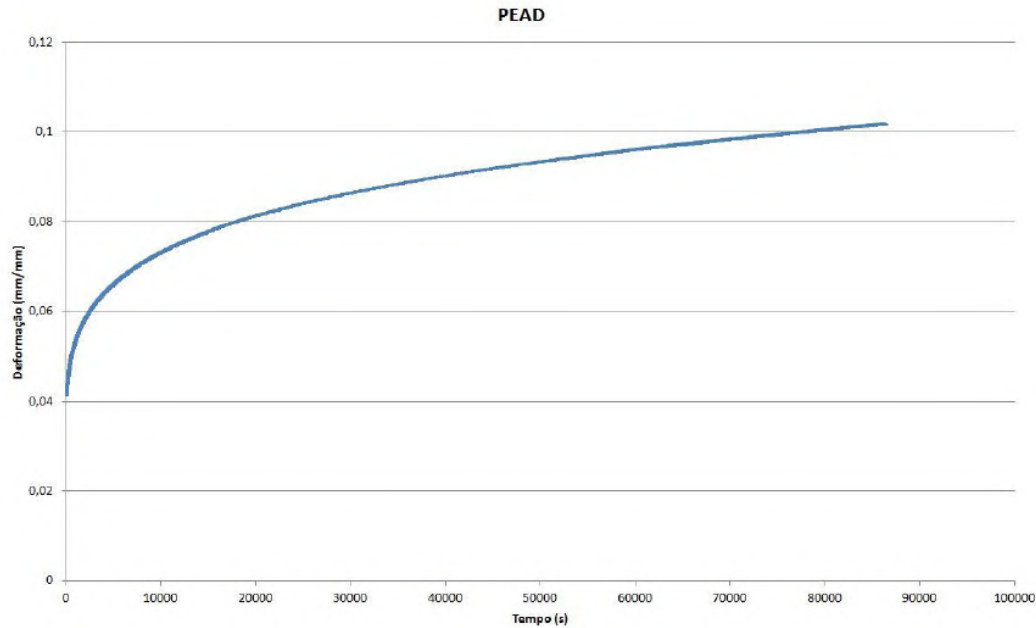


Figure 2.32: Strain vs. time curve for one of the specimens HDPE tested by Silva [61].

Table 2.14: Mean creep rate obtained for HDPE under 118N constant load at room temperature [61].

Time Interval	Creep rate $\times 10^{-7}$ (s^{-1})
2h – 4h	9.89 ± 1.40
4h – 8h	5.42 ± 0.96
8h – 12h	3.41 ± 0.69
12h – 16h	2.61 ± 0.60
16h – 20h	2.15 ± 0.55
20h – 24h	1.95 ± 0.62

Pereira et al. [62] studied the short-time creep behavior of HDPE after aging in oil derivatives. The authors determined viscoelastic properties, the steady creep rate and compliance of the HDPE before and after aging. The tests were conducted with a constant tension load of 30 N, simulating an initial stress of approximately 3 MPa, since the cross section area of the samples was 9.90 mm^2 . The load was applied within 5 to 10 s, so it can be considered as an instantaneous load. The tests lasted 10 min. Three specimen were used per condition at room temperature. The steady-state creep rate obtained for each condition of the HDPE is listed in Tab. 2.15. The creep compliance was determined in order to understand the effect of absorption of fluids in HDPE as a function of the immersion time. The compliance over time, $J(t)$, can be calculated by the ratio between time dependent strain and the constant applied stress ($J(t) = \frac{\epsilon(t)}{\sigma_0}$). These results are shown in Fig. 2.33, where it can be noted that compliance increased with the load application time, and its maximum values were obtained by samples aged in gasoline [62].

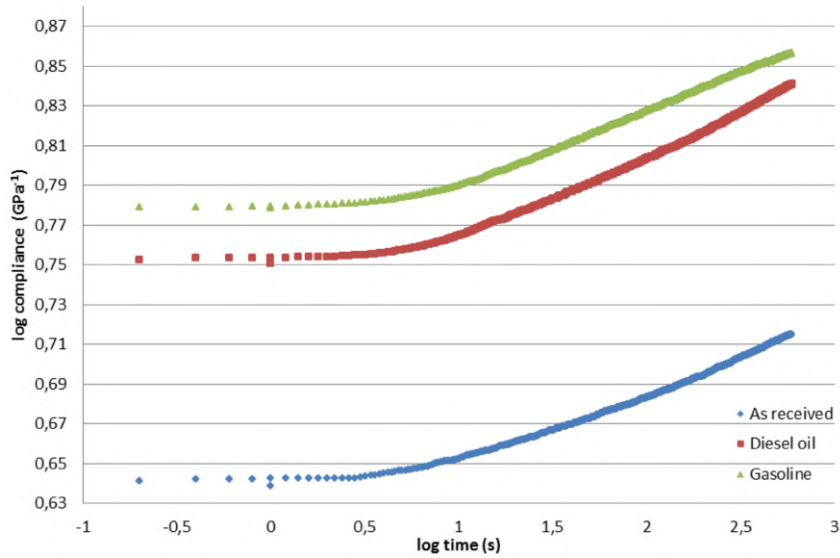


Figure 2.33: Compliance comparison between as-received and aged HDPE [62].

Table 2.15: Rates of steady-state creep for as-received and aged HDPE [62]

	As-received	Diesel oil	Gasoline
Creep Rate $\dot{\epsilon} \times 10^{-6} (s^{-1})$	2.22	3.40	2.52

The results obtained by Pereira et al. [62] showed that the samples aged in oil derivatives showed higher instantaneous strain and viscous flow, and therefore greater viscous strain, than the as-received samples. The aged samples also presented higher creep rates, which implies in shorter lifetimes than the unaged material. The relevance of this work lies in proving that aging effects can be analysed using short term creep tests, speeding the evaluation of how aggressive a working fluid can be in respect to HDPE parts [62].

The literature regarding the creep behavior of particulate-filled semi-crystalline polymers is still under development, not many papers reporting similar materials were found. In general, the effect of the addition of fillers to the creep behavior of a polymeric matrix depends on factors such as the creep behavior of the polymer, elastic and fracture behavior of the filler, geometry and arrangement of the filler, and the filler-matrix interfacial properties. Mechanisms such as load transfer from the matrix to the filler and residual stresses caused by the difference in thermal expansion coefficients between phases should be considered simultaneously, thus the analysis and prediction of such behavior is a complex subject [54].

Ek et al. [63] investigated the effect of filling high density polyethylene (HDPE) with calcium carbonate (up to 50% by weight) on the stress relaxation and the creep in uniaxial extension at room temperature. The addition of

$CaCO_3$ was found to have a strong influence on the flow behavior of HDPE. The filled samples presented lower creep rates, which suggested that the $CaCO_3$ particles induce a change in the structure of the HDPE in the inter-phase close to the filler surface [63].

In a more recent work, Eftekhari et al. [57] investigated the creep behavior of neat, talc-filled, and short glass fiber reinforced injection molded thermoplastic composites at room and elevated temperatures. The neat thermoplastic used was an impact polypropylene copolymer. Two types of talc-filled composites were used: a polypropylene-elastomer blend with 25% by weight of elastomer and 35wt% talc and a 40wt% talc filled polypropylene. The tests conditions are listed in Tab. 2.16, the tests were done in transversal direction [57].

Table 2.16: Materials and conditions used for the experimental creep test [57]

Polymer Matrix	Reinforcement	T_m (°C)	T_g (°C)	Temperatures studied (°C)	Stress range studied*
Polypropylene + 25 wt% Rubber	30 wt% Talc	> 120	< -10	23, 85, 125	30-82
Impact Polypropylene	None	170	4	23, 85, 125	40-85
Polypropylene	40 wt% Talc	165	11	23, 85	53-80
Polypropylene	30 wt% Short Glass Fiber	165	23	23, 85, 120	46-85

*(% Ultimate tensile strength).

The experimental behavior revealed that temperature significantly affected creep behavior of both the neat polymer and the composites tested. For polypropylene composites, the type of reinforcement (talc or short glass fiber) had the same effect on creep deformation. Reinforcement or filler did not change the creep mechanism noticeably and only resulted in improved creep strength (i.e. reduction of both creep strain and rate), as compared to the neat polymer [57].

2.4 Mechanical Models for Polymeric Composites

In order to predict the effects of the filler in the practical mechanical and long-term behavior of the polymer, the theoretical modeling of these behaviors are of great importance. Predictive models, as well as experimental results that validated some of those theories, have been reviewed in the following sections. In Section 2.4.1, theories regarding the prediction of the tensile strength and elastic modulus of particulate composites as a function of the filler content are studied. While in Section 2.4.2, viscoelastic models that aim to describe the creep behavior of polymers and polymeric composites are reviewed.

2.4.1 Tensile Properties

2.4.1.1 Theories for Young's Modulus

A variety of empirical and semi-empirical equations have been proposed in order to model the modulus of particulate composite materials. Einstein's equation [64] is one of the simplest models in the literature. It predicts a linear relation between the relative modulus and the filler content as follows:

$$E_c/E_m = 1 + 2.5\phi_p \quad (2-2)$$

where E is the elastic modulus. This model assumes perfect filler-matrix adhesion and perfect dispersion of individual filler particles. Therefore, this equation is valid only for low filler concentrations. Guth [65] generalized the Einstein equation by introducing a particle interaction term, as follows:

$$E_c/E_m = 1 + 2.5\phi_p + 14.1\phi_p^2 \quad (2-3)$$

where the linear term is the stiffening effect of individual particles and the second power term accounts for the contribution of particle interaction [66]. For non-spherical particles Eq. (2-3) was modified to include a shape factor p , as follows :

$$E_c/E_m = 1 + 0.67p\phi_p + 1.62p^2\phi_p^2 \quad (2-4)$$

where p is defined as the ratio of particle length to width and assumed to be greater than 1 [42]. Mooney [67] made a different modification to the Einstein equation:

$$E_c/E_m = \exp\left(\frac{2.5\phi_p}{1 - s\phi_p}\right) \quad (2-5)$$

where s is a "crowding factor" that takes into account first order interactions between particles. Geometrically, s is the ratio of the apparent volume occupied by the particle to its true volume, and its value lies between 1.0 and 2.0 [66]. For non-spherical particles, the Mooney equation was further modified according to Brodnyan [68]:

$$E_c/E_m = \exp\left(\frac{2.5\phi_p + 0.407(P - 1)^{1.508}\phi_p}{1 - s\phi_p}\right) \quad (2-6)$$

where P is the aspect ratio of the particle and $1 < P < 15$. When $P = 1$, Eq. (2-6) becomes Eq. (2-5).

Halpin [69] found that the following semi-empirical relationship can predict the modulus of particulate polymers:

$$E_c/E_m = \frac{1 + A'B'\phi_p}{1 - B'\phi_p} \quad (2-7)$$

where A' and B' are constants for a given composite. The constant A' takes into account factors such the geometry of the filler and the Poisson's ratio of the matrix, and can be related to the generalized Einstein coefficient k as follows:

$$A' = k - 1 \quad (2-8)$$

For a suspension of rigid spheres in a matrix with a Poisson's ratio of 0.50, $k = 2.5$. B' takes into account the relative moduli of the particulate filler and matrix phases, as follows [70]:

$$B' = \frac{E_p/E_m - 1}{E_p/E_m - A'} \quad (2-9)$$

Nielsen [71] proposed another form of Eq. (2-7) that takes into account the maximum packing fraction of the filler (ϕ_{max}):

$$E_c/E_m = \frac{1 + A'B'\phi_p}{1 - B'\psi\phi_p} \quad (2-10)$$

where ψ is defined as:

$$\psi = 1 + \left(\frac{1 - \phi_{max}}{\phi_{max}^2} \right) \phi_p \quad (2-11)$$

Values for the shape factor, A' , for several filler types are listed in Tab. 2.17, while values of the maximum packing fraction, ϕ_m , for different packing geometries can be found in Tab. 2.18 [49].

Table 2.17: Shape Factors for Several Filler Type [49].

Filler type	Aspect Ratio	A'
Spheres	1	1.5
Cubes	1	2.0
Random fibers	2	1.58
Random fibers	5	2.45
Random fibers	10	4.93

Bigg [49] determined the relative elastic modulus of several systems and the results were compared with the curve generated by the equation (2-10) proposed by Nielsen [72]. The reinforcements used include minerals, such as talc and silicon carbide, and metals, such as aluminum flakes and stainless steel fibers. The polymers used were General Electric's Noryl resin, acrylonitrile-butadiene-styrene (ABS), polypropylene and modified polypropylene. The

Table 2.18: Maximum packing fraction of selected fillers [49].

Filler type	Packing geometry	ϕ_m
Spheres	Hexagonal	0.74
Spheres	Face centered cubic	0.74
Spheres	Body centered cubic	0.60
Spheres	Simple cubic	0.52
Spheres	Random	0.637
Irregular	Random	0.637
Fibers	Random (L/D = 5:1)	0.52
Fibers	Random (L/D = 20:1)	0.20
Fibers	Unidirectional random	0.637
Flake	Random (L/t = 56:1)	0.33

talca and part of the aluminum flakes were treated with coupling agents to improve adhesion to polymers. The relative modulus data for all of the systems investigated are shown in Fig. 2.34, where Nielsen's equation was used to fit the data. A value of 2.00 was used for the A' coefficient and a maximum packing fraction of 0.50 assumed. The tensile modulus increased with filler content for all systems. However, by observing Nielsen's equation the authors concluded that, at 30 vol% filler loading, additional increases in filler concentration have only a small effect on the composite modulus.

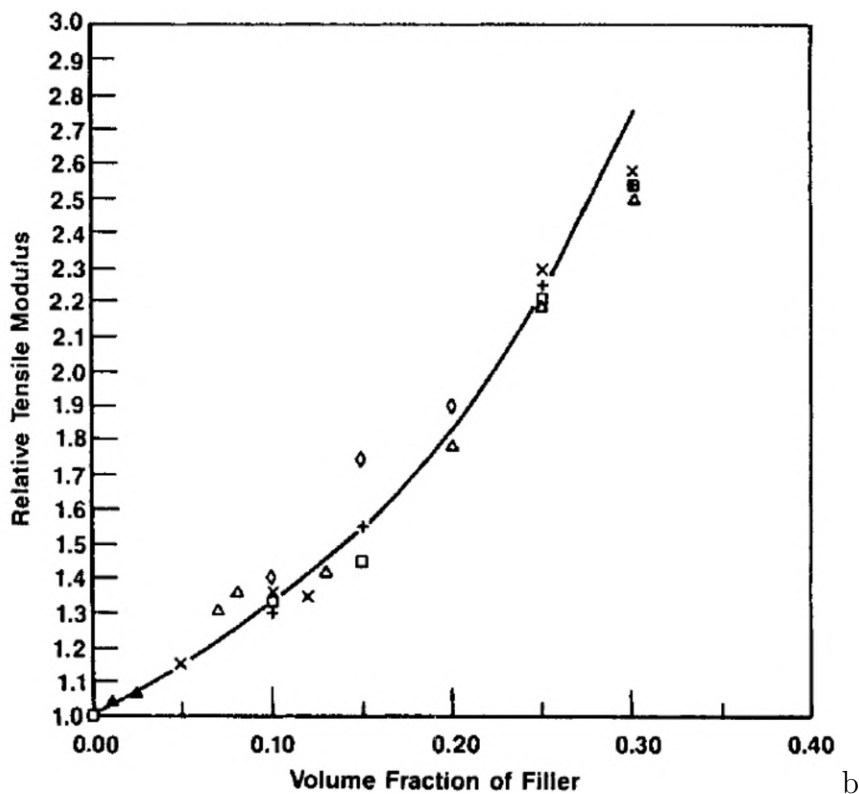


Figure 2.34: Fitting of the Nielsen equation for the relative modulus vs. filler concentration for: + Noryl-talc; □ ABS-talc, ◇ PP-SiC, × modified PP-aluminum flake, △ PP-aluminum flake, ▲ PP-steel fibers [49].

2.4.1.2 Theories for Strength

The ultimate strength of a composite depends on the weakest fracture path throughout the material. The addition of particles can affect the strength in two ways. One is the weakening effect due to the stress concentration caused by the particles, and the other is the reinforcing effect since they may serve as barriers to crack growth [66]. Whether or not the filler will increase the polymer strength will depend on which effect is predominant.

The theoretical prediction of the strength of composites is usually a more complicated task than that of the elastic modulus. The strength of composites is determined by the fracture behaviours, which are associated with the extreme values of such parameters as interface adhesion, stress concentration and defect size/spacial distributions [66]. Although interfacial adhesion is of primary importance for load transfer between the phases, it is a parameter difficult to measure. Thus, it is often inferred only qualitatively by examining the interfacial aspects at fracture surfaces or simply by measuring whether or not the mechanical properties of the composite are greater than those of the matrix [73].

The degree of the interfacial bonding is usually divided into poor adhesion, good adhesion and some adhesion [50]. In the case of poor adhesion, the interface will act as an inherent flaw as the deformation proceeds and a lower bound response is observed [42]. In the case of good filler-matrix adhesion, the stress is transferred between phases through shear and the filler has an reinforcing effect on the matrix properties. Thus an upper bound response is observed [50]. Leidner and Woodhams [74] proposed the following equation for an upper bound response of a polymer filled with spherical particles:

$$\sigma_{yc} = (\sigma_i + C\tau_m)\phi_p + K\sigma_i(1 - \phi_p) \quad (2-12)$$

where σ_y is the tensile yield strength, σ_i is the interfacial tensile strength between polymer and filler, K is the relative change of the strength of the matrix due to the presence of the filler, C is a constant determined to be 0.83 and τ_m is the shear strength of the matrix. Bigg [49] proposed an alternative representation for this upper bound response with the following empirical equation:

$$\sigma_{yc} = \sigma_{ym}(1 - a\phi_p^b + c\phi_p^d) \quad (2-13)$$

where a is a constant related to stress concentration and b is a constant related to the geometry of the filler. For spherical particles having no adhesion to the polymer matrix, the value of a has been found to be equal to 1.21. When there

is some adhesion between phases, there is less stress induced in the polymer by the filler and the value of a is less than 1.21 [49]. The value of b is determined by the fracture mode, it has been found to be equal to 1.00 when the sample fails by random fracture which probably propagates throughout the matrix, while in the case of fracture which goes through the filler-matrix interface, b equals 2/3 [49, 52]. The parameters c and d are adjustable constants that can lead to some insight into the degree of adhesion between the polymer and filler.

The equation proposed by Bigg [49] was used to fit the strength at break data of the various thermoplastic composite systems previously described. The resulting curves are shown in Fig. 2.35. It can be seen that talc increased the tensile strength of Noryl at all concentrations up to 30 vol%. While, there was only a slight amount of tensile strength reinforcement for the ABS-talc composites, which peaked at low talc concentrations, around 10 vol%. At concentrations above 20 vol% the tensile strength of the filled ABS was lower than that of the unfilled polymer. The results lead to the conclusion that the adhesion between Noryl and talc was greater than the adhesion between ABS and talc.

The SiC filled polypropylene composites showed a lower bound response, hence the filler had a negative effect of the polymer's strength. While in the talc filled compositions, reinforcement was observed and the responses followed an upper bound curve. The coefficients calculated for the talc systems are listed in Tab. 2.19 to serve as reference for the present work.

Table 2.19: Calculated Coefficients for Upper and Lower Bound Equations [49].

Polymer	Filler	a	b	c	d
Noryl	Talc	0.80	0.67	1.30	0.50
ABS	Talc	1.18	0.67	0.67	0.33

Turcsányi et al. [41] proposed a more general approach for the yield stress of particulate composites with the following semi-empiric equation:

$$\sigma_{yc} = \frac{1 - \phi_p}{1 + A\phi_p} \sigma_{ym} \exp(B\phi_p) \quad (2-14)$$

where A is a shape factor, related to the spacial distribution of the filler and B is an adimensional parameter directly related to the particle-matrix adhesion and it can be used to provide a quantitative characterization of the interfacial adhesion. If $B = 0$, there is no adhesion and, consequentially, there is no load transfer in the interface. For values of $B \geq 3$ there is some matrix-filler adhesion and a reinforcement effect [41].

Experiments done by d'Almeida et al. [51] showed that the relation proposed by Turcsányi et al. [41], Eq. (2-14), can also be used to describe

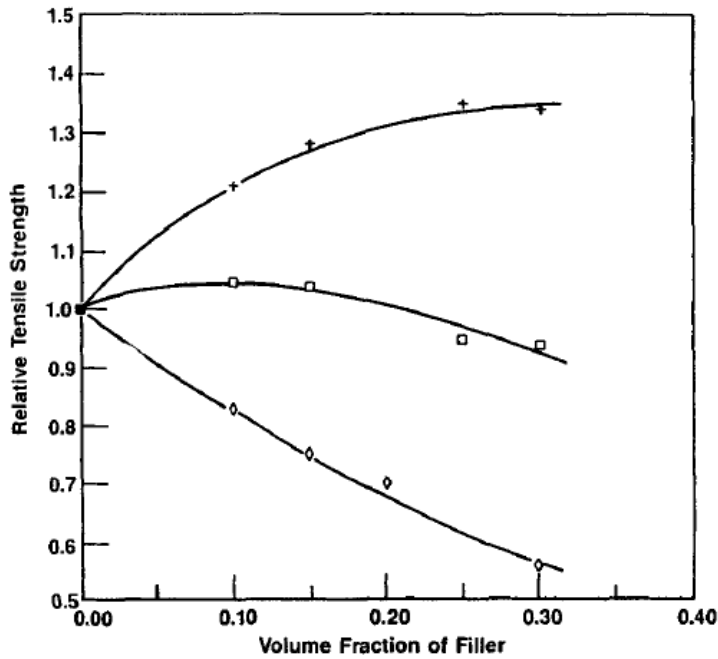


Figure 2.35: Fitting for the relative tensile strength of polymers with non-metallic fillers. + Noryl-talc, \square ABS-talc, \diamond PP-SiC [49].

the ultimate strength of a group of particulate composites, according to the following modification:

$$\sigma_{uc} = \frac{1 - \Phi}{1 + A\Phi} \sigma_{up} \exp(B\Phi) \quad (2-15)$$

where σ_u is the ultimate tensile strength, that for many polymers correspond also to the strength at break. This approach is only valid for composites that present fragile fracture, i.e., the fracture occurs without considerable macroscopic deformation.

In order to verify the applicability of Eq. (2-15), composites with four different polymeric matrices and various filler types were manufactured and submitted to tensile testing. The polymers used were polypropylene (PP) and high- (HDPE), medium- (MDPE) and low-density polyethylene (LDPE). As fillers, particles of calcium carbonate, atapulgite, sepiolite and short length sisal fibers up to 75 μm long were used. In order to vary the adhesion between filler and resin, atapulgite filled composites were also made with treated particles. The surface treatment agents employed were γ -aminopropylmetoxysilane and isopropil-triisostearyl titanate (KRTTS). Both were used at a concentration of 1% by weight. The sepiolite particles were treated with a solution of hydrochloric acid. Values for the B parameters were obtained for the composites tested and used to judge whether the surface treatment effectively enhanced the adhesion between phases [51].

The experimental results for the HDPE, MDPE and LDPE were well fitted by the modified Eq. (2-15). The parameters A and B , and the ultimate polymer strength, σ_{up} were set as adjustable variables. The PP composites showed large plastic deformations, and thus the experimental data for this material could not be fitted by the model proposed, as the primary boundary condition was not satisfied. The adjusted curves for the HDPE composites are shown in Fig. 2.36, the experimental data is listed in Tab. 2.20 and the values obtained for the adjustable parameters are listed in Tab. 2.21 [51].

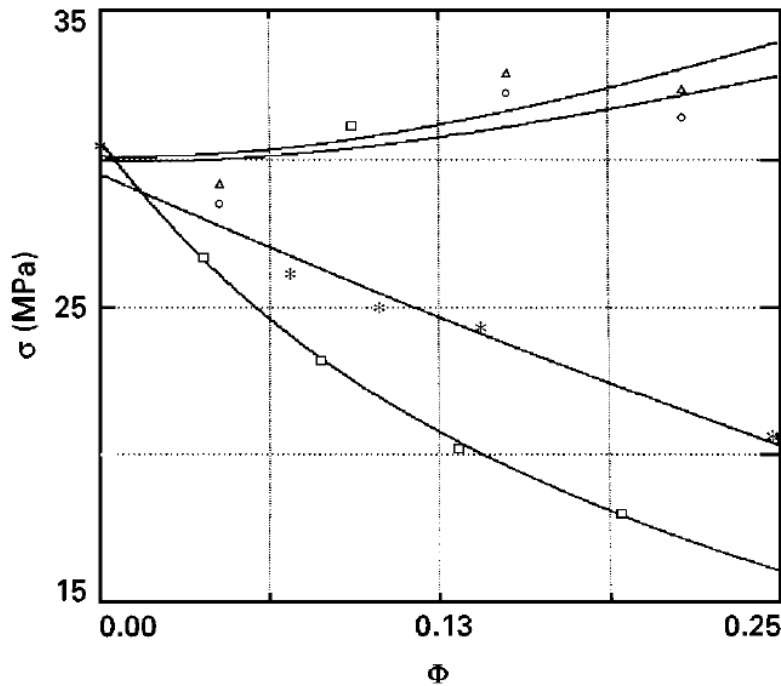


Figure 2.36: Fitting procedure for HDPE composite: (○) atapulgitite, (△) atapulgitite + silane, (□) CaCO₃, (*) sisal [51].

Table 2.20: Ultimate tensile strength (MPa) of HDPE particulate composites [51].

Volume fraction	Atapulgitite	Atap. + silane	Volume fraction	CaCO ₃	Volume fraction	Sisal
0	30.4	30.4	0	30.4	0	30.4
4.4	28.5	29.1	3.8	26.7	6.8	25.8
9.3	31.0	31.0	8.2	23.2	10.4	25.0
15.0	32.2	32.8	13.2	20.2	14.1	24.3
21.6	31.4	32.3	19.2	18.0	24.7	20.6

The values of the B parameter, listed in Tab. 2.21, can serve as a quantitative measure of the particle reinforcement efficiency. In addition, it can be used for a more systematic analysis of the effect of surface treatment upon adhesion between phases. For instance, it can be seen from Tables 2.20 and 2.21 that, for the composites evaluated, the treatment of the atapulgitite particles

Table 2.21: Values of the parameters adjusted to the modified eq. 2-15 for HDPE [51].

Parameters	Atapulgit	Atap. + silane	CaCO ₃	Sisal
σ_{up} (MPa)	29.91	30.09	30.48	29.45
A	2.49	2.85	4.73	0.58
B	3.45	3.78	1.70	0.21
r	0.630	0.786	0.999	0.978

with a silane coupling agent produced only a secondary effect upon the filler-matrix adhesion and, consequentially, upon the properties of the composites [51]. It is important to note, however, that the composites that showed higher values of the B parameter, also presented lower correlation coefficients (r) and therefore, had worse fitting of the model.

2.4.2

Viscoelastic Models

As previously mentioned, the data from a short-term creep testing, obtained under accelerated testing conditions, such as higher temperature, stress, and humidity, can often be extrapolated by representative viscoelastic models in order to predict long-term practical conditions [57]. These models characterize an intermediate behavior between elastic solid and Newtonian flow. Owing to the complex coupling of the crystalline and amorphous phases, the mechanical behavior of a semi-crystalline polymer is more complicated to model than that of an amorphous polymer [55].

The high linearity exhibited by HDPE guarantees a more efficient alignment and packing of chains, which results in high levels of crystallinity. HDPE shows two types of viscoelastic behavior when under creep, namely: linear and nonlinear. Linear behavior is often found in short load application times while nonlinear behavior is found for long load application times. Both behaviors are characterized by strain dependence on temperature and on the applied load. The duality of behaviors from HDPE can be linked to its semi-crystalline morphology, where the crystalline regions show linear behavior and the amorphous phase plays a significant role in nonlinear behavior [62].

A particularly useful method of formulating the combination of elastic and viscous behavior is through mechanical models. The two basic components used in these models are an elastic spring of modulus E , which obeys Hooke's law, Eq. (2-16), and a viscous damper containing an incompressible fluid of viscosity η , which obeys Newton's law, Eq. (2-17).

$$\sigma = E\epsilon \quad (2-16)$$

$$\sigma = \eta \frac{d\epsilon}{dt} \quad (2-17)$$

The various models that have been proposed involve different combinations of these two basic elements. Most of them are based on simple models like the Maxwell Model, that consists of a spring and damper in series, and the Kelvin-Voigt Model (KV), that consists of the same elements arranged in parallel [75].

The Standard Linear Solid Model, or Three Parameters Model, was proposed in order to reduce the limitations presented by the KV Model by introducing a spring in series to the KV schematics, as shown in Fig. 2.37. This extra spring represents the immediate strain observed when an instantaneous load is applied to the material. The strain over time is given by Eq. (2-18) [62]:

$$\epsilon(t) = \frac{\sigma_0}{E_1} + \frac{\sigma_0}{E_2} \left(1 - \exp\left(-\frac{E_2 t}{\eta}\right) \right) \quad (2-18)$$

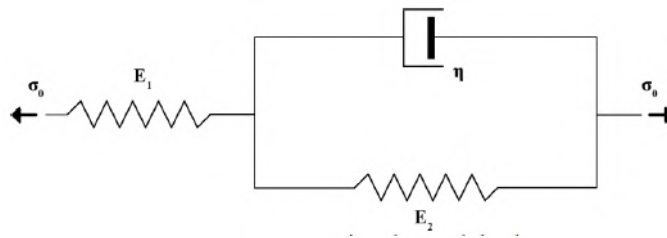


Figure 2.37: Standard Linear Solid Model schematic representation [76].

where t represents the time after the loading, σ_0 the constant applied stress during the loading and $\epsilon(t)$ the resulting strain at instant t . The three adjustable parameters are the the elastic modulus of the parallel spring (E_2), the viscosity of the damper (η) and the elastic modulus of the spring in series (E_1) [62].

The Burgers Model, also called the Four Parameters Model, is composed by the combination of the KV Model with the Maxwell model, as shown in Fig. 2.38. The creep behavior according to this model is given by Eq. (2-19) [62]:

$$\epsilon(t) = \frac{\sigma_0}{E_1} + \frac{\sigma_0}{\eta_1} t + \frac{\sigma_0}{E_2} \left(1 - \exp\left(-\frac{t}{\tau}\right) \right) \quad (2-19)$$

where η_1 is the viscosity of the damper in series, η_2 the viscosity of the damper associated in parallel and τ represents the relaxation time, associated with the existing relation between the damper viscosity (η_2) and the spring elastic modulus (E_2) in the KV Model, given by the ratio between these variables (η_2/E_2) [62].

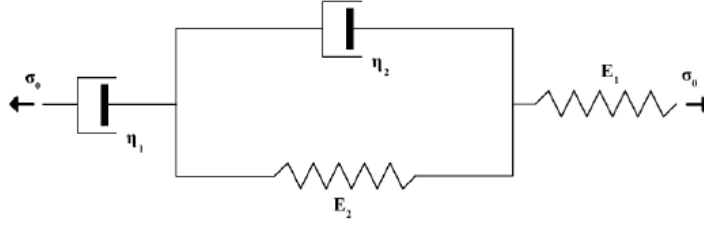


Figure 2.38: Burgers Model schematic representation [76].

The Stretched Burgers Model is based on the mathematical and schematic formulation of the Burgers Model, however, taking into consideration a distribution of relaxation times, instead of a single relaxation. It is assumed that recovery of the material is complete, therefore, schematically the additional damper is not connected in series with the system. The creep behavior in this case is described by Eq. (2-20) [62]:

$$\epsilon(t) = \frac{\sigma_0}{E_1} + \frac{\sigma_0}{E_2} \left(1 - \exp\left(-\left(\frac{t}{\tau}\right)^n\right) \right) \quad (2-20)$$

where the exponent n is determined by the width of the relaxation time distribution and τ is an average relaxation time associated with the spectral relaxation time distribution of the material [62].

The exponent n usually takes values between 0 and 1. This parameter can be used to understand the relaxation time distribution along the material. The closer n reaches 1 ($n \rightarrow 1$), greater is the uniformity shown by the relaxation spectrum, and so a single relaxation time is enough to describe the viscoelastic behavior of the material. However, if n reaches 0 ($n \rightarrow 0$), the width of the relaxation distribution becomes greater, and it is important to consider a spectrum of relaxation times [62].

The Findley Law is given by an empirical relation and it is usually applied to describe long-term creep behavior of polymeric materials. This model can be numerically represented by Eq. (2-21) [62]:

$$\epsilon(t) = \epsilon_0 + \epsilon_1 t^n \quad (2-21)$$

where ϵ_0 is the instantaneous strain, ϵ_1 is the amplitude of the transient strain and n is the time exponent, usually considered independent of strain, but dependent on material and temperature [62].

One of the advantages of Eq. (2-21) is its numerical simplicity. However, this simplicity can implicate in some application restrictions, for instance in the case of materials submitted to complex loadings. When compared to the other models, the Findley Law has a relevant graphical difference as its equation

suggest a constant strain growth while the other models predict an equilibrium plateau for long time creeps [62]. However, for a short time interval ($t < \tau$), the Stretched Burgers model can be reduced to Eq. (2-22), which behaves similarly to the Findley Model:

$$\epsilon(t) = \frac{\sigma_0}{E_1} + \frac{\sigma_0}{E_2\tau^n}t^n \quad (2-22)$$

Equating the terms σ_0/E_1 with ϵ_0 and $\sigma_0/E_2\tau^n$ with ϵ_1 , Eq. (2-22) becomes exactly the Findley Law equation [62].

In his study of HDPE/PA12 blends, Silva [61] performed the numerical fitting of neat HDPE strain-time response by non-linear regression associated with the least squares method. Three viscoelastic models were evaluated: the Standard Linear Solid, the Burgers and the Stretched Burgers Models. The latter presented the best fit to the experimental data, obtaining a higher correlation coefficient (r). A comparison between the fitted curves obtained by the three viscoelastic models is shown in Fig. 2.39, while the mean values of the obtained parameters are listed in Tab. 2.22 [61].

Table 2.22: Parameters obtained for the viscoelastic models for the HDPE specimens [61].

	Standard Linear Model		Burgers Model		Stretched Burgers Model	
	Mean	Standard Deviation	Mean	Standard Deviation	Mean	Standard Deviation
E_1 (Pa)	1.75E+08	1.55E+07	1.97E+08	1.74E+07	1.33E+09	1.81E+09
E_2 (Pa)	2.91E+08	6.27E+07	4.16E+08	5.59E+07	1.07E+07	8.98E+06
η_1 (Pa.s)	7.17E+12	6.56E+11	4.93E+13	1.61E+13	3.01E+18	4.36E+17
η_2 (Pa.s)	-	-	3.22E+12	5.55E+11	-	-
n	-	-	-	-	0.1749	0.0474
r	0.9747		0.9947		0.9991	

In their work Pereira et al. [62], used four viscoelastic models to assess changes in creep properties of the material, namely: Three Parameters model, Four Parameters model, Stretched Burgers model and Findley Law. The resulting parameters are listed in Tab. 2.23 and the fitted curves for the HDPE before and after aging in contact with gasoline and diesel oil are shown in Fig. 2.40.

As can be seen from Tab. 2.23, all models showed great numerical convergence with the experimental data, presenting high values of the correlation coefficient.

The Three Parameters model presented an excellent numerical convergence with the experimental data, but graphically it does not match the curve displayed by the data and the other models. The difficulty in reproducing the graphical behavior of the experimental data was linked to both the lack of parameters to describe the viscous permanent flow and the assumption of a single

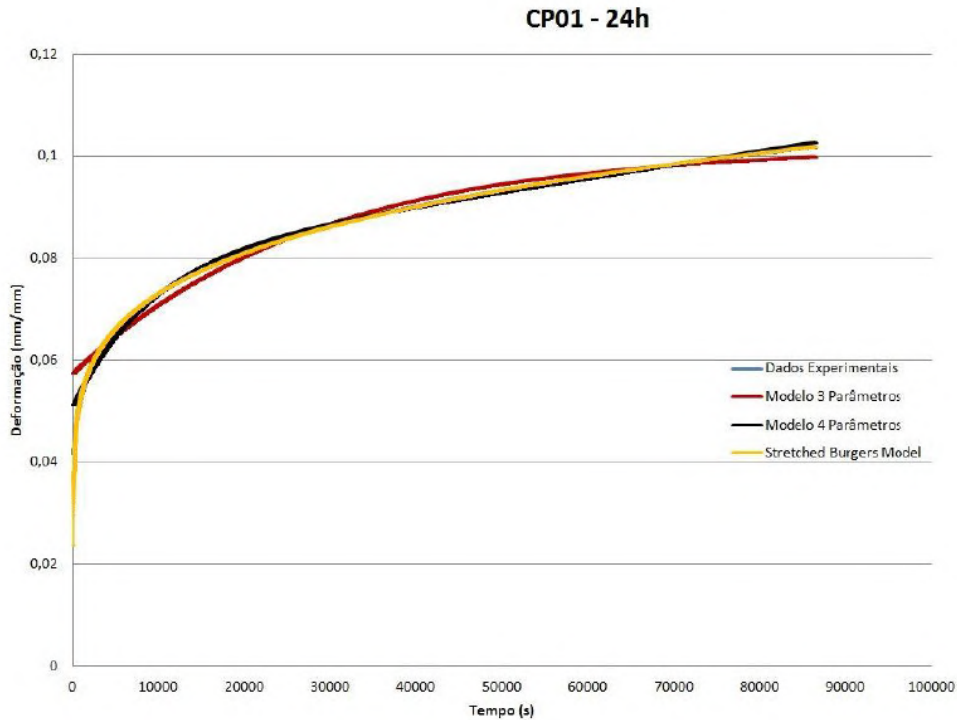


Figure 2.39: Comparison between the viscoelastic models and the creep test experimental strain-time data (in blue) for one HDPE specimen. In red the Three Parameters model, in black the Four Parameters model and in yellow the Stretched Burgers model [61].

Table 2.23: Parameters obtained for the viscoelastic models for the HDPE specimens [62].

		As-received	Diesel oil	Gasoline
Three Parameters Model (Standard Linear Model)	$E_1 \times 10^8 (Pa)$	2.27	1.71	1.62
	$E_2 \times 10^9 (Pa)$	1.53	0.95	1.04
	$\eta \times 10^{11} (Pa.s)$	3.45	1.87	1.48
	r	0.983	0.981	0.982
Four Parameters Model (Burgers Model)	$E_1 \times 10^8 (Pa)$	2.31	1.76	1.65
	$E_2 \times 10^9 (Pa)$	2.79	1.52	1.34
	$\eta_1 \times 10^{12} (Pa.s)$	1.78	1.06	1.58
	$\eta_2 \times 10^{11} (Pa.s)$	1.98	0.91	0.88
	r	0.996	0.996	0.996
Stretched Burgers Model	$E_1 \times 10^8 (Pa)$	2.43	1.84	1.72
	$E_2 \times 10^9 (Pa)$	0.51	0.40	0.66
	$\eta \times 10^{11} (Pa.s)$	15.5	3.75	1.00
	n	0.39	0.40	0.51
	r	0.999	0.999	0.999
Findley Law	$E_1 \times 10^8 (Pa)$	2.5	1.94	1.89
	$E_2 \times 10^9 (Pa)$	11.3	1.95	1.97
	$\eta \times 10^9 (Pa.s)$	4.3	8.25	5.62
	n	0.27	0.24	0.18
	r	0.998	0.998	0.990

relaxation time. The Four Parameters (Burgers) model showed excellent numerical and graphical convergence, however demonstrating some limitations, that were associated with the lack of distribution of relaxation times [62].

Both the Stretched Burgers model and the Findley Law were developed

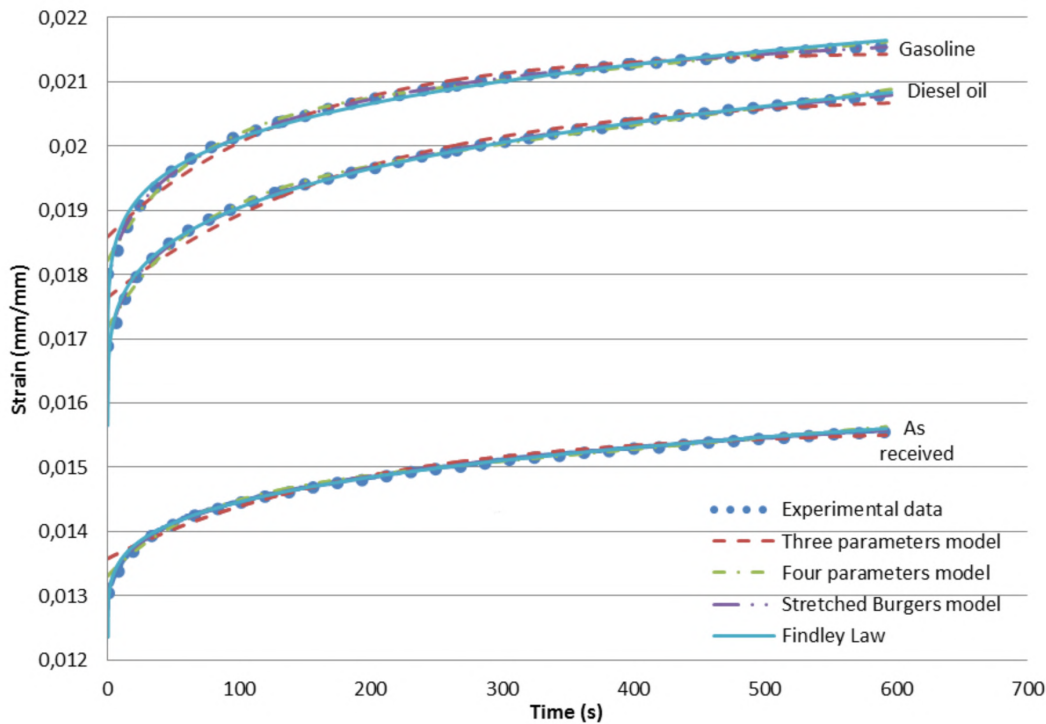


Figure 2.40: Comparison between the viscoelastic models for the HDPE specimens as received and after aging in oil derivatives [62].

to describe the nonlinear creep behavior of viscoelastic materials. However, the results presented by Pereira et al. [62] show that both models exhibited excellent convergence for the HDPE, even though HDPE exhibits linear viscoelastic behavior when subjected to low stress for short times [62]. The authors have pointed out, however, that the Findley Law should be used with care for long-time creep, as it is governed by a power law and not by an exponential function. Therefore, it shows a constantly increasing strain over time, which is not usually observed experimentally. The Stretched Burgers was the only model that did not show any restrictions on its use to describe the behavior of HDPE [62].

2.5 Characterization Techniques

When working with mineral waste, it is important to have a deeper understanding of the material's composition, morphology, size and shape distributions, as these parameters influence the mechanical and rheological properties of particulate composites [42, 52]. In addition, since the soapstone can be composed by a variety of minerals other than talc, including asbestos, and the talc as well can have impurities such as iron, titanium, manganese, amongst others, the mineralogical characterization of the waste is mandatory

in order to identify possible health hazards in the investigation of new purposes for this material [19, 77].

In the following sections, a brief theoretical background is given for each of the techniques used in this work in order to improve interpretation and discussion of the experimental findings.

2.5.1

Particle Analysis

Particle analysis instruments can be divided into two general categories, namely, stream scanning methods and field-scanning techniques. In the former the particles are examined individually and then classified into corresponding size baskets, while in the latter the whole particle assembly is measured simultaneously and the particle-size distribution is derived from the integral "field" response [78].

Different physical properties can be used to characterize the particle size, provided that there is an unique relationship between the physical property used and a one-dimensional property defining "size" [79]. However, for non-spherical particles this can only be done approximately. In order to solve this limitation, the concept of equivalent particle diameter has been introduced. There are many types of equivalent diameters, but, in general, they are defined as diameters of calibrated spheres that yield the same value of a certain physical property when analysed under the same condition as the irregularly-shaped particles [79]. For example, the volume-equivalent diameter is the diameter of a sphere having the same volume as of non-spherical particle measured by the same particle size instrument [78].

A correlation between all the different methods and equivalent diameters is yet under development, but the general understanding is that microscopy, combined with automated image analysis, is a valuable technique for particle size analysis and data verification [80]. Despite the labor intensity of the microscopy methods, they allow an accurate description of the size distribution based on appropriately chosen projected dimensions that take into account particle shape [80, 81]. However, special care is required in the sample preparation. In order to achieve the best results, the dispersion of the powder must be complete. Particles should not be agglomerated or touching one another and in some cases a pre-treatment of the samples is necessary to enhance the separation or dispersion of aggregates [80].

The graphical representation of particle size analysis data is usually reported as a histogram, a cumulative or a density distribution. A normalized cumulative distribution $Q_r(x)$ can be seen in Fig. 2.41 , where each individual

point specifies the relative amount of particles smaller than, or equal to, a certain equivalent diameter [79].

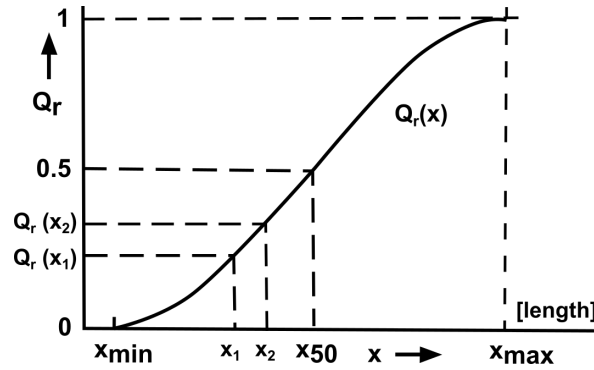


Figure 2.41: Cumulative distribution. Adapted from [79].

Figure 2.42 shows the normalized histogram of a density distribution, which can be obtained from [79]:

$$\bar{q}_r(x_1, x_2) = \frac{\Delta Q_r(x_1, x_2)}{\Delta x} = \frac{Q_r(x_2) - Q_r(x_1)}{x_2 - x_1} \quad (2-23)$$

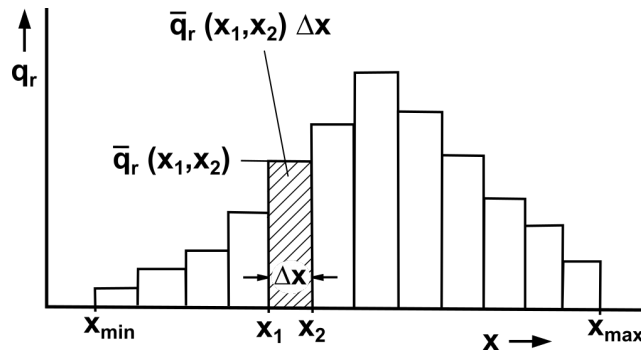


Figure 2.42: Histogram of a density distribution. Adapted from [79].

If $Q_r(x)$ is a differentiable curve, the density distribution $q_r(x)$, shown in Fig. 2.43, can be calculated as [79]:

$$q_r(x) = \frac{dQ_r(x)}{dx} \quad (2-24)$$

The density distribution can be represented in different ways with respect to the weighting of individual particles. The weighting mechanism will depend upon the physical principle being used to measure the equivalent diameter. Counting techniques, such as image analysis will provide a number distribution, in which each particle is given equal weighting irrespective of its size [82]. On the other hand, static light scattering techniques such as laser diffraction will give a volume distribution, where the relative contribution of each particle

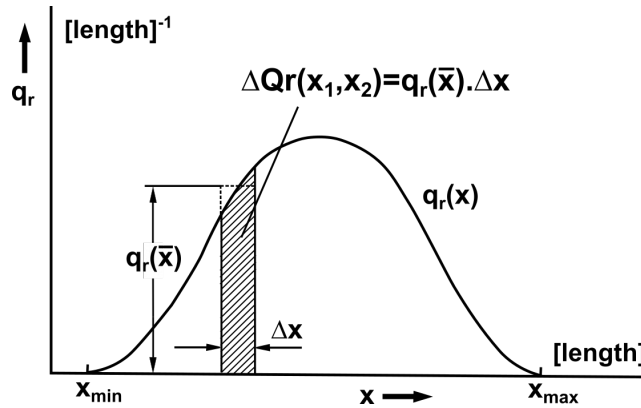


Figure 2.43: Density distribution. Adapted from [79].

is proportional to its volume [82]. The software for many equipment include the ability to convert the results from one system to another, although the conversion from volume to number distribution is not recommended, as it can lead to undefined errors [83].

Number and volume based systems are the most often used. However, other types of quantity are possible, such as length, area or, with constant particle density, mass [83, 79]. The difference between the number and volume distributions is illustrated in Fig. 2.44, which shows the distributions for a sample consisting of equal numbers of particles with diameters of 5 nm and 50 nm [82]. In the number distribution both types of particles are weighted equally, while the volume distribution emphasizes the presence of the 50 nm particles by a factor of one thousand.

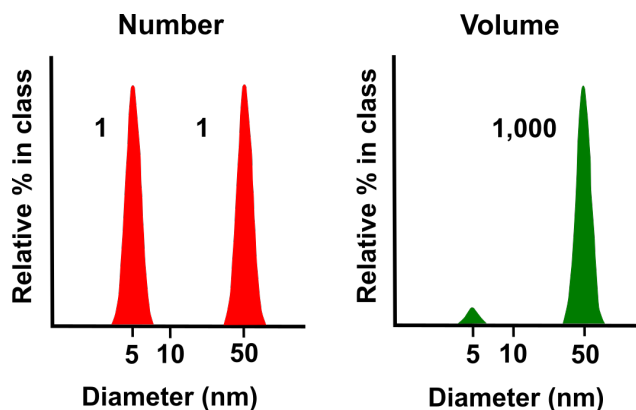


Figure 2.44: Example of number and volume particle size distributions for the same sample. Adapted from [82].

In the present work, the size and shape analyses of the soapstone waste particles were performed by automated image analysis.

2.5.1.1 Automated Image Analysis

Image analysis systems capture a two-dimensional projection of the particle profile (Fig. 2.45) and calculate various particle size and shape parameters using simple geometrical calculations [84, 82].

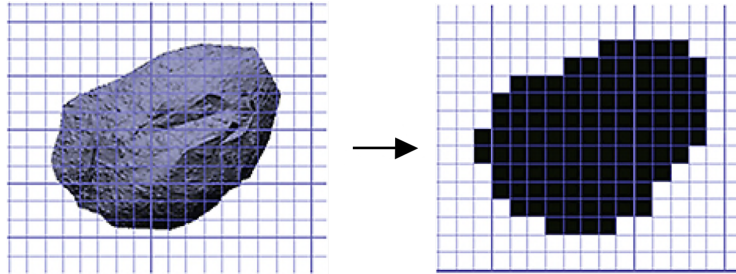


Figure 2.45: Conversion of a particle image into a 2D binary projection for size and shape analysis [82].

The particle size is determined in terms of circle equivalent (CE) diameter, which is the diameter of a circle with the same area as the projected area of the particle image. The area is determined as the visual projected area of the particle and the perimeter as the total length of the object boundary in millimeters, calculated by summing the length of the boundary pixels. The volume is measured in terms of a spherical equivalent (SE) volume, which is the volume of a sphere with the same CE Diameter as the object. The SE volume is calculated as [82]:

$$SE\ Volume = \frac{\pi \times CE\ Diameter^3}{6} \quad (2-25)$$

The overall shape of a particle can be characterized using relatively simple parameters such as Feret ratio, elongation, convexity, solidity and circularity. The first two are more sensible to the particle shape, while convexity and solidity measure the regularity of the object's outline. The HS (high sensitive) circularity parameter is sensitive to both form and outline regularity.

The ferret ratio is calculated as [82]:

$$Feret\ ratio = \frac{width}{length} \quad (2-26)$$

where the width is the minor axis and length is the major axis in the particle image, as shown in Fig.2.46. The values of the Feret ratio lie in the range 0 - 1, with 1 being the ratio of a circle.

The elongation is calculated as [82]:

$$Elongation = 1 - \frac{width}{length} \quad (2-27)$$

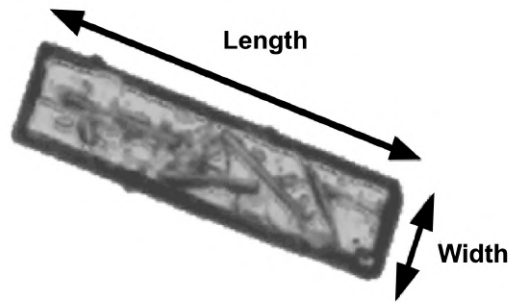


Figure 2.46: Illustration of length and width on a needle shaped particle image [82].

Elongation values also range from 0 to 1. A rod, for example, has a high elongation. The High Sensitive (HS) circularity can be calculated as follows [82]:

$$HS\ Circularity = \frac{4 \times \pi \times Area}{Perimeter^2} \quad (2-28)$$

with 1 being the HS circularity of a perfect circle, while a very narrow object has a HS circularity close to 0 [82]. In this equation, the object's projected area is divided by the square of the perimeter, thus this parameter is considered a more sensitive measure when comparing particles of similar circularity.

Convexity can be calculated by dividing the convex hull perimeter of the object by its perimeter. The convex hull can be seen as the border created by an imaginary rubber band wrapped around the object, as illustrated in Fig. 2.47, where B is the added "convexity area" of the particle surrounded by the convex hull [82].

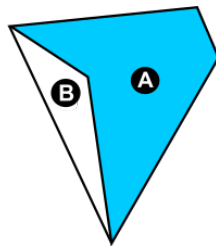


Figure 2.47: Diagram of an object (area A) and its corresponding convex hull (area B) [82].

Convexity values range from 0 (least convex) to 1 (most convex) and are calculated according to the following equation [82]:

$$Convexity = \frac{Perimeter\ of\ A + B}{Perimeter\ of\ A} \quad (2-29)$$

The solidity is the object area (A) divided by the area enclosed by the convex hull (B) [82]:

$$\text{Solidity} = \frac{A}{A + B} \quad (2-30)$$

2.5.2 X-Ray Diffraction

The X-Ray diffraction technique is highly recommended for the characterization of clay minerals, such as talc, since these materials are ordered in crystalline planes separated by distances of the same magnitude as the X-ray wave-length [77, 85]. As an X-ray beam impinges upon a crystal, it interacts with the atoms, originating the diffraction phenomenon [85]. This phenomenon occurs according to the Bragg Law (eq. 2-31) :

$$n\lambda = 2d\sin\theta \quad (2-31)$$

where n is an integer, λ is the X-ray wave-length, θ is the diffraction angle and d is the distance between planes, which is characteristic for each crystalline phase [85]. Figure 2.48 illustrates the conditions under which the Bragg Law is satisfied [37]. A set of parallel crystal lattice planes are shown, at which both incident and diffracted X-ray beams subtend θ angles. If the path differences between successive waves ($2d\sin\theta$) are equal to the wavelength of the X-rays used, or some integral multiple of it, there is constructive interference, and thus the diffracted beam is very intense and can be detected by an X-ray detector [86].

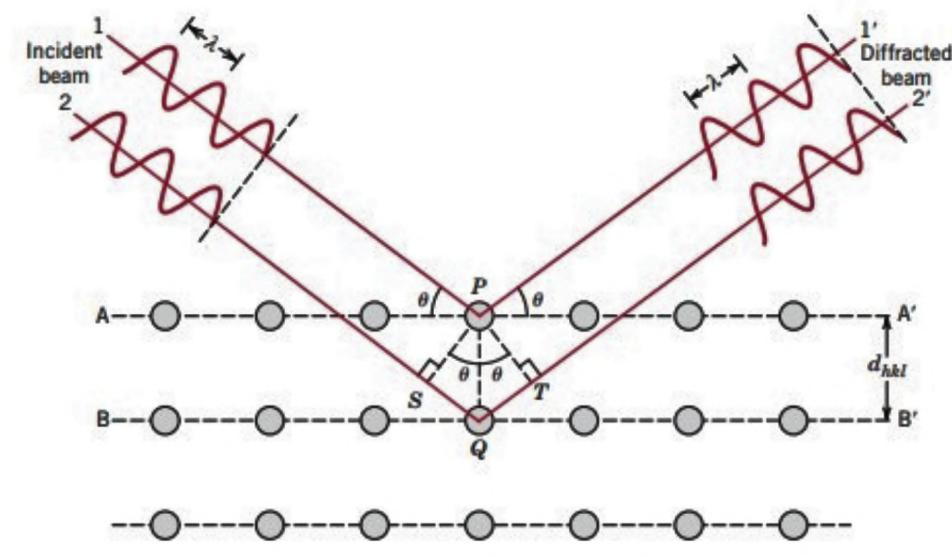


Figure 2.48: X-ray diffraction on a crystal [37].

The objective of X-ray diffraction experimental investigations is to find one or more of the following variables:

- the features of the diffraction pattern (whether sharp or broad spots, lines, or arcs, or broad halos);
- the directions (in 2θ) in which the scattered X-rays are diffracted;
- the intensity of the diffraction in the various directions.

The choice of experimental equipment depends on the type of information desired and on the type of material studied [86].

X-ray diffractometers measure the intensity distribution utilizing a counter tube or an area detector. The analysis of powders is usually done by scanning diffractometers. The majority of these equipment are based on the Bragg-Brentano technique, shown in Fig. 2.49 [86]. The optical system of a goniometer has its counter tube set to scan point by point, in a horizontal plane. Using a "line-focus" X-ray source, the Soller slits, S_1 and S_2 , the vertical divergence of the incident and diffracted beams is limited to 2° , in order to minimize the error. The X-rays are diffracted by the specimen, focused on the receiving slit and enter the counter tube [86].

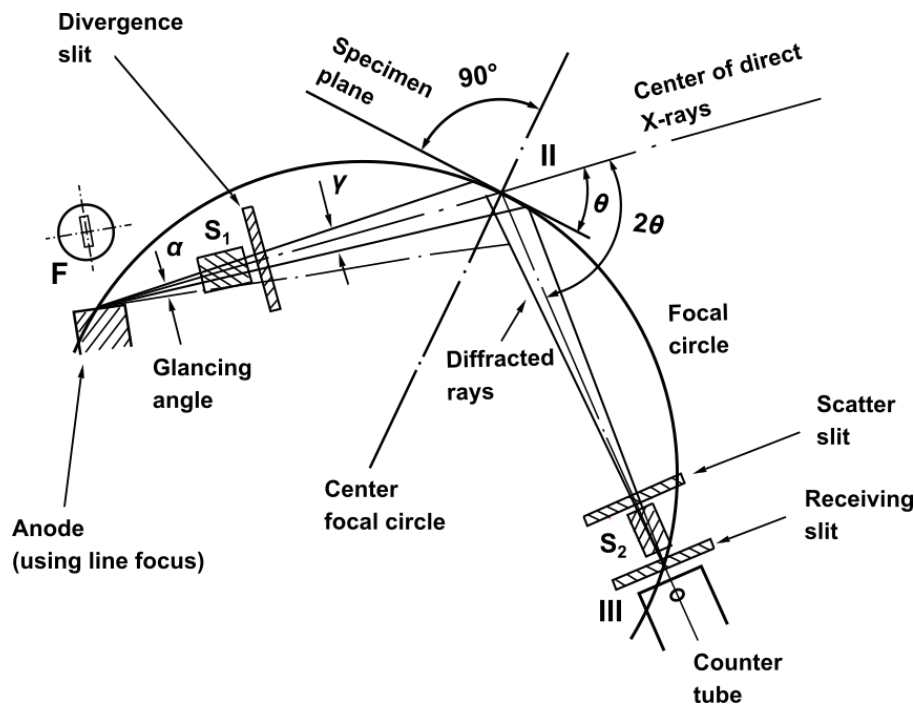


Figure 2.49: X-ray powder diffractometer (scanning type): principle of finding the diffracted intensity at Bragg angle [86].

Some advantages of the X-ray diffraction analysis are simplicity of the method, the rapidity in obtaining results and the possibility of analysing the crystalline components of a mixture [85].

In the x-ray diffractometry analysis, caution must be taken when relating peak intensity to quantity, as the morphology of the particle has a direct effect on reflectivity, and hence in the x-ray peak intensities. Many clay mineral can occur in different crystal habits and, therefore, a quantitative analysis by peak height measurement can lead to erroneous results. For quantification and a better investigation on the mineral composition it is recommended to use differential thermal analysis (DTA) combined with the X-ray diffraction [77].

2.5.2.1

Talc Crystallographic Data

Talc's structure, as reported in Fig. 2.1, consists of a brucite $[\text{Mg}(\text{OH})_2]$ layer sandwiched between two silica layers. The layers are kept together by van der Waals forces, consequently, they have the ability to slip over each other easily, which results on talc's slippery and soft nature [13, 77, 87]. It is known that talc most often crystallizes in the monoclinic system (Fig. 2.50) [87]. Values of the lattice constants and the β angle reported in the literature are listed in Tab. 2.24 [24, 88].

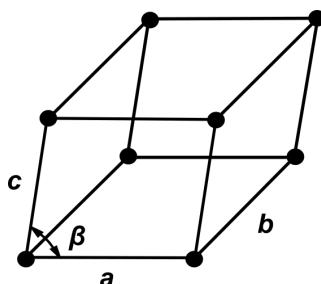


Figure 2.50: Monoclinic crystalline system. Adapted from [89].

Table 2.24: Values of the lattice constants and β angle for talc [24, 88].

	Gruner [24]	Hendricks [88]
a (Å)	5.27	5.28
b (Å)	9.12	9.12
c (Å)	18.85	18.81
β (°)	100.00	100.15

Given the crystallographic data, the VESTA software [25] plots a theoretical diffractogram for an ideal structure. Figure 2.51 shows the theoretical diffractogram obtained from the talc structure reported by Gruner [24], in order to provide a visual reference of the expected peaks. It is important to highlight that very few silicates are found in nature with the theoretical composition, so deviations in the X-ray diffraction patterns are expected [77]. As aforementioned, varying amounts of iron, titanium, manganese, between other metals can appear as oxides and/or partially substituted atoms in the lattice

for magnesium or silicon. When metals are substituted in the talc lattice they are not removable and, depending on the concentration, can be identified by X-ray diffraction [77].

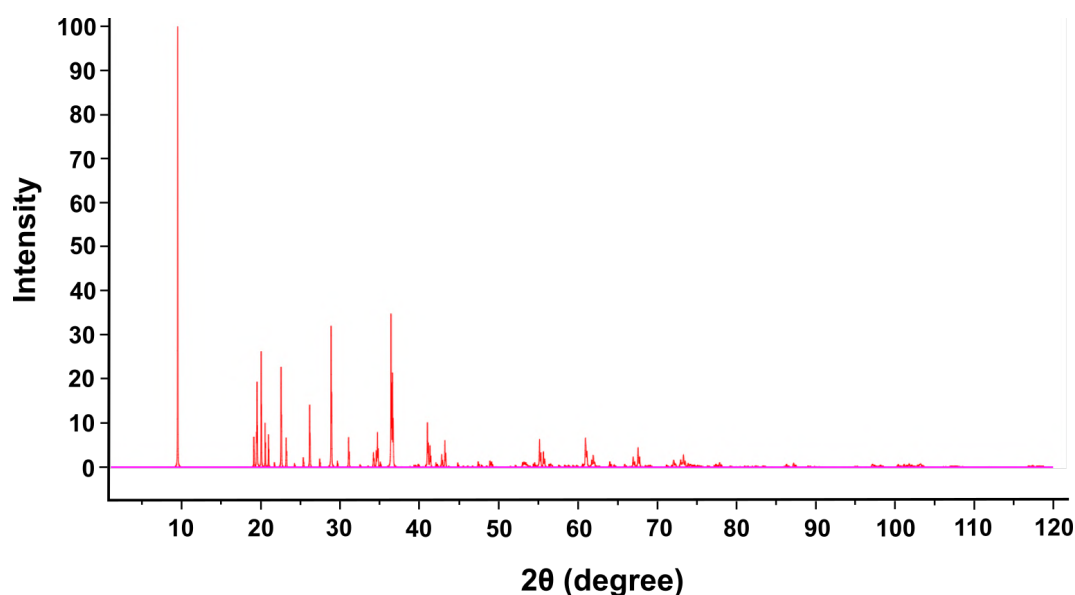


Figure 2.51: Theoretical X-ray diffractogram of talc [24, 25].

Additionally, X-ray diffraction data of natural talc mineral from Murphy, North Carolina, USA, available in the RRUFF database (R050058), can be used as reference. The data was plotted by the author using the Origin Pro software. The diffractogram and crystallographic information are summed up in Fig. 2.52 [90].

2.5.3 FTIR and Raman Spectroscopy

Infrared and Raman spectroscopy are important methods in mineral identification, as these techniques provide information of the basic molecular building blocks and their structural coordination in the mineral [91]. The vibrational spectrum of a molecule is considered to be a unique physical property characteristic of the molecule. Therefore, it can be used as a fingerprint for identification by comparison of the spectrum from an "unknown" sample with previously recorded reference spectra [92].

Additionally, spectroscopy analysis can be used for chemical characterization of polymeric composites and blends. By comparing the spectra from the virgin materials and the resulting composite it is possible to assess whether chemical interactions occurred during the compounding of the materials [93]. Therefore, in the present work, such analysis can be used to investigate whether

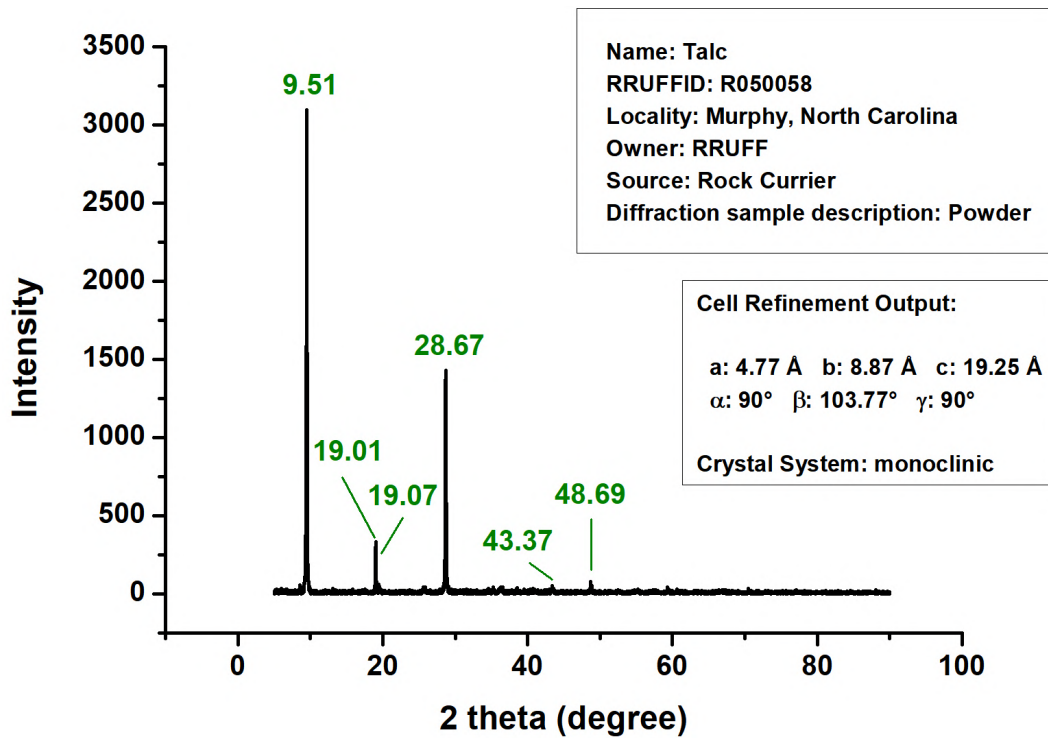


Figure 2.52: X-ray diffratogram of talc mineral from Murphy, North Carolina, USA [90].

there were any chemical reactions between the soapstone waste particles and the HDPE matrix.

The key of a practical spectroscopy approach is to understand the fundamental absorption frequencies and how to interpret them in relation to the structure and chemistry of the sample [92]. Previous to result interpretation, it is important to understand the theoretical basis of these techniques.

The infrared spectrum is formed as a consequence of the absorption of the electromagnetic radiation at frequencies that correlate to the vibration of specific sets of chemical bonds from within a molecule [92]. The majority of compounds that have covalent bonds in their structures, whether organic or inorganic, absorb frequencies in the infrared region. A portion of the electromagnetic spectrum showing the relationship of the vibrational infrared to other types of radiation is shown in Fig. 2.53 [94]. From the chemistry point of view, only the vibrational portion of the infrared spectrum is of interest, i.e., wavelengths between 2.5 μm and 25 μm . It is customary to represent the radiation in the vibrational infrared in terms of wavenumber, expressed in cm^{-1} , because this unit is directly proportional to the energy. The conversion between wavelength (λ) and wavenumber ($\bar{\nu}$) can be easily done according to Eq. (2-32) [94].

$$\bar{\nu}(cm^{-1}) = \frac{1}{\lambda(cm)} \quad (2-32)$$

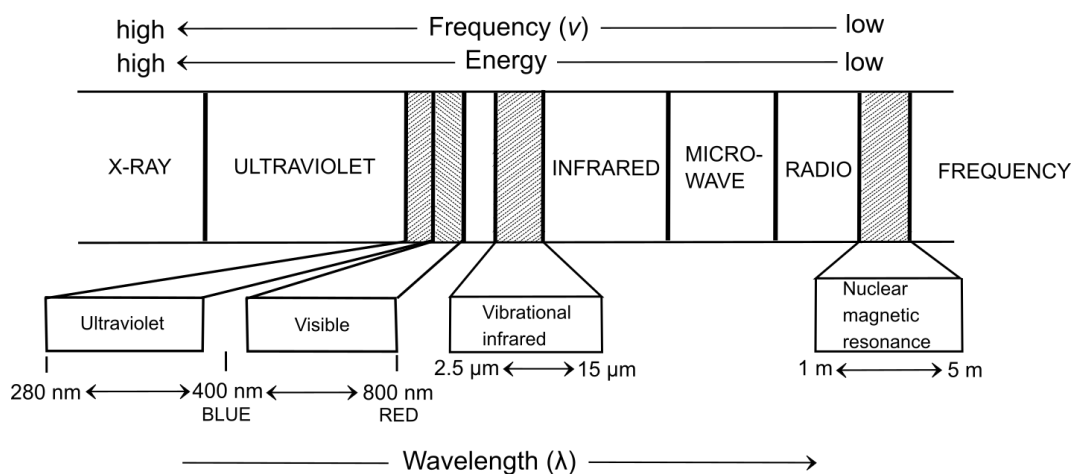


Figure 2.53: Portion of the electromagnetic spectrum [94].

The absorption of infrared radiation is a quantized process. A molecule absorbs only selected frequencies (energies) of infrared radiation, that increases the amplitude of the vibrational motions of the bonds. As a result, the molecule is excited to a higher energy state [94]. However, not all bonds in a molecule are capable of absorbing infrared energy. The fundamental requirement for absorption of infrared radiation is the existence of a net change in dipole moment during the vibration of the molecule [92]. Thus, for energy to be transferred, a bond must present an electrical dipole that changes at the same frequency as the incoming radiation. The simplest modes of vibrational motion in a molecule that are infrared active are the stretching and bending modes, shown in Fig. 2.54 [94].

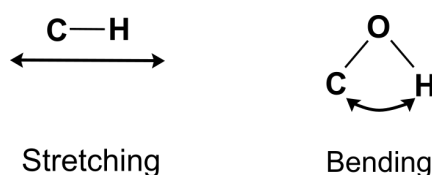


Figure 2.54: Simple modes of vibrational motion in a molecule [94].

The instrument that determines the absorption spectrum for a compound is called spectrometer. Commercially there are two types of infrared spectrometers: dispersive and Fourier Transform (FT). The latter is the most used because it provides the infrared spectrum much more rapidly than the former [94].

Raman spectroscopy is another form of vibrational spectroscopy and is complementary to infrared [91]. When electromagnetic radiation, of energy content $h\nu$, irradiates a molecule, the energy can either be transmitted, absorbed or scattered. Raman spectroscopy is based in a type of scattering phenomenon known as the Raman effect [95].

In a Raman spectrometer the sample is irradiated with monochromatic radiation, usually in the visible part of the spectrum, and the radiation scattered by the sample is analyzed in the spectrometer [95].

The Raman effect can be interpreted as an inelastic collision between the incident photon and the molecule, where the vibrational or rotational energy of the molecule is changed by an amount of ΔE_m . According to the law of conservation of energy, the energy of the scattered photon, $h\nu_s$, must be different from the energy of the incident photon, $h\nu_i$, by an amount equal to ΔE_m , as per Eq. (2-33) [95]:

$$h\nu_i - h\nu_s = \Delta E_m \quad (2-33)$$

If ΔE_m is positive, i.e., the molecule gains energy, then ν_s is smaller than ν_i , giving rise to Stokes lines in the Raman spectrum. This terminology is derived from the Stokes rule of fluorescence, which states that fluorescent radiation always occurs at lower frequencies than that of the exciting radiation. If the molecule loses energy, i.e., ΔE_m is negative, then ν_s is larger than ν_i , giving rise to anti-Stokes lines in the Raman spectrum [95].

A better visualization of the Raman scattering and a comparison to infrared absorption can be obtained by the schematics illustrated in Fig. 2.55. The lines designated as $v = 0$ and $v = 1$ represent vibrational energy levels of a molecule such as HCl. The energy is given by $\Delta E_m = h\nu_m$. The absorption of an infrared photon whose frequency is the same as the molecular frequency, ν_m , results in a direct transition between the two levels [95].

When the frequency of the incident photon is much greater than ν_m , the molecule absorbs the photon energy and is raised momentarily to some high level of energy (dashed line), which is not a stable energy level. Therefore, the molecule immediately loses energy and returns, most probably, to the ground vibrational level, emitting a scattered photon whose energy and frequency is the same as that of the incident photon. This is known as Rayleigh scattering. However, a small proportion of the molecules in the unstable high level of energy may fall, not to the ground vibrational level, but to the $v = 1$ energy level (Raman Stokes). The final possibility is that the molecule initially is in the excited state, $v = 1$, absorbs the incident photon energy, and is raised to an unstable high level of energy. When the molecule falls to the ground level,

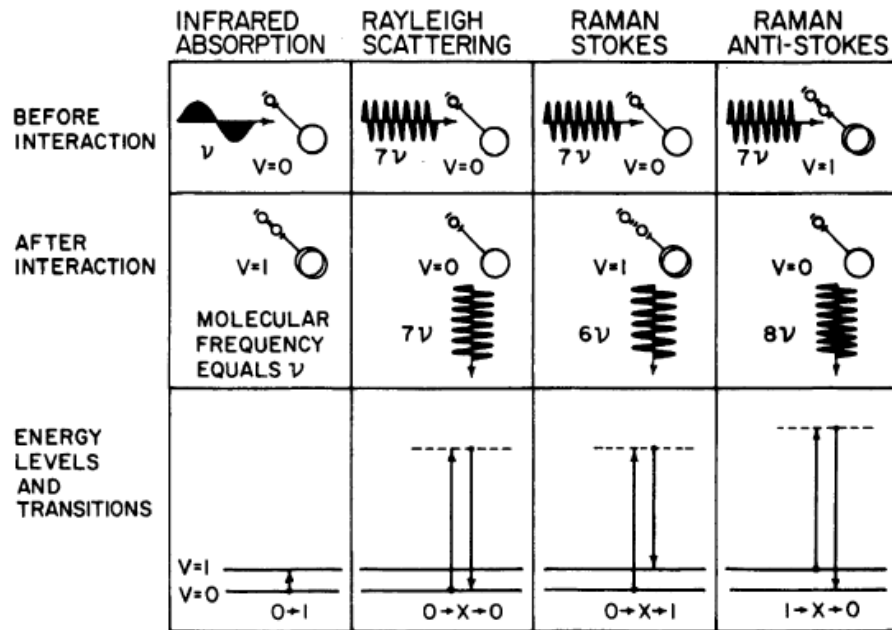


Figure 2.55: Schematic illustration of Raman and Rayleigh scattering and infrared absorption [95].

$v = 0$, it emits a photon whose energy is greater than that of the incident photon by $h\nu_m$ (anti-Stokes Raman scattering) [95].

Even though both Raman and infrared phenomena involve vibrational and rotational energy levels, they don't give the same spectrum, but complementary ones, as can be seen in the example shown in Fig. 2.56. Just as infrared-active bonds depend on the existence of a changing in electrical dipole, the Raman-active bands require a net change in bond polarizability [92]. Furthermore, the intensity of the spectral bands depends on how effectively the photon energy is transferred to the molecule and the mechanism for photon energy transfer differs in the two techniques [95].

As mentioned before, within the frame of the present work, spectroscopy analysis can be used both to characterize the mineral waste used as filler and the polymeric composites made with the waste. Thus, the main theoretical background and reference spectra for the soapstone mineral is revised in the following section. The analysis of the composites also requires knowledge of the vibrational modes of the polymeric matrix, thus HDPE bands and reference spectra are revised in Section 2.5.3.2.

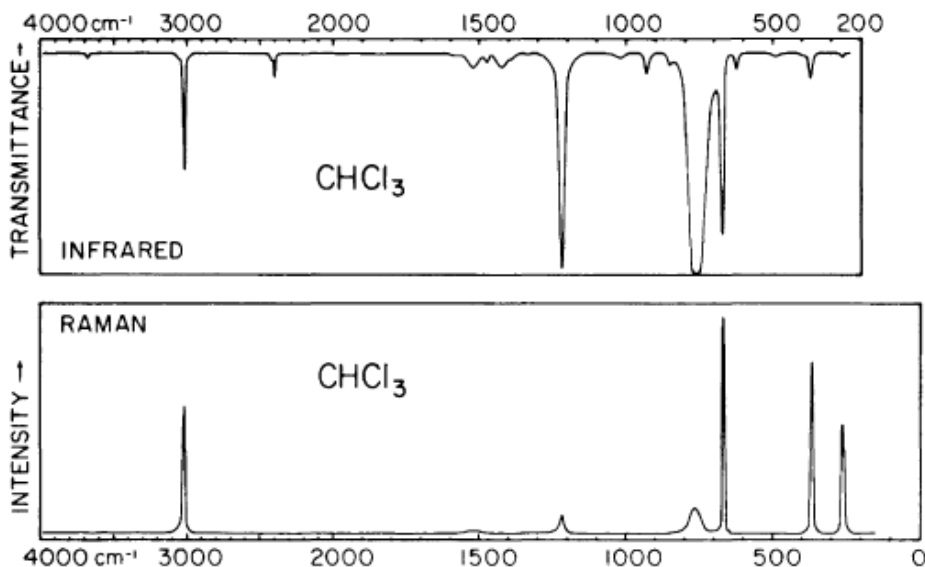


Figure 2.56: Example: complementary infrared and Raman spectra of chloroform [95].

2.5.3.1 Soapstone Infrared and Raman Bands

From the infrared point of view, talc has a relatively simple spectrum, with sharp peaks and a small number of bands. One strong peak, meaning lower transmittance, exists around $\sim 3677 \text{ cm}^{-1}$, which is due to the O-H symmetric stretch. This band is accompanied by a much weaker peak, which can be due to iron (Fe) impurities or a tilted orientation and is usually stronger in the natural specimen than in the synthetic one [22].

In their work, Rosasco et al. [21] assigned the FTIR bands with the vibration modes expected for the talc structure and compared it to observed Raman peaks (Fig. 2.57). The corresponding peak assignments are listed in Tab. 2.25. The vibrational modes were discussed in terms of an idealized unit cell and an electrostatic dipole-dipole interaction was used to compare the Raman and infrared active bands. Raman peaks were averaged from six separate crystals, with accuracy of $\pm 1.5 \text{ cm}^{-1}$ [21]. The notation \parallel and \perp implies parallel and perpendicular motion to the sheet denoted either "brucite" or silicate if so assigned, while ν_s and ν_{as} indicate symmetric and asymmetric stretching, respectively .

In the study of the spectra it is useful to identify the major structural unit and its coordination in the lattice. Talc is a layered silicate formed by cross-linking of pyroxene chains. A strong raman peak is expected at $\sim 670\text{-}680 \text{ cm}^{-1}$ that is characteristic of the silicon-bridging oxygen-silicon symmetric

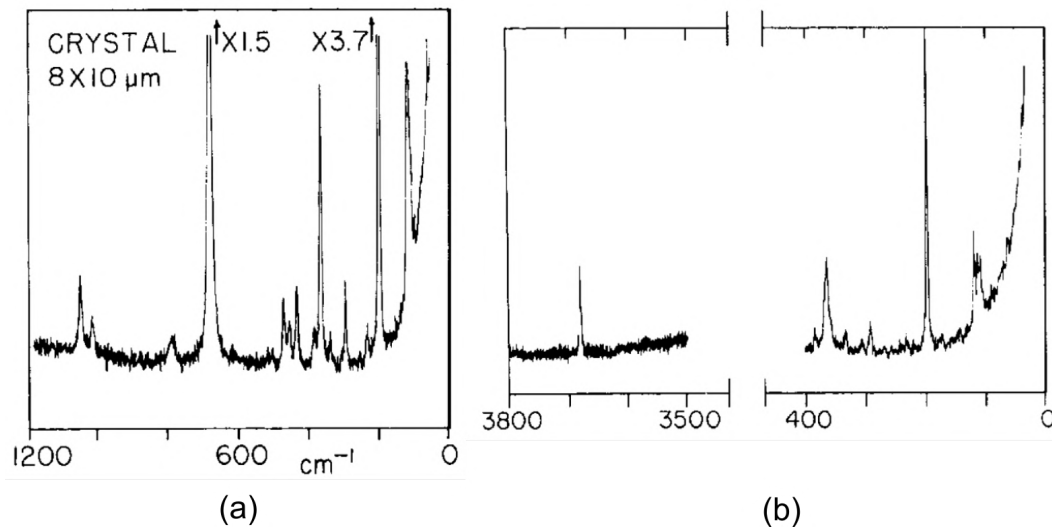


Figure 2.57: Raman spectrum of talc crystal (a) in the 1200 cm^{-1} to 0 cm^{-1} region and (b) in the low-frequency lattice and OH stretch regions with expanded scale [21].

Table 2.25: Raman and infrared peaks of talc mineral [21].

Raman peaks (cm^{-1})	Raman Intensity*	IR peaks (cm^{-1})	IR Assignments
64		169	"brucite"
109	s	177	"brucite"
113	s	231	
119	s	259	⊥ "brucite"
197	vs	311	
232	m	344	
294	m	384	
307	vw	392	
335	w	424	
366	s	440	
383	w	452	silicate
435	m	465	
456	m	499	⊥ "brucite"
471	m	535	
511	vw	670	OH libration
519	vw	687	
679	vs	779	ν_s Si-O-Si
789	m	890	
795	m	943	ν_s SiO ⁻
1018	m	1018	ν_{as} Si-O-Si
1049	m	1040	⊥ ν_{as} Si-O ⁻
3675	m	3677	OH ⁻ stretch

*vs: very strong; s: strong; m: medium; and w: weak.

stretching mode of the pyroxene chain. Non-bridging oxygen stretching mode of this silicate network is assigned in the region $900\text{--}1100\text{ cm}^{-1}$ of the spectrum [91].

In talc's structure there is a brucite layer between the silicate sheets forming a "sandwich". This brucite layer is composed of octahedrally coordinated cations (Mg ions) so metal-oxygen vibrational modes are seen in the region below 450 cm^{-1} to 200 cm^{-1} of the Raman spectrum. Certain modes below 250 cm^{-1} can be assigned to external lattice phonons, for which the

basic structural groups are vibrating or librating as a unit [91].

In another work, Baita et al. [26] did a micro-Raman characterization of medieval artifacts made of soapstone obtaining peaks of a variety of minerals such as talc, chlorite, magnesite, dolomite, calcite, aragonite and others. The Raman bands reported for talc were 195, 363, 676, 1052 and 3675 cm^{-1} [26].

Additionally, Infrared and Raman data of talc mineral from Murphy, North Carolina, USA, available in the RRUFF database (R050058) are shown in Figures 2.58 and 2.59, respectively. The main peaks were identified using the software tools.

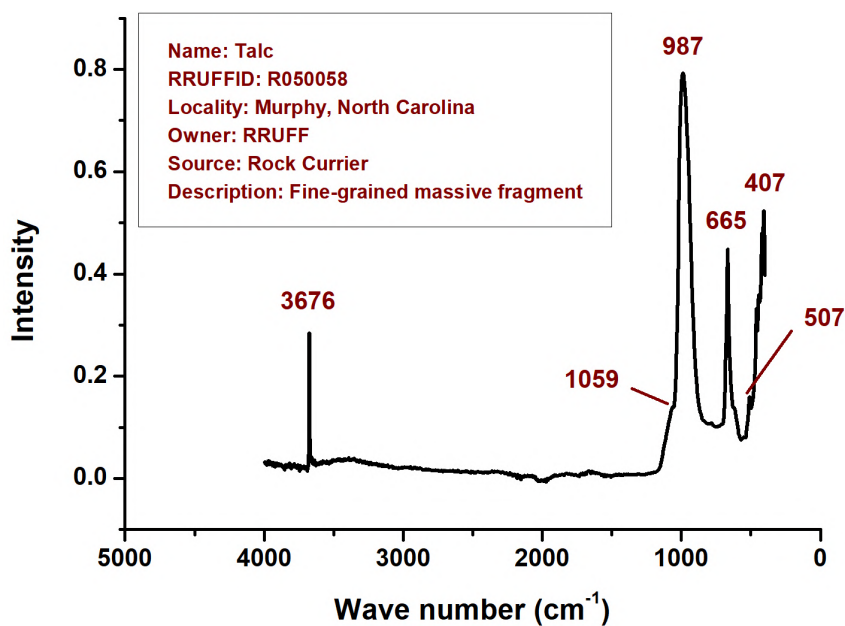


Figure 2.58: Infrared spectrum (attenuated total reflectance) of talc mineral from the RUFF database [90].

2.5.3.2

HDPE Infrared and Raman bands

In their work, Barnes et al. [96] reviewed the vibrational data, their assignments, and force field constants of polyethylene. Theoretical vibrational frequencies were calculated assuming various models of the molecular structure and force fields [96].

Like other polymers, polyethylene has a semi-crystalline structure. Reported results [97] from electron microscopy have shown that polyethylene, crystallized from dilute solution, exhibits regions of high crystallinity in which the main structural features are chain-folded lamellae and amorphous regions comprising the chain folds and interlamellar spaces. It is known that polyethylene crystallizes with two chains in the Bravais unit cell, each of which con-

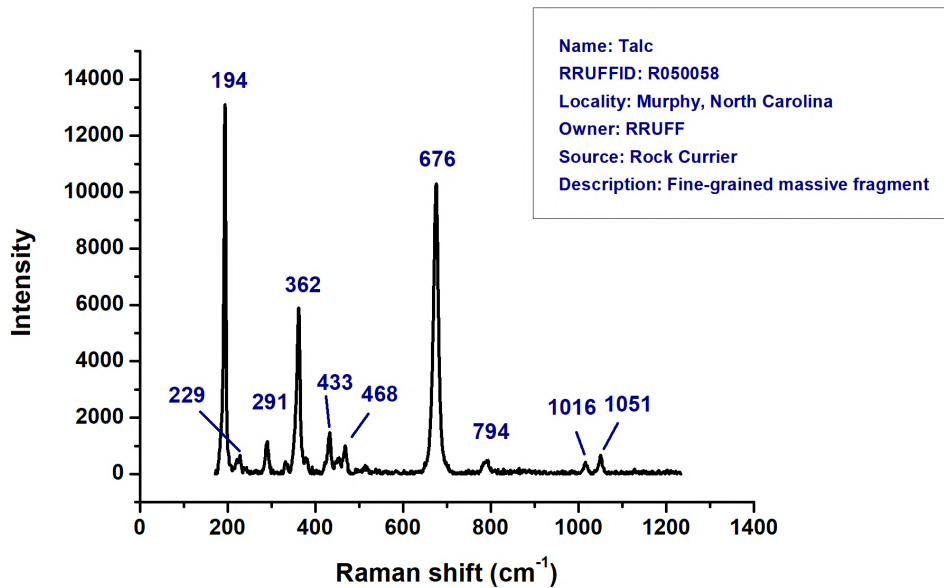


Figure 2.59: Raman spectrum (785 nm laser) of talc mineral from the RUFF database [90]. Unoriented sample.

tributes two methylene (CH_2) groups of the four comprising the orthorhombic unit cell [96]. The lattice parameters used in the calculations performed by Barnes et al. [96] are listed in Tab. 2.26. The experimental and calculated frequencies reported for the orthorhombic structure are listed in Tab. 2.27 [96].

Table 2.26: Lattice Modes of n-alkanes and polyethylene for the orthorhombic structure [96].

Type	Symmetry	Frequencies (cm^{-1})	
		Exp.	Calc.
librational	A_g	136	141
translatory	A_u	inactive	55
translatory	B_{1u}	81	86
translatory	B_{2u}	106	109
librational	B_{3g}	108	102

Furthermore, when interpreting the infrared spectrum of a polymer, it is important to consider the FTIR method used, since FTIR spectra acquired from different modes are not the same. Xu et al. [98] emphasized this point by comparing attenuated total reflection (ATR) and transmission data for eight commonly-used plastics. As can be seen in Fig. 2.60, some bands of the transmitted spectra are very intense causing opaque spectral intervals, while the ATR technique allows well-resolved and less intense bands [98]. The PE spectra from Fig. 2.60 can be used as reference in the composites analysis.

In a study of the use of waste plastics in partial asphalt binder replacement, Kakar et al. [99] performed FTIR spectroscopy to assess difference between two PE samples: pellets (PE-P) and shreds (PE-S). Figure 2.61 shows the resulting spectra. The image also includes the analysis of three binders,

Table 2.27: Experimental and calculated frequencies of polyethylene for the orthorhombic structure [96].

Symmetry	Calc. (cm ⁻¹)	Exp. (cm ⁻¹)	Assignment
<i>A_g</i>	Raman active		
	141.2	136	libration
	1137.5	1133	optical skeletal
	1175.2	1170	methylene rock
	1445.0	1442	methylene scissors
	2854.6	2848	symmetric C-H stretch
	2884.8	2883	asymmetric C-H stretch
<i>A_u</i>	Raman inactive		
	54.9	inactive	translatory
	1040.6	inactive	methylene twist
	1180.8	inactive	methylene wag
<i>B_{1g}</i>	Raman active		
	1065.8	1065	optical skeletal
	1296.8	1297	methylene twist
	1370.7	1370	methylene wag
<i>B_{1u}</i>	Infrared active		
	85.9	81	translatory
	736.5	734	methylene rock
	1477.8	1473	methylene scissors
	2851.5	2851	symmetric C-H stretch
	2921.5	2919	asymmetric C-H stretch
<i>B_{2g}</i>	Raman active		
	1069.6	1068	optical skeletal
	1293.4	1295	methylene twist
	1373.2	1370	methylene wag
<i>B_{2u}</i>	Infrared active		
	109.1	106	translatory
	720.7	721	methylene rock
	1472.3	1463	methylene scissors
	2852.9	2851	symmetric C-H stretch
	2921.7	2919	asymmetric C-H stretch
<i>B_{3g}</i>	Raman active		
	101.5	108	libration
	1137.0	1133	optical skeletal
	1176.1	1170	methylene rock
	1458.3	1442	methylene scissors
	2849.9	2848	symmetric C-H stretch
	2888.7	2883	asymmetric C-H stretch
<i>B_{3u}</i>	Infrared active		
	1042.9	1050	methylene rock
	1177.3	1175	methylene wag

which are out of the scope of this review. Regarding the polyethylene samples, some additional peaks were observed in the PE-S spectrum when compared to the PE-P, which were associated with impurities present in the PE shreds, that were confirmed by differential scanning calorimetry (DSC) analysis. Since pellets are used to produce various products such as pipes, they have to meet certain requirements of a degree of purity, hence the peaks observed in the PE-P spectrum are in accordance with the theoretical values expected for polyethylene [99]. Within the scope of the present work, the PE-P spectrum can serve as reference.

2.5.4 X-Ray Microtomography

One particularly powerful method that can be used to characterize the microstructure of a particulate composite is X-ray microtomography. This non-

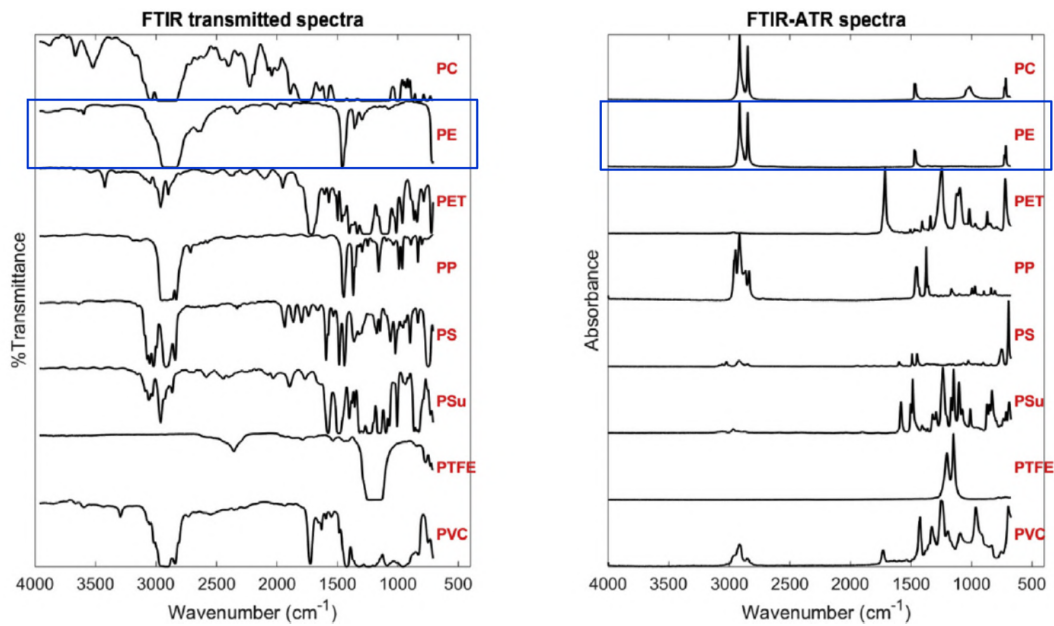


Figure 2.60: Comparison of FTIR spectra obtained in transmission and ATR modes of plastics: polycarbonate (PC), polyethylene (PE), polyethylene terephthalate (PET), polypropylene (PP), polystyrene (PS), polysulfone (PSu), Polytetrafluoroethylene (PTFE), and polyvinyl chloride (PVC) [98]

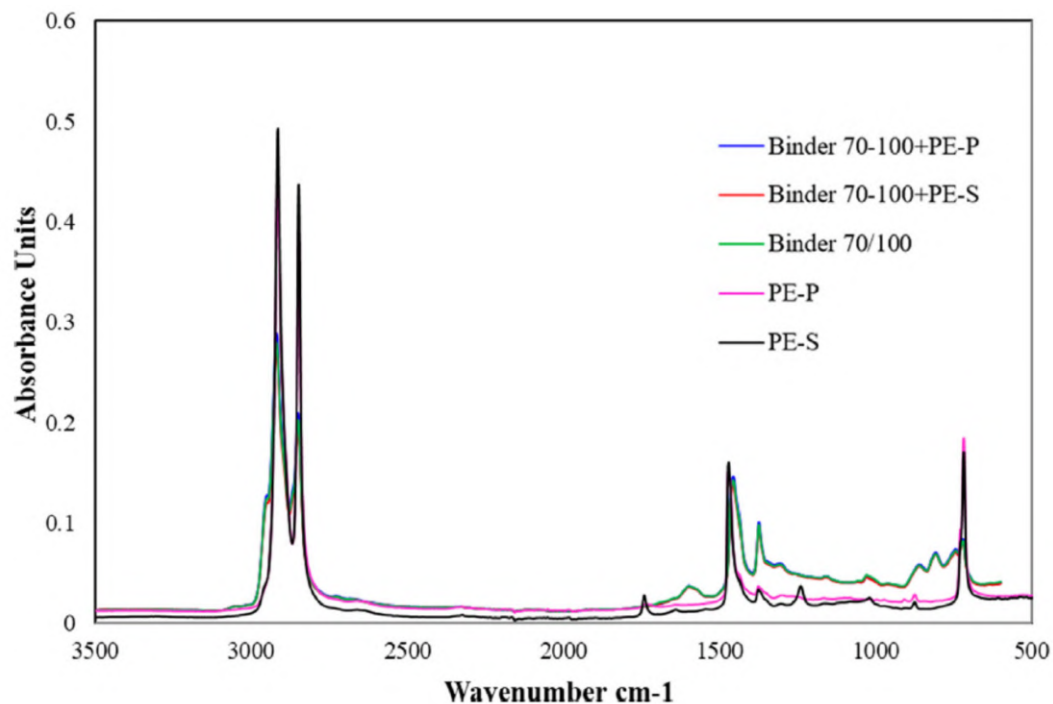


Figure 2.61: FTIR analysis of two polyethylene samples, asphalt binder and binder blends [99].

destructive technique is based on computational reconstruction of the three-dimensional (3D) structure of the sample from a number of two dimensional X-

ray images taken from different directions [18]. Figure 2.62 shows a schematic illustration of acquisition in a X-ray CT and the subsequent reconstruction process.

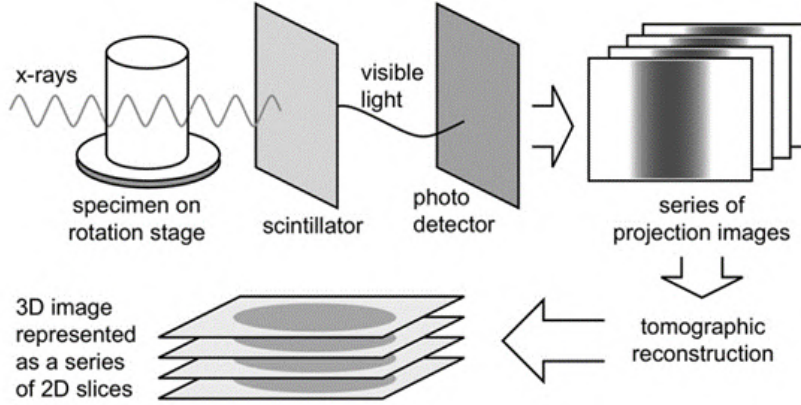


Figure 2.62: Schematic illustration of X-ray CT acquisition and reconstruction process. [100]

There are three different modes to perform tomography: absorption, phase contrast and holotomography [101]. The present work will focus on the absorption mode. Essentially, a X-ray beam is sent on a sample and the transmitted beam is recorded on a detector. According to Beer-Lambert law, the absorption of light as it passes through a material is a logarithmic function of the absorptivity of the of the material and the distance through which the light must travel (it is assumed that the parallel X-ray beam travels perpendicularly to the image plane along the y -axis) [100, 101]. The true absorptivity of the material depends on the number (density) and type of atoms along the path of the beam [100]. Therefore, the X-ray intensity I , measured at a point (x, z) , can be related to the incident X-ray intensity, $I_0(x, z)$, by [100]:

$$I(x, z) = I_0(x, z)e^{-\tau} \quad (2-34)$$

in which τ is the total X-ray absorption along the ray path. Assuming the incident and transmitted X-ray energy are measured quantities, the absorption is calculated by solving Eq. (2-34) for τ [100]:

$$\tau = \ln\left(\frac{I_0}{I}\right) \quad (2-35)$$

Experimentally, the intensities I and I_0 can be determined through the acquisition of the X-ray beam, as illustrated in Fig. 2.63.

The X-ray detector may have a baseline charge independent of the radiation striking it. Thus, to avoid interference, a baseline image of a dark field is usually taken and subtracted from the incident and transmitted images [100]. Therefore, the absorption at a particular pixel located at position (x,z) is calculated by:

$$\tau = \ln \left(\frac{I_0 - I_d}{I - I_d} \right) \quad (2-36)$$

in which I_d is the dark field intensity at that point [100].

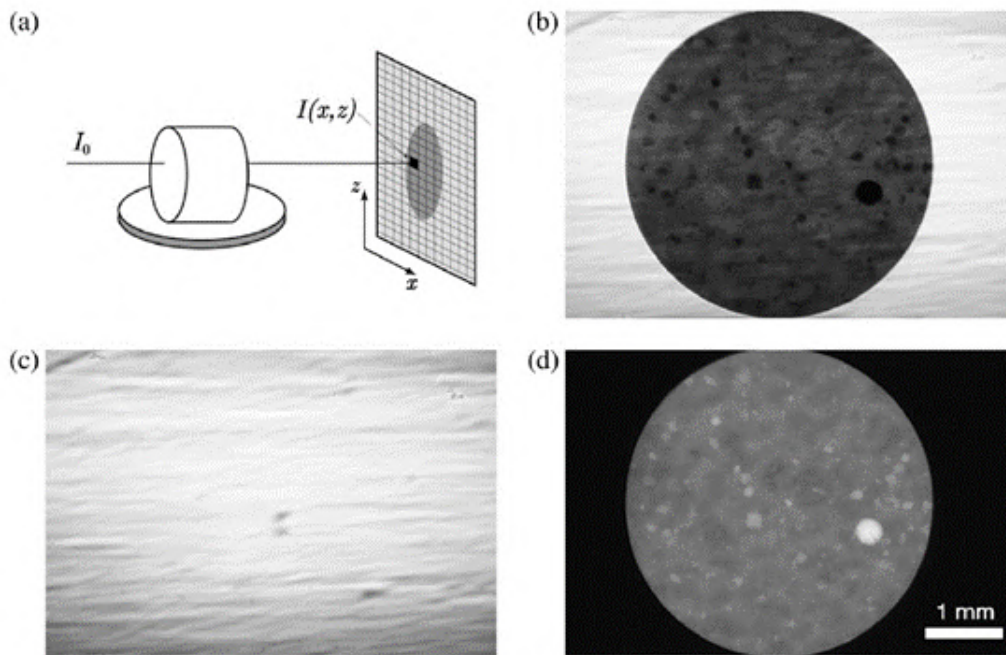


Figure 2.63: Illustration of the incident and acquired X-ray represented as a ray passing through the object. (a) the acquired intensity $I(x,z)$ is modeled as a line integral of X-ray absorption along the ray path. Total absorption along the path is calculated through measurements of both I_0 and I . (b) to (d) show images that illustrate the stage of X-ray absorption measurement. (b) is a map of $I(x,z)$, (c) is a map of I_0 and (d) is the corrected radiograph, $\tau(x,z)$, calculated using Eq. (2-34) [100]

Once an accurate series of corrected radiographs are made of a specimen, each one representing a projection of the object at a different angle, the following step is tomographic reconstruction [100]. This process requires the solution of an inverse problem and the mathematics of it are out of the scope of the present work. The tomographic reconstruction is a computationally intensive process, however, several types of reconstruction algorithms have been developed over the years and many are commercially available nowadays.

A tomographic reconstruction of projection images consists of a 3D map of X-ray absorption. Different materials features and phases often have different X-ray absorption properties. Thus, it is possible to identify the different features and have a qualitative assessment of spatial relationship. Furthermore, perhaps the most compelling aspect of tomographic data is the digital nature of the 3D images, that makes possible, through image processing techniques, to extract a wide array of quantitative measurements of the internal structure, such as phase volume fractions and spatial distributions [100].

Therefore, X-ray microtomography can be used not only to measure filler and matrix volume fractions of particulate composites, but also to assess defects such as void content and the variability of filler distribution throughout these composites. The homogeneity of filler distribution can be analysed by the parameters described in the following subsection.

2.5.4.1

Microstructural parameters

In particulate polymer matrix composites (PMMCs), particles with random size distributions and shape irregularities, are incorporated into a polymer matrix. Due to processing conditions and the randomness of the fillers, it is difficult to obtain a uniform and homogeneous distribution of the particles along the composite [18, 102]. Additionally there may be a tendency for particle clustering, where individual reinforcement particles form clusters (agglomerates) whose mechanical properties differ from those of individual particles and matrix [18].

The amount of clustering in the composite's microstructure can be expressed by dividing the total volume of particles v_p into two parts: $v_p = v_p^c + v_p^i$, where v_p^c is the volume of clustered particles and v_p^i is the volume of individual particles. Accordingly, the fraction of particles in clusters can be defined as:

$$\zeta = \frac{v_p^c}{v_p} \quad (2-37)$$

which is the volume ratio of the particles in the clusters over the total particles [18]. In addition, the amount of clustering can be described by the volume fraction of clusters as:

$$\gamma = \frac{v_p^c}{v} \quad (2-38)$$

where v is the total volume of the sample [18].

The present work proposes an approach to analyze the variability of reinforcement distribution in the composite by dividing the sample into equal

subsets and measuring the amount of filler in each subset. Considering the volume of all the particles in each subset as v_p^{sub} , two parameters can be defined: the fraction of particles in the subset, calculated as:

$$\xi_p^{sub} = \frac{v_p^{sub}}{v_p} \quad (2-39)$$

and the local volume fraction of particles, defined as:

$$\Phi_p^{sub} = \frac{n v_p^{sub}}{v} \quad (2-40)$$

where n is the number of subsets. Comparisons between the local volume fractions of particles (Φ_p^{sub}) and the total volume fraction of particles (Φ_p) can give insights to the uniformity of the filler distribution in the composite.

3 Experimental

3.1 Materials

The materials used in this work were high density polyethylene (HDPE) and soapstone waste (SW), as showed in Fig. 3.1. The soap stone waste was obtained with craftsmen in Ouro Preto, MG. The waste consists of a orange fine powder and it was used without any kind of processing. The HDPE was received as pellets with the specification IA59U3 and it was produced using the solution process by BRASKEM company. Some of the HDPE's properties provided by the manufacturer are presented in Tab. 3.1 [103].

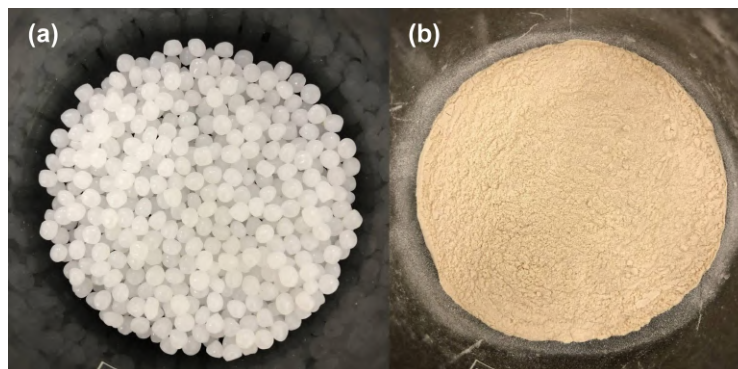


Figure 3.1: (a) HDPE pellets and (b) soapstone waste powder used in this work.

Table 3.1: Properties of the HDPE used in this work [103]

Properties	ASTM Method	Values
Melt Flow Index (g/10min)	D1238	7.3
Density (g/cm^3)	D792	0.960
Yield Strength (MPa)	D638	28
Tensile Strength (MPa)	D638	25
Shore D Hardness (-)	D2240	58
Impact Resistance (J/m)	D256	73
Softening Temperature ($^{\circ}\text{C}$)	D1525	129

3.2 Methods

The methodologies used to manufacture the composite specimens and characterize the materials are detailed in the following subsections. The characterization methods used in this work are summarized in the diagram shown in Fig. 3.2.

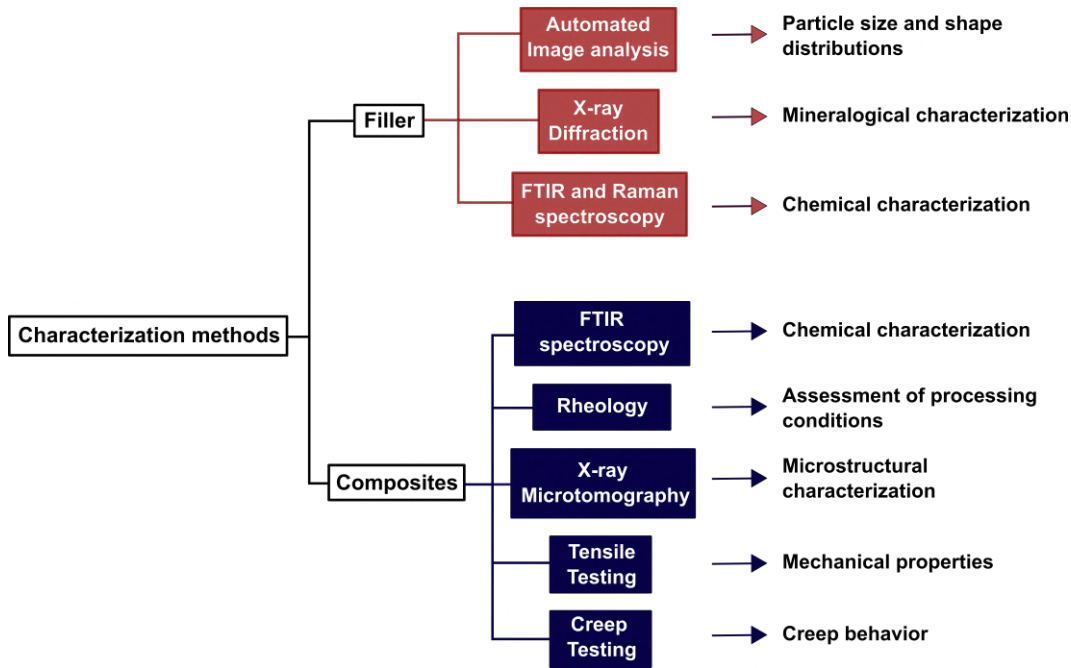


Figure 3.2: Schematics of the characterization techniques utilized in this work.

3.2.1 Filler Characterization

Image Analysis: Shape and size parameters of the soapstone particles were determined by automated image analysis with a Malvern Morphology 4 (Fig. 3.3), which has an integrated dry powder dispersion unit and can determine particle sizes in the range from 0.5 to 1300 μm .

XRD: X-ray diffraction tests were performed with a D8 Discover diffractometer from Bruker, with copper radiation operating at 40 mA and 40 kV and with Lynxeye detector. The radial scan of intensity vs. diffraction angle (2θ) was recorded in the range $5^\circ - 90^\circ$ with a step of 0.02° and 1 second by step. The software TOPAS was used to obtain the crystalline structure and to determine the crystalline peaks and the respective diffraction angles.

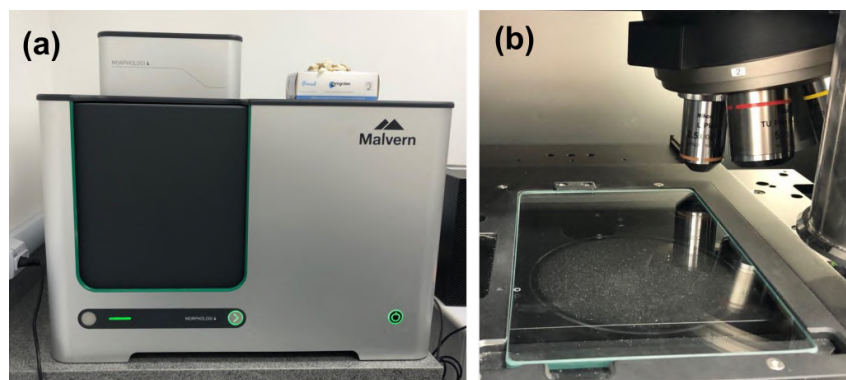


Figure 3.3: (a) Automated image analysis equipment and (b) interior of the equipment showing the dispersed powder after the analysis.

Spectroscopy: The infrared spectrum was obtained with a Perkin Elmer FT-IR Spectrometer (Spectrum Two Universal ATR), which has a standard optical system with KBr windows for data collection over a spectral range of $8,300 - 350 \text{ cm}^{-1}$ at 0.5 cm^{-1} resolution. The soapstone waste spectrum was obtained in the $4000 - 400 \text{ cm}^{-1}$ range.

A complementary Raman spectrum in the range of $1200 - 50 \text{ cm}^{-1}$ was obtained with a Horiba confocal Raman microscope (model Xplora), with 785 nm (green) Laser and 1200 gr/mm diffraction grating.

3.2.2

Preparation of Composites

The composites were produced in a mini parallel double-screw extruder (DSM Xplore 5cc), in which the inlet, homogenization and exit temperatures were set at $180 \text{ }^\circ\text{C}$, $190 \text{ }^\circ\text{C}$ and $200 \text{ }^\circ\text{C}$, respectively. The rotation used for the mixture was 160 rpm. The homogenization time was about three minutes in the extruder, under constant flow of N_2 . After the extrusion, the tensile specimens were injected using a mini injector (DSM Xplore 5,5cc), with the injection nozzle at $200 \text{ }^\circ\text{C}$ and the mold at $80 \text{ }^\circ\text{C}$. The specimen fabricated were of type V as per ASTM D638. Three different soapstone waste concentrations were used: 10%, 20% and 30% by weight, which are referred to as 90/10, 80/20 and 70/30 composites, respectively. The extruder and injector used are shown in Fig. 3.4, while the mold and some example specimens are presented in Fig. 3.5.

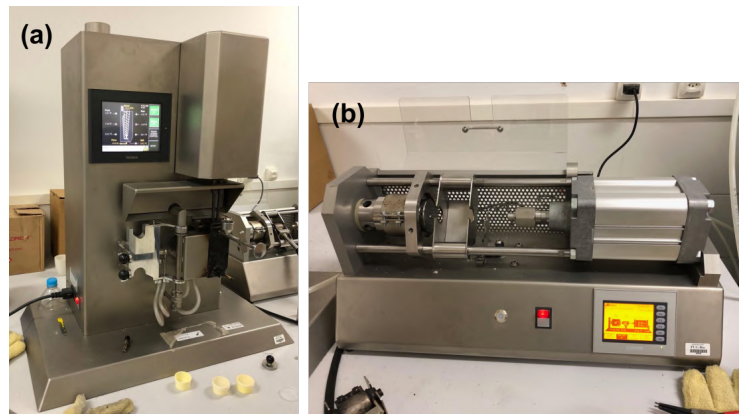


Figure 3.4: (a) Extruder and (b) injection molding machine used to produce the composite specimens.

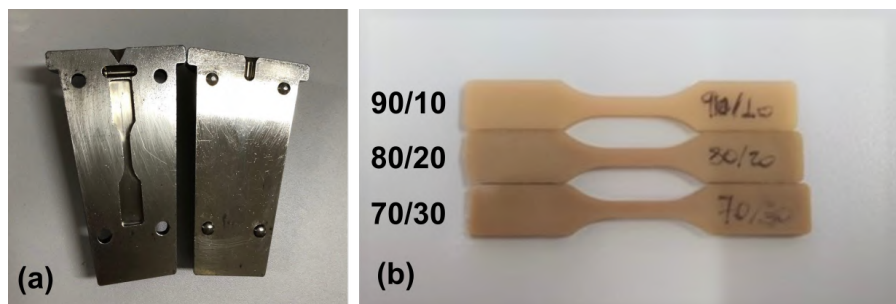


Figure 3.5: (a) Mold used in the composites production and (b) composite specimens with three compositions after production.

3.2.3 Composites Characterization

X-ray microtomography: One specimen from each composite fraction was analyzed with a Zeiss micro CT (Xradia Versa 510), with $3.5 \mu\text{m}$ pixel size, shown in Figures 3.6 and 3.7. The X-ray tube was used without filter, with acceleration voltage and power set to 80 kV and 7 W, respectively. 1601 projection images over 360° of rotation were acquired with a total of 4 s exposure time per angular position.

The digital image processing was performed with Dragonfly software. The images obtained in the micro CT were submitted to image processing and analysis following three steps: pre-processing (through the application of the Non Local Means filter, according to Buades et al. [104]); segmentation of the particles by the threshold method; and extraction of attributes. Typically, the spatial resolution refers to the minimum separation at which a feature pair can be resolved by an imaging system. Due to this fact, it is important to note that image resolution and particle distinction are limited to twice the pixel size ($2 \times 3.5 \mu\text{m}$), according to the recommendation of Zeiss [105]. The

particle's attributes include volume and feret diameters. The feret diameter can be defined as the distance between the two parallel planes restricting the object perpendicular to that direction. The minimum and maximum feret diameters are, respectively, the shortest and longest distance between any two points along the object boundary at an arbitrary angle. The mean feret diameter is defined as the mean value of the feret diameters over a sufficient number of orientations. In the Dragonfly software, measurements for the mean feret diameter are taken every 5 degrees.

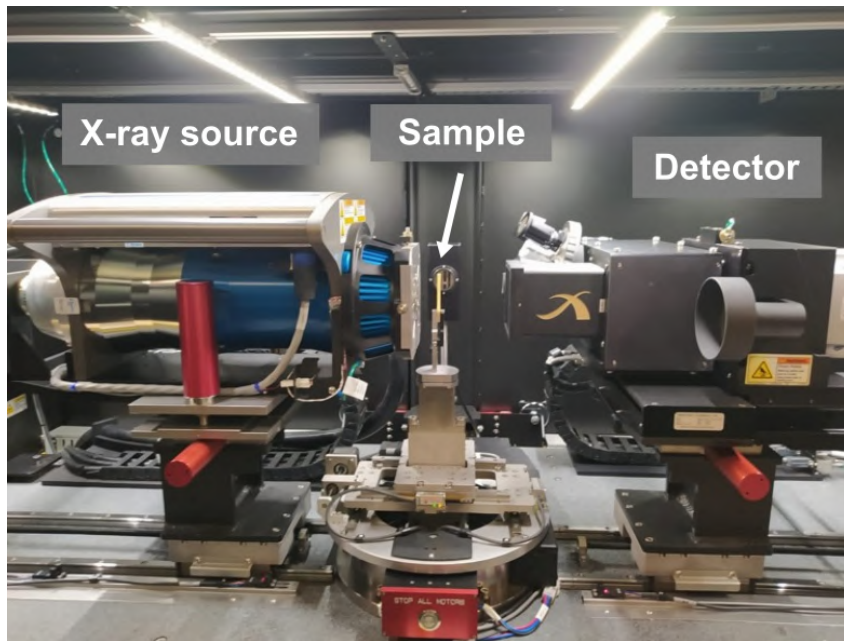


Figure 3.6: Micro CT used to characterized the composites microstructure.

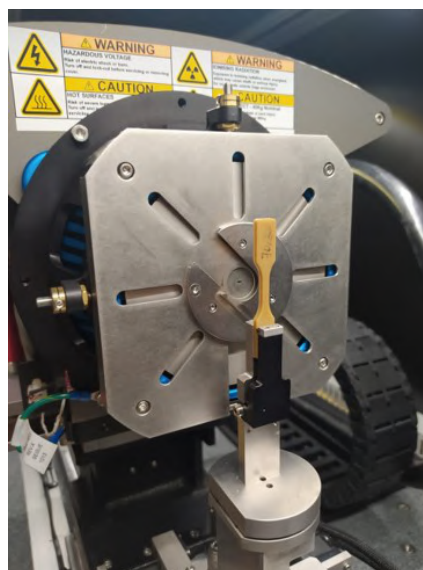


Figure 3.7: 70/30 sample positioned in the micro CT rotation stage.

Rheology: The rheology tests were made in a Discovery HR-3 rheometer from TA Instruments (Fig. 3.8.a), with 40 mm parallel plate system operating with 5 mm gap at 180 °C and with shear rate ranging from 0 to 10 s⁻¹.



Figure 3.8: Parallel plate rheometer used for rheology tests.

Mechanical Characterization: The composites mechanical behavior was evaluated by tensile and creep tests. Mechanical properties were measured using a universal testing machine, Oswaldo Filizola ASME 2 kN (Fig. 3.9.b). The test data were obtained by the Dynaview software and the properties were calculated using Excel.

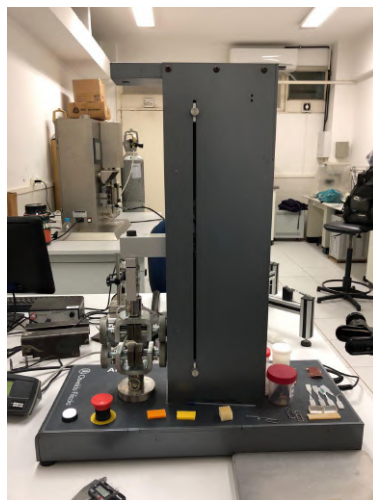


Figure 3.9: Testing machine used for tensile and creep tests.

Tensile testing: Eight specimens of each material (unfilled HDPE, 90/10, 80/20 and 70/30 composites) were tested. The tensile tests were performed at 50 mm/min and with initial distance between grips (L_0) of 25 mm. All tests were performed at room temperature (23 ± 2 °C).

Creep testing: Tensile creep tests were performed at constant load on eight specimens of each material. Load values corresponding to 50% of the yield strength were used for each class of material. The corresponding values were calculated based on the results from the tensile tests and are listed in Tab. 3.2. Further details from these calculations are shown in Chapter 4. Creep tests were performed at room temperature (23 ± 2 °C), with $68\% \pm 6\%$ humidity and acquisition rate of 30 points/min. Preliminary tests were performed with 24h to 5 days on HDPE samples in order to determine the optimal test duration. The best correlation between data and literature models was obtained with 48h, so this value was used as a maximum duration for all the creep tests performed.

Table 3.2: Creep tests setting.

Material	Load (N)
HDPE	133
90/10	152
80/20	174
70/30	179

4 Results

4.1 Filler Characterization

4.1.1 Particle Analysis

In the analysis of the soapstone waste powder, a total of 177,862 dispersed particles were measured. Descriptive statistics of the CE diameter can give a better insight to the particle size distribution. Thus, the main statistic descriptors were summed up in Fig. 4.1, which shows the cumulative number distribution and histogram of the CE diameter. The mean diameter of the particles was $10.62 \pm 8.00 \mu\text{m}$. The percentiles D_n indicate that $n\%$ (by number) of particles have a size equal to or less than that corresponding value. Even though the dispersed particles were identified in the $0.20 \mu\text{m} - 158.17 \mu\text{m}$ range, 99% of the particles had diameters less than or equal to $39.11 \mu\text{m}$, thus, values above this can be considered as outliers.

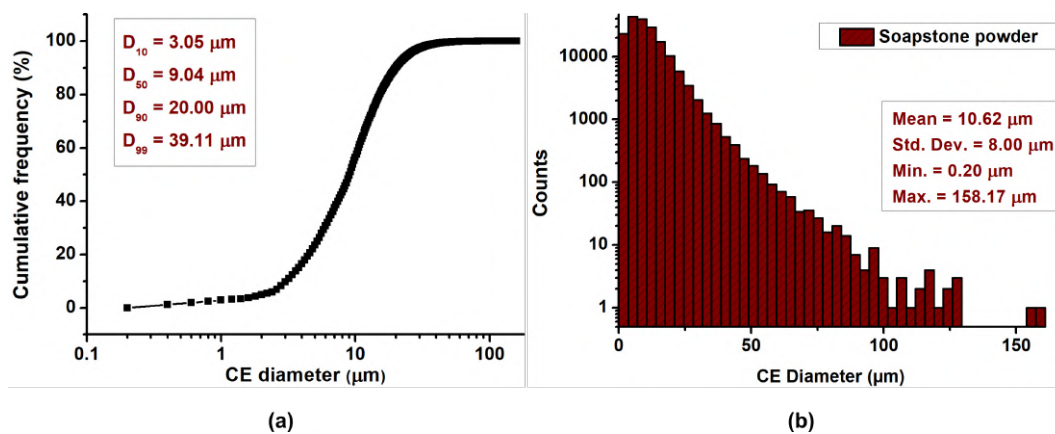


Figure 4.1: Particle size of the soapstone waste powder: (a) number distribution and (b) histogram of CE diameter.

The fraction of particles under $10 \mu\text{m}$ was of 55.21% and up to 98.70% of the particles were smaller than $37 \mu\text{m}$, which means that the waste used in this work was constituted of considerably smaller particles than the samples of soapstone waste analysed by Rodrigues [23], reported at Section 2.1.2.

As mentioned before, the volume of the particles is measured in terms of spherical equivalent (SE) volume. Figure 4.2 shows the histogram of volume of the soapstone particles. The SE volume of the dispersed particles ranged from $0.02 \mu\text{m}^3$ to $2.07 \times 10^6 \mu\text{m}^3$, but the median volume was of $386.57 \mu\text{m}^3$ and 90% of the particles had volume equal to or less than $4,189.95 \mu\text{m}^3$.

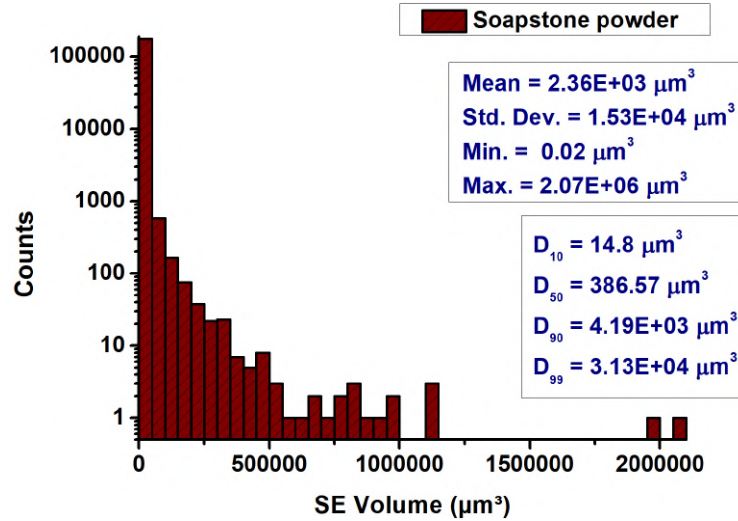


Figure 4.2: Particle size of the soapstone waste powder: histogram of SE volume.

The mean values for the shape parameters of the soapstone waste particles are listed in Tab. 4.1. The mean convexity and solidity of 0.99 and 0.96, respectively indicate regularity in the object's outline, i.e., the great majority of the particles have smooth edges. More information regarding the shape of the particles can be obtained by analysing the descriptive statistics of the HS circularity (Fig. 4.3.a) and feret ratio (Fig. 4.3.b) parameters.

Table 4.1: Shape parameters of the soapstone particles.

Parameter	Mean	Std. Deviation
Length (μm)	14.97	11.89
Width (μm)	9.14	7.24
Feret Ratio	0.63	0.16
Elongation	0.37	0.16
HS Circularity	0.77	0.15
Convexity	0.99	0.03
Solidity	0.96	0.06

The median HS circularity of 0.80 also is indicative of regularity in the object's outline. Additionally, as this parameter is also sensitive to the object's shape, it is reasonable to assume that the particles are relatively circular. However, the values obtained for the feret ratio indicate that the particles are slightly elongated. Figure 4.4 shows one of the particles analysed and the corresponding values of each size and shape parameter for visualization purposes. This example particle has a HS circularity value (0.83) close to the median of

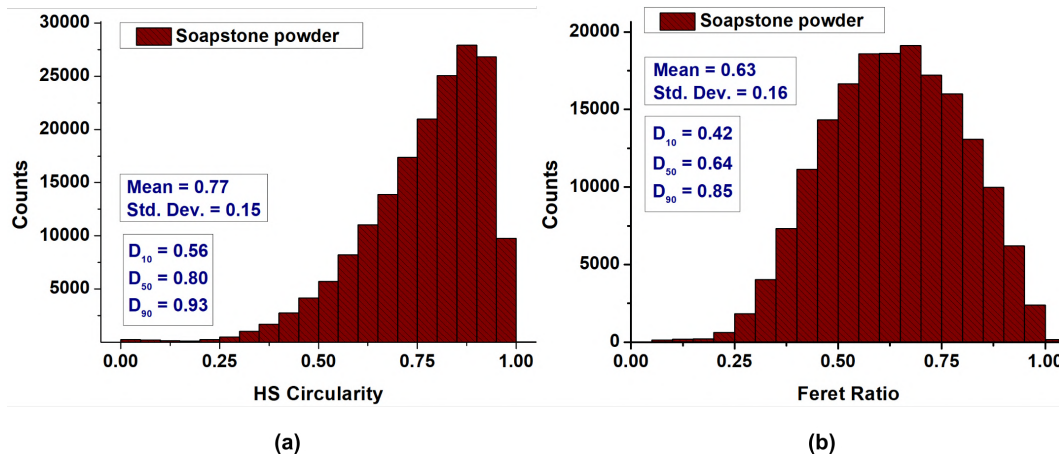


Figure 4.3: Particle shape of the soapstone waste powder: histogram of (a) HS circularity and (b) Feret ratio.

the distribution, while its feret ratio value of 0.85 is representative of the 90% percentile for the feret ratio distribution.



Figure 4.4: Example: soapstone particle and the corresponding values for the size and shape parameters measured.

4.1.2 X-ray Diffraction

Figure 4.5 shows the X-ray spectrum of the soapstone waste, in which typical talc reflections were identified. The diffractogram was imported into the TOPAS software and the analysis revealed a monoclinic crystalline structure, as expected. The talc peaks observed in the soapstone waste diffractogram are listed in Table 4.2, with their respective indices, basal distances d , and both observed and theoretical (Section 2.5.2.1) diffraction angles. The intense peaks identified at $2\theta = 9.5^\circ$ ($d = 9.34 \text{ \AA}$) and $2\theta = 28.7^\circ$ ($d = 3.12 \text{ \AA}$), as several secondary peaks, are consistent with the data from RRUFF database for natural talc (Fig. 2.52) [90]. In addition, the results are in good agreement with the values reported by other studies [24, 34, 53] for natural talc and by Rodrigues

et al. [5] for soapstone waste containing talc. However, in the latter, other minerals such as kaolinite, chlorite-serpentine, nimitite, magnesite and dolomite were also reported in the soapstone waste analysis, while in the present work talc was the only mineral identified.

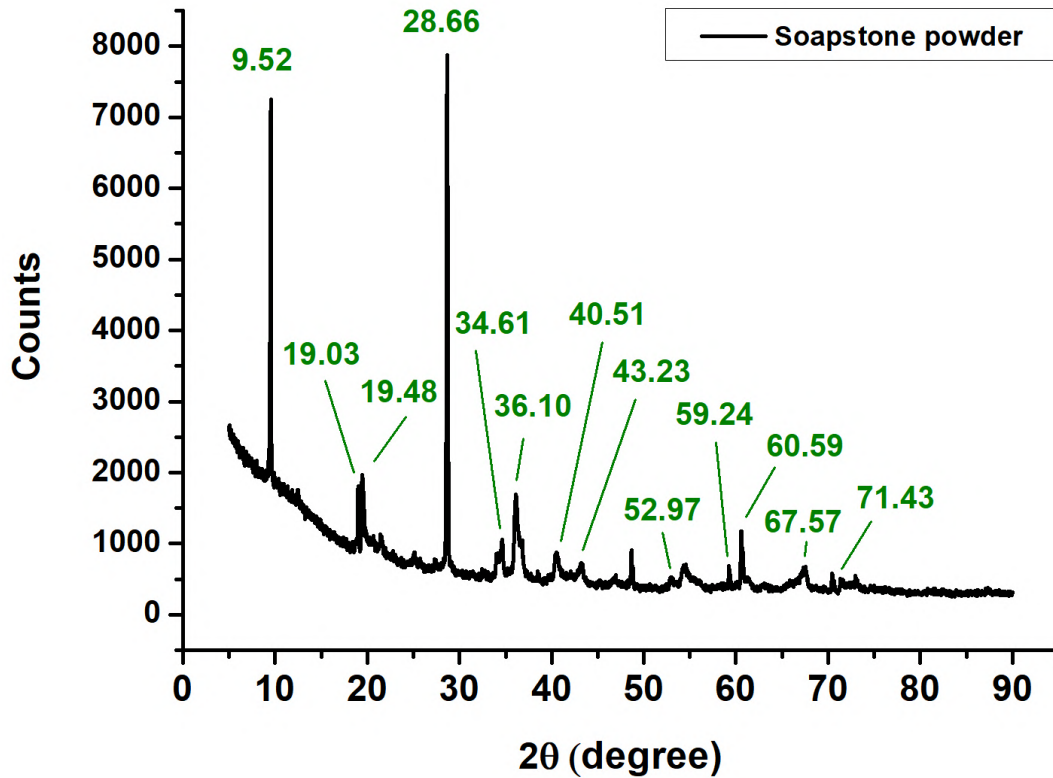


Figure 4.5: X-ray spectrum of the soapstone waste. Talc peaks identified with the corresponding diffraction angle.

Table 4.2: Talc peaks detected in the soapstone X-ray spectrum and the corresponding theoretical values.

No.	Indices	d (Å)	Theoretical* 2θ (°)	Observed 2θ (°)
1	002	9.260	9.544	9.523
2	004	4.630	19.154	19.032
3	020	4.550	19.494	19.477
4	006	3.087	28.903	28.658
5	200	2.589	34.613	34.611
6	13 $\bar{3}$	2.490	36.128	36.099
7	22 $\bar{3}$	2.226	40.489	40.506
8	13 $\bar{6}$	2.090	43.264	43.231
9	029	1.875	48.641	48.663
10	047	1.725	53.046	52.972
11	313	1.568	59.004	59.235
12	049	1.526	60.630	60.588
13	2010	1.395	67.206	67.566
14	0014	1.323	71.425	71.431

*Values from the theoretical diffratogram reported in Section 2.5.2.1.

4.1.3 Spectroscopy of the Soapstone Powder

The Fourier Transform Infrared (FTIR) spectrum of the soapstone waste powder is shown in Fig. 4.6. It can be noticed that the resulting infrared peaks are very similar to those reported in the RUFF database for natural talc mineral, shown in Fig. 2.58. Talc's O-H symmetric stretch band was detected at 3675 cm^{-1} . This band was accompanied by a weaker peak at 3660 cm^{-1} , which can be due to iron (Fe) impurities or a tilted orientation [22]. As mentioned previously, talc is a layered silicate formed by cross-linking of pyroxene chains [91]. The strong peak, meaning lower transmittance, detected at 666 cm^{-1} is characteristic of the silicon-bridging oxygen-silicon (Si-O-Si) symmetric stretching mode of these pyroxene chains. The strong peak at 983 cm^{-1} can be assigned to the nonbridging oxygen (Si-O^-) symmetric stretching mode of this silicate network.

The vibrational modes in the region under 400 cm^{-1} were detected by Raman spectroscopy and the resulting spectrum is shown in Fig. 4.7. The raman peaks are also in agreement with those reported in the RUFF database for natural talc mineral (Fig. 2.59). Table 4.3 shows a comparison of the corresponding Raman and FTIR talc peaks detected in the soapstone waste spectra and their infrared assignments, according to Rosasco et al. [21]. The spectroscopy results are in accordance with theoretical values from the literature and with the X-ray diffraction results. Talc was the only mineral identified in all spectra, which indicates that the studied soapstone waste is mainly constituted of talc and if other minerals are present, their concentration is very low.

Table 4.3: Observed FTIR and Raman bands in the soapstone spectra and their assignments.

Raman peaks (cm^{-1})	Raman intensity*	FTIR peaks (cm^{-1})	Infrared Assignments [21]
102	m		"brucite"
113	m		"brucite"
193	vs		⊥ "brucite"
291	w		
359	m	411	
433	w		silicate
452	w	459	OH transition
472	w	509	⊥ "brucite"
		666	OH libration
676	s	779	ν_s Si-O-Si
		983	ν_s SiO^-
1016	w		ν_{as} Si-O-Si
1053	w	1052	⊥ ν_{as} SiO^-
		3675	OH^- stretch

**vs*: very strong; *s*: strong; *m*: medium and *w*: weak.

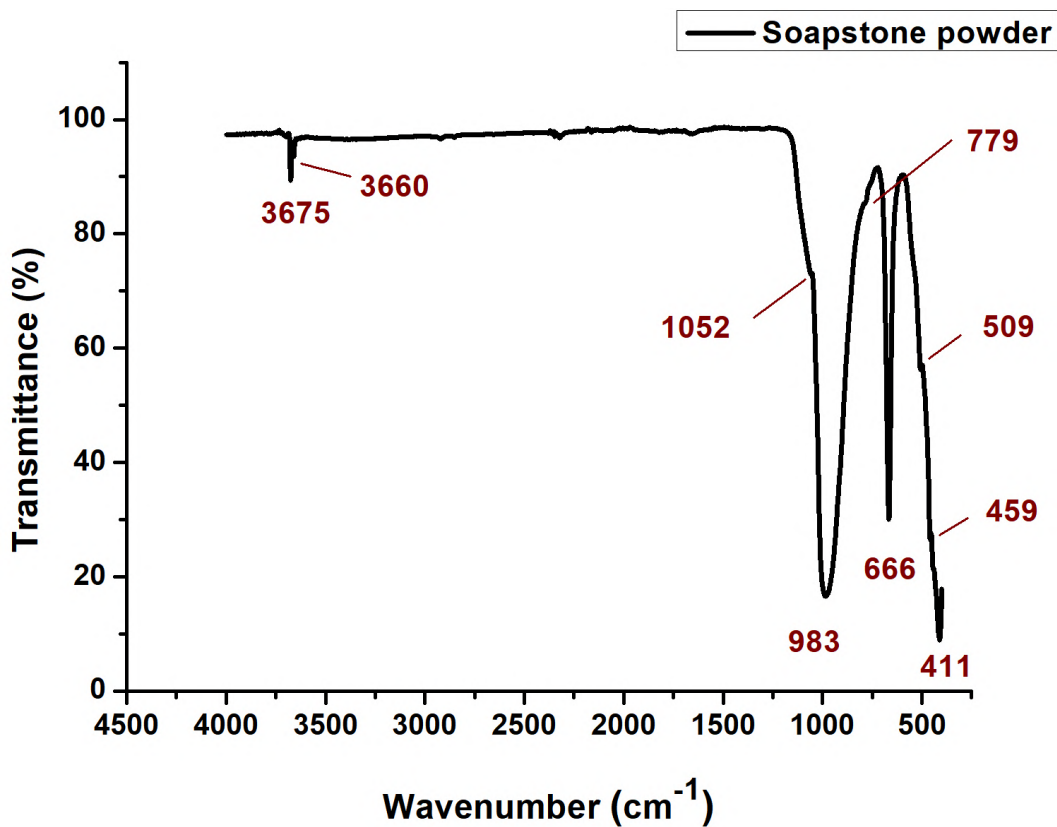


Figure 4.6: FTIR-ATR spectrum of the soapstone waste.

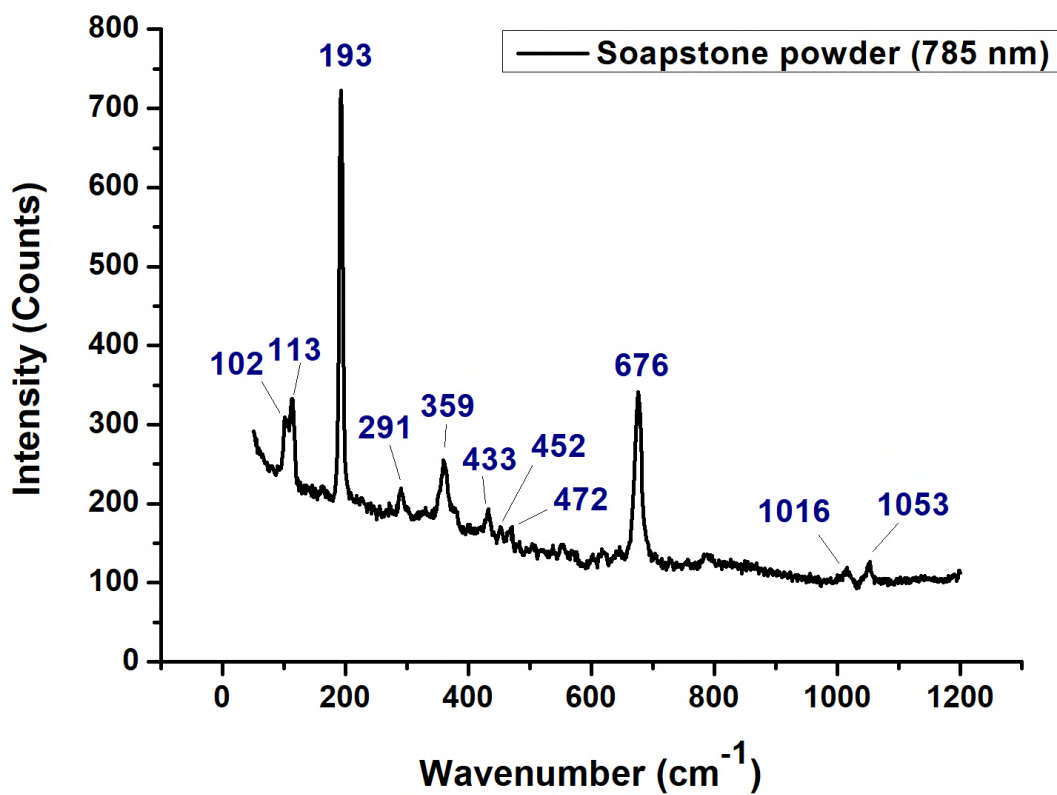


Figure 4.7: Raman spectrum of the soapstone waste.

4.2 Composites Characterization

4.2.1 Spectroscopy

FTIR spectroscopy was used to accomplish the chemical characterization of the composites. The analysis was performed on the 70/30 sample and on the virgin HDPE pellets used to manufacture the composites. The resulting HDPE spectrum is shown in Fig. 4.8, to be used as reference for the composite analysis. The resulting peaks were consistent with the polyethylene ATR spectrum reported by Xu et al. [98] (Fig. 2.60), as well as with the spectrum obtained for PE pellets by Kakar et al. [99] (Fig. 2.61). The two peaks observed at 2914 cm^{-1} and 2847 cm^{-1} are characteristic of the asymmetric and symmetric C-H stretching, respectively [96]. The remaining peaks represent the out of plane vibrational modes of the methylene group: the peaks at 1473 cm^{-1} and 1462 cm^{-1} are characteristic of methylene scissors, while the peaks at 731 cm^{-1} and 719 cm^{-1} are characteristic of methylene rock [96].

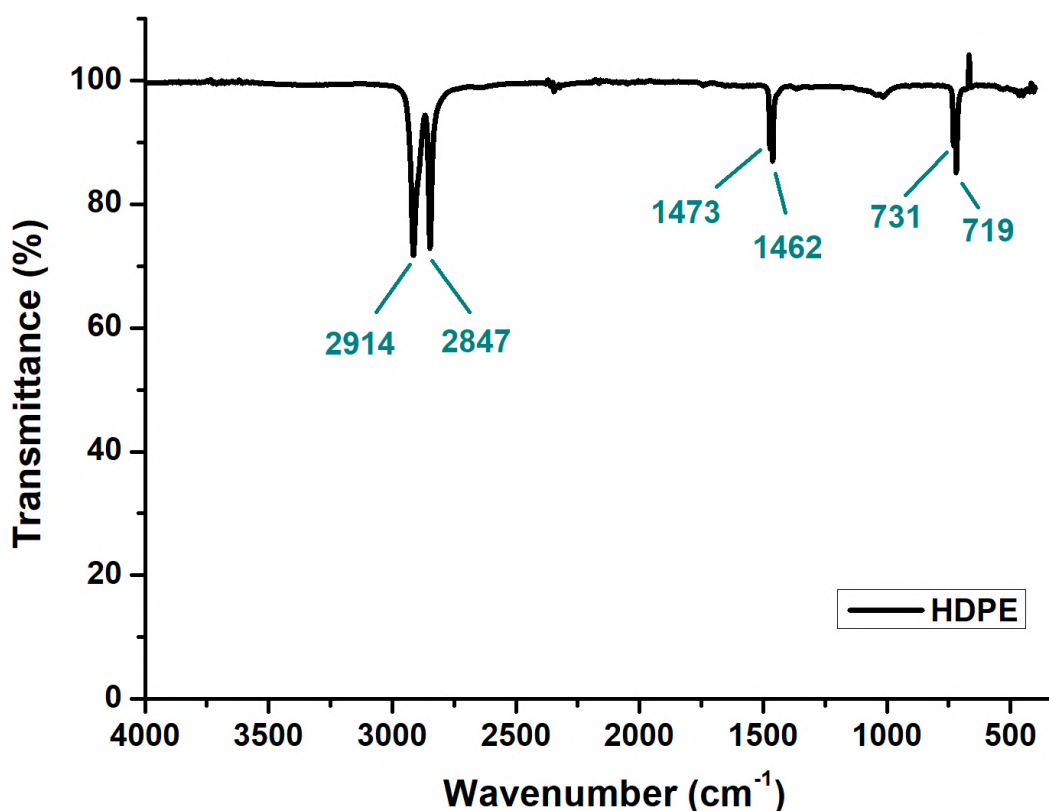


Figure 4.8: FTIR-ATR spectrum of the HDPE pellets used to manufacture the composites.

Figure 4.9 shows the FTIR spectrum of the 70/30 composite sample, in which the peaks corresponding to the HDPE matrix and soapstone filler were

identified. Figure 4.10 shows a comparison between the spectra of the neat polymer, the filler and the composite in the same scale. Most talc bands identified in the soapstone powder spectrum (Fig. 4.6) were also identified in the composite's spectrum, however the latter presented considerably less intense peaks (lower transmittance), which was attributed to the smaller amount of soapstone in the composite (30 wt%). Talc's O-H symmetric stretch band was detected at 3676 cm^{-1} . The strong peak at 983 cm^{-1} , characteristic of the Si-O symmetric stretching mode of talc's silicate network was weaker and slightly shifted in the composite's spectrum, which could be due to the overlapping of the symmetric and asymmetric Si-O stretching peaks. The two peaks were very near in the soapstone spectrum (983 cm^{-1} and 1052 cm^{-1}) and only distinguishable due to the different intensities, as indicated in Fig. 4.10.

The peaks consistent of C-H stretching modes and the methylene out of the plane vibrational modes identified in the HDPE spectrum were present in the composite spectrum, with slightly smaller intensities, which can also be attributed to the smaller amount of PE molecules in the composites, when compared to the neat pellets. The bands identified and their corresponding assignments according to Rosasco et al. [21], for the soapstone talc bands and Barnes et al. [96], for the HDPE bands were summed up in Tab. 4.4. Overall, there were no significant shifts and appearances or disappearances of peaks in the composite's spectrum. Thus, it can be concluded that no chemical reaction occurred between the HDPE and the soapstone particles.

Table 4.4: Comparison of the observed FTIR bands on the filler, matrix and composites and their assignments.

Talc bands (cm^{-1})	Composite bands (cm^{-1})	HDPE bands (cm^{-1})	Assignments
411	422		
459	449		OH transition [21]
509	500		\perp "brucite" [21]
666	671		OH libration [21]
	718	719	methylene rock [96]
	730	731	methylene rock [96]
779*	-		ν_s Si-O-Si [21]
983	1013		ν_s SiO ⁻ [21]
1052			$\perp \nu_{as}$ Si-O ⁻ [21]
	1461	1462	methylene scissors [96]
	1472	1473	methylene scissors [96]
	2846	2847	symmetric C-H stretch [96]
	2913	2914	asymmetric C-H stretch [96]
3675	3676		OH ⁻ stretch [21]

*Very weak peak.

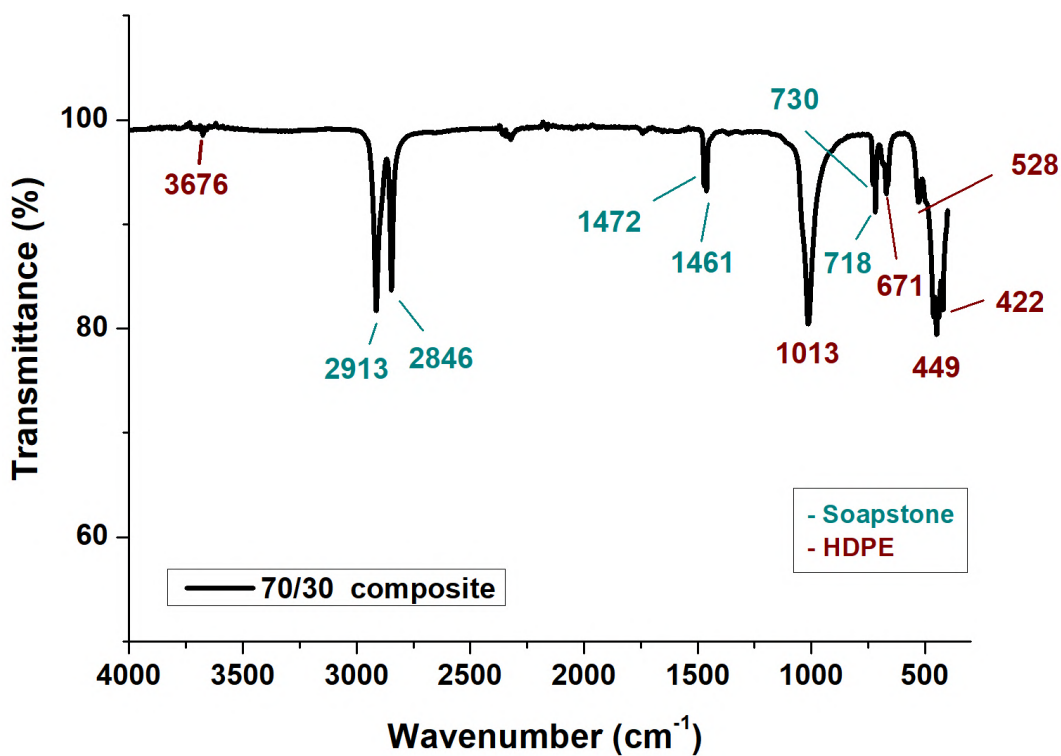


Figure 4.9: FTIR-ATR spectrum of the 70/30 composites.

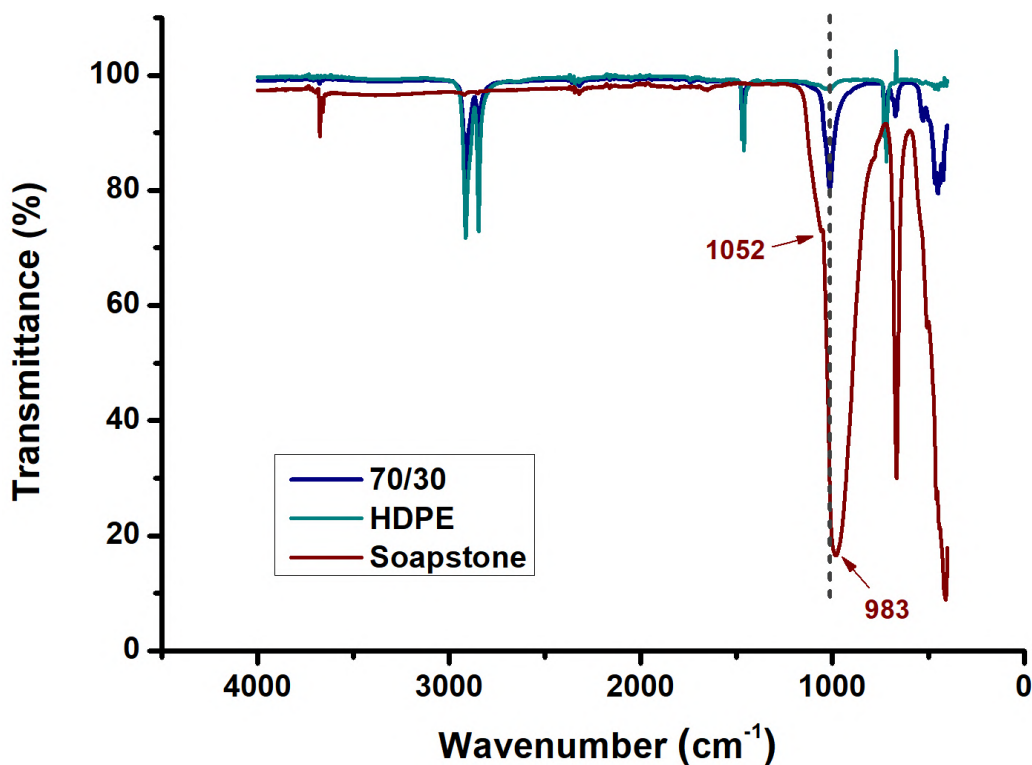


Figure 4.10: Comparison between the FTIR-ATR spectra of the 70/30 composites, the HDPE pellets and the soapstone filler.

4.2.2 Rheology

Figure 4.11 describes the dependence of the shear viscosity on the shear rate, in logarithm scale. The viscosities decreased as the shear rate increased, which implies a pseudoplastic (shear thinning) behavior of all studied systems. The shear thinning behavior is the most common amongst thermoplastics materials and it is due to the unfolding and orientation of the polymeric chains as the shear rate increases [106, 107].

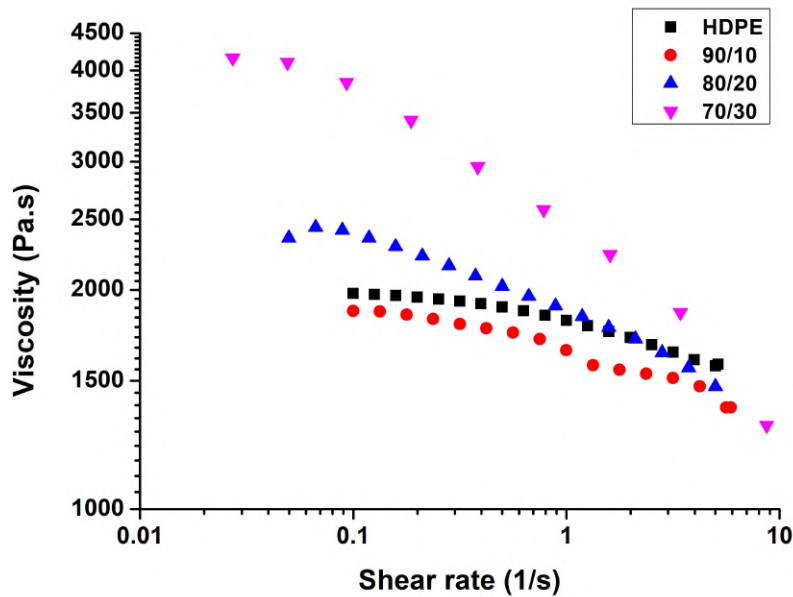


Figure 4.11: Viscosity versus shear rate curves in logarithm scale.

The filler influence on the viscosity was more evident for the 80/20 and specially for the 70/30 composites, which presented a considerable rise in viscosity in relation to the neat HDPE, as expected. In general, the addition of particulate fillers represents a strong interference in the molecular motion and, consequently, on the polymer flow [43]. As a result, it is expected an increase in viscosity with filler content [106]. The viscosity enhancement was more expressive at lower shear rates, while the viscosities of the materials were similar at higher shear rates, which is consistent with the results reported by Suh et al. [48] for HDPE-talc composites. This observation is of practical relevance since most production processes, such as extrusion and injection molding, occur at higher shear rates, ranging between a hundred and several thousand s^{-1} [106].

The 90/10 composite showed only a marginal effect on the viscosity, presenting, in fact, lower values than the neat polymer. Similar results were reported by Mehrjerdi et al. [43] from rheology tests performed at 190 °C for HDPE-talc composites with 0-15 wt% loadings, shown in Section 2.3.1.

This behavior, although unexpected, can be explained by the morphology of the soapstone waste particles. As the mineralogical characterization confirmed, the composition of the waste used in this work consists mainly of talc mineral, which is, as mentioned before, a layered mineral. The layers are kept together by van der Waals forces and are able to slip over each other easily. Therefore, by applying shear forces, the particles have the ability to slide past each other and have a lubricating function in the melt flow [43]. The lubricating effect seems to have been overcome when higher fractions of the filler were loaded into the matrix, which can be due to the distribution of particles and aggregates [52]. The probability of particle aggregation during the compounding of the samples increases when higher amounts of filler are added to the polymer. In fact, Leong et al. [11] reported that talc has a tendency of forming agglomerates at high filler loadings. These agglomerates can represent a very strong interference in the flow, especially at lower shear rates. However, as the shear rate rises, the agglomerates are broken up by the shear forces and the viscosity decreases to values similar to those of the neat polymer, as observed in Fig. 4.11.

Figure 4.12 shows the dependence of the shear stress on the shear rate for the neat and filled HDPE, in logarithm scale. Filler interference was negligible for the 90/10 and 80/20 ratios and it was a little more pronounced for the 70/30 composite, that presented higher values of shear stress at lower shear rates. It can be seen that the relationship between shear stress (σ) and shear rate ($\dot{\gamma}$) is linear for all the materials tested. This relationship can be expressed by the power law model. Considering that $\sigma = \eta\dot{\gamma}$, Eq. (2-1) becomes:

$$\sigma = K\dot{\gamma}^n \quad (4-1)$$

The power law curves seen in Figure 4.12 were calculated using the method of least squares in order to fit the experimental data. The values obtained for the coefficients are listed in Table 4.5, where r is the correlation coefficient. The value of the non-Newtonian index in all cases were less than unity, confirming quantitatively the pseudoplastic nature of the materials. In general, the pseudoplasticity of polymers is enhanced by filler addition [15]. In this case, the value of the non-Newtonian index n decreased as filler concentration increased, which implies that the addition of the soapstone particles, in fact, increased the pseudoplasticity of the polymer.

Overall, these results suggest that the addition of high concentrations of the filler (higher than 20 wt%) should require different conditions, than those of the neat polymer, for processes that occur at low shear rates, such as compression molding [107]. Based upon the tendency observed in Fig. 4.11, for

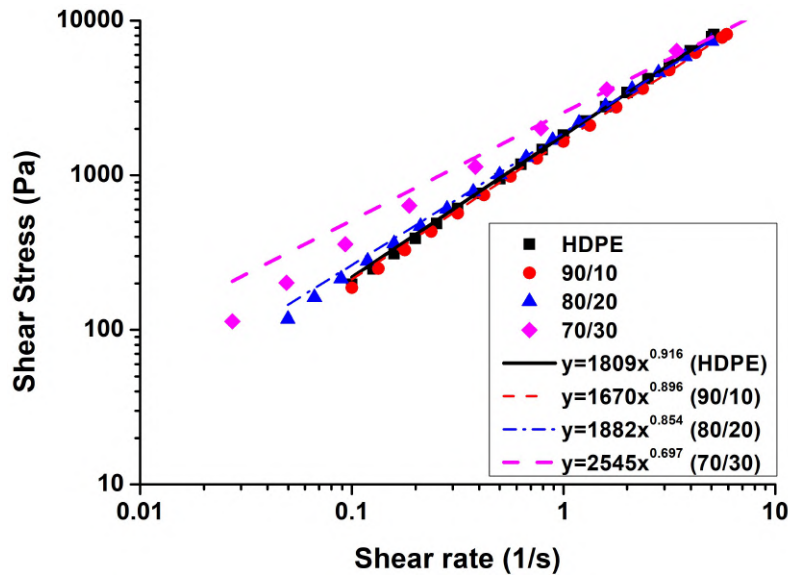


Figure 4.12: Shear stress versus shear rate curves logarithm scale.

Table 4.5: Values for the coefficients of the power law for each composite.

Material	K [Pa.s]	n	r
HDPE	1809	0.916	0.9999
90/10	1671	0.896	0.9995
80/20	1882	0.854	0.9997
70/30	2545	0.697	0.9976

processes that occur at higher shear rates, such as extrusion and injection molding, it is expected a negligible difference in viscosity and processing conditions similar to those of the neat polymer [106]. However, for the injection molding process, in the case that long and narrow ducts have to be filled, the shear rate decreases and the effect of particles on viscosity should play an important role [106]. In the case of the 70/30 composites, for instance, due to high viscosity, the complete filling of the mold cavity may be hindered, and the application of higher pressures required.

4.2.3 X-ray Microtomography

As detailed in Chapter 2, the images obtained in the micro CT were submitted to three image processing steps. The first step was pre-processing the 2D slices with the application of the Non-Local Means filter. Figure 4.13 shows 2D slices of the 70/30 sample before and after this step, where is possible to see the noise reduction promoted by the filter. Top and bottom cuts were also made in the 2D slices in order to minimize the cone defect characteristic of CT images, as shown in Fig. 4.14.

The second step consisted of segmentation of particles and voids by the threshold method, as shown in Fig. 4.15 for the 70/30 sample. The same

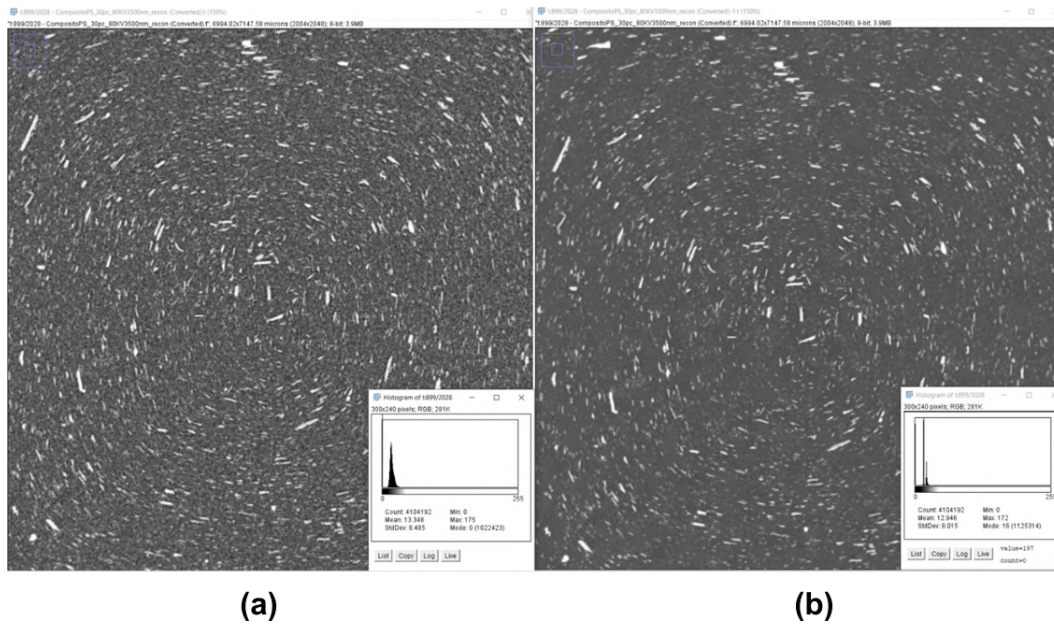


Figure 4.13: 2D slice 70/30 sample showing the pixel intensity histogram (a) before and (b) after the application of the Non-Local Means filter.

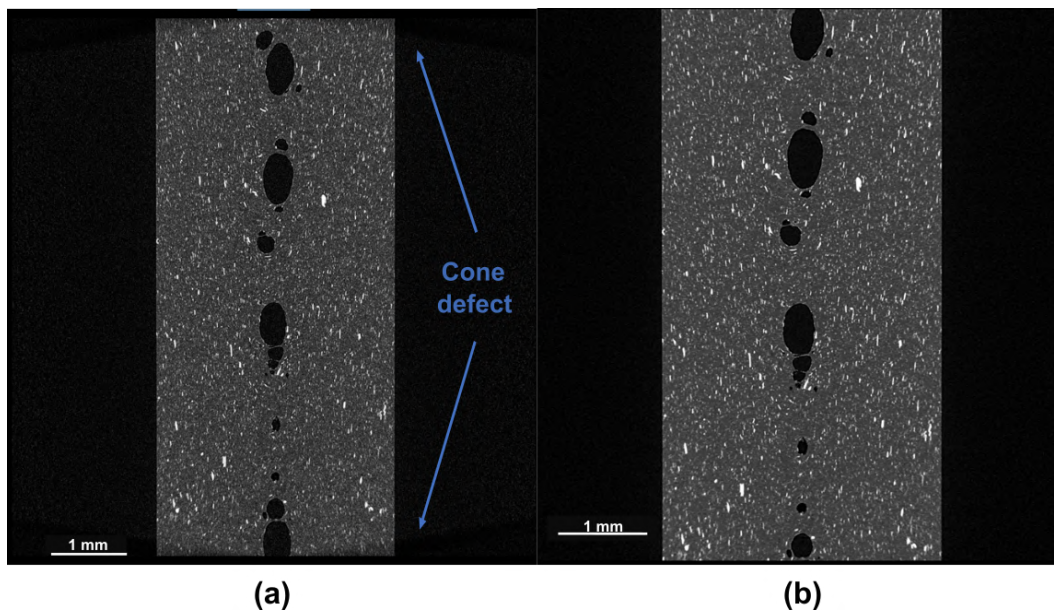


Figure 4.14: 2D slice 70/30 sample (a) before and (b) after pre-processing.

threshold was used for all three samples.

The final step of image processing consisted of the extraction of attributes. Volume and feret diameters of the soapstone powder identified in the composites were measured. Since image resolution and particle distinction are limited to twice the pixel size, in this case $2 \times 3.5 \mu\text{m}$, data assessment was required to filter items with feret diameters smaller than $7 \mu\text{m}$. The resulting mean values for the feret diameters and volume, as well as the number of particles (count) identified in the different composite samples are listed in

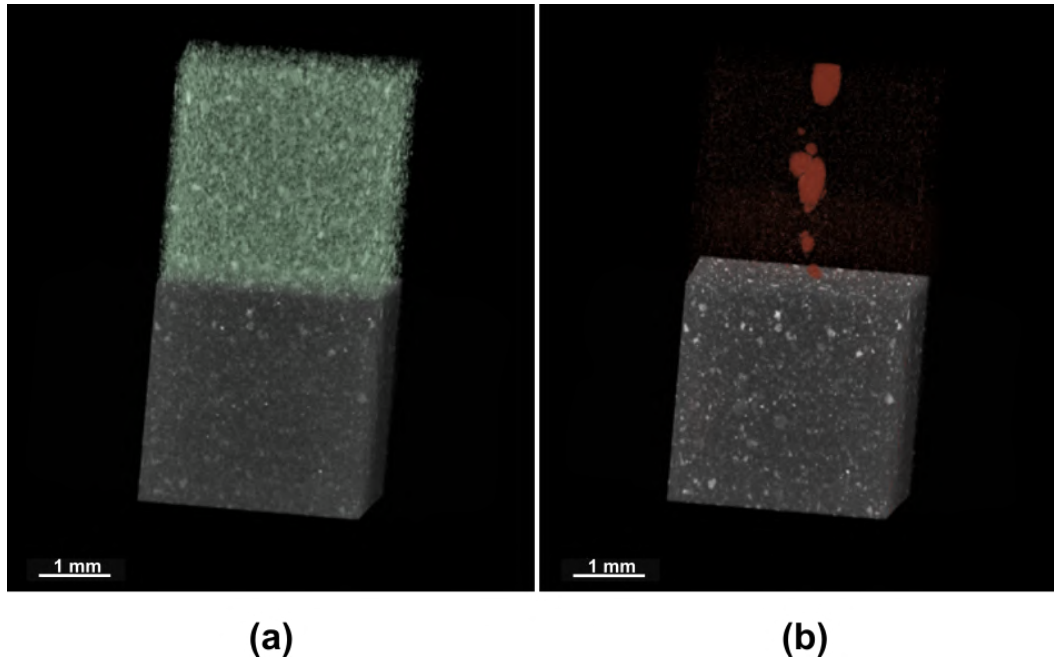


Figure 4.15: Segmentation of (a) particles (in green) and (b) voids (in red) in the 70/30 sample. The polymer matrix is shown only on the bottom half in gray color.

Tab. 4.6. The mean values of the volume and feret diameters increased with the amount of filler, which can be an indicative of particle clustering, since all composite samples were made with the same filler, under the same processing conditions.

Table 4.6: Size measurements of soapstone particles identified in different HDPE composite samples. (Uncertainties represent the standard deviation).

Sample	Count	Min Feret (μm)	Max Feret (μm)	Mean Feret (μm)	Volume (mm^3)
90/10	540696	13.13 ± 6.28	28.61 ± 17.39	22.78 ± 13.81	4.17 ± 12.31
80/20	721335	14.70 ± 8.64	31.63 ± 22.26	24.84 ± 17.39	5.75 ± 18.28
70/30	657450	15.43 ± 10.33	34.14 ± 27.25	26.94 ± 21.40	7.42 ± 26.17

Figures 4.16 to 4.18 show the 3D rendering of the three composite samples, where the particles were colored according to the corresponding size scale. These images give a qualitative assessment of the filler distribution throughout the composite samples. It is possible to see local regions where the particles appear to be agglomerated, specially in the 70/30 sample. Another aspect that was noticeable in the 3D renderings was the void content. Within the resolution of the micro CT used, no voids were identified in the 90/10 and 80/20 samples, however, as can be seen in Figure 4.19, which shows the orthographic projections of the 70/30 sample, voids were formed in the central region of this sample during processing. The formation of voids can be explained by the increase in the polymer's melt viscosity caused by the soapstone particles, reported in Section 4.2.2. As mentioned before, higher

viscosity hinders the complete filling of the mold cavity and could cause this type of defect.

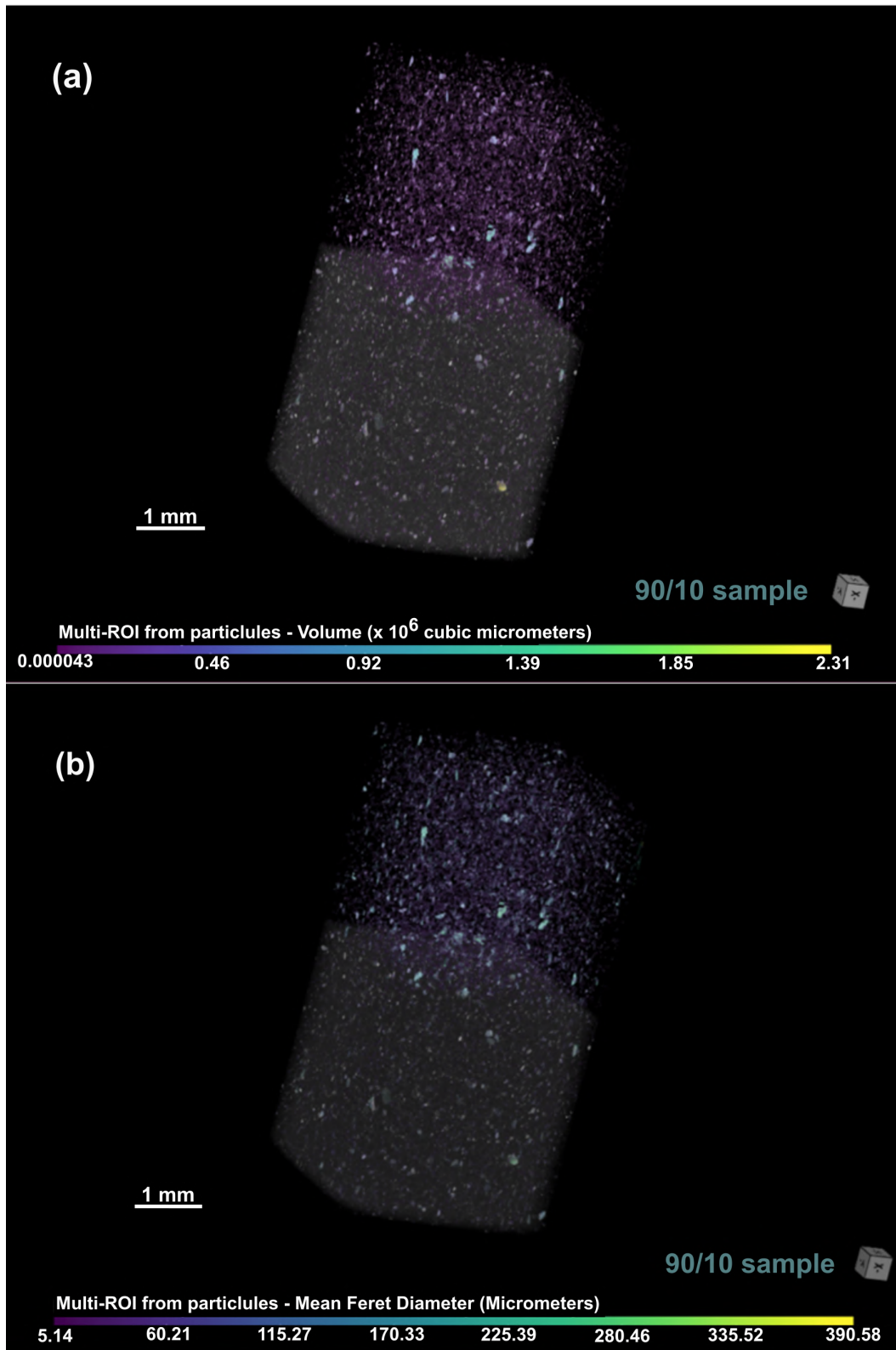


Figure 4.16: 3D rendering of 90/10 composite sample. Images show the particles colored according to (a) volume and (b) mean feret diameter scales. The polymer matrix is shown only on the bottom half in gray color.

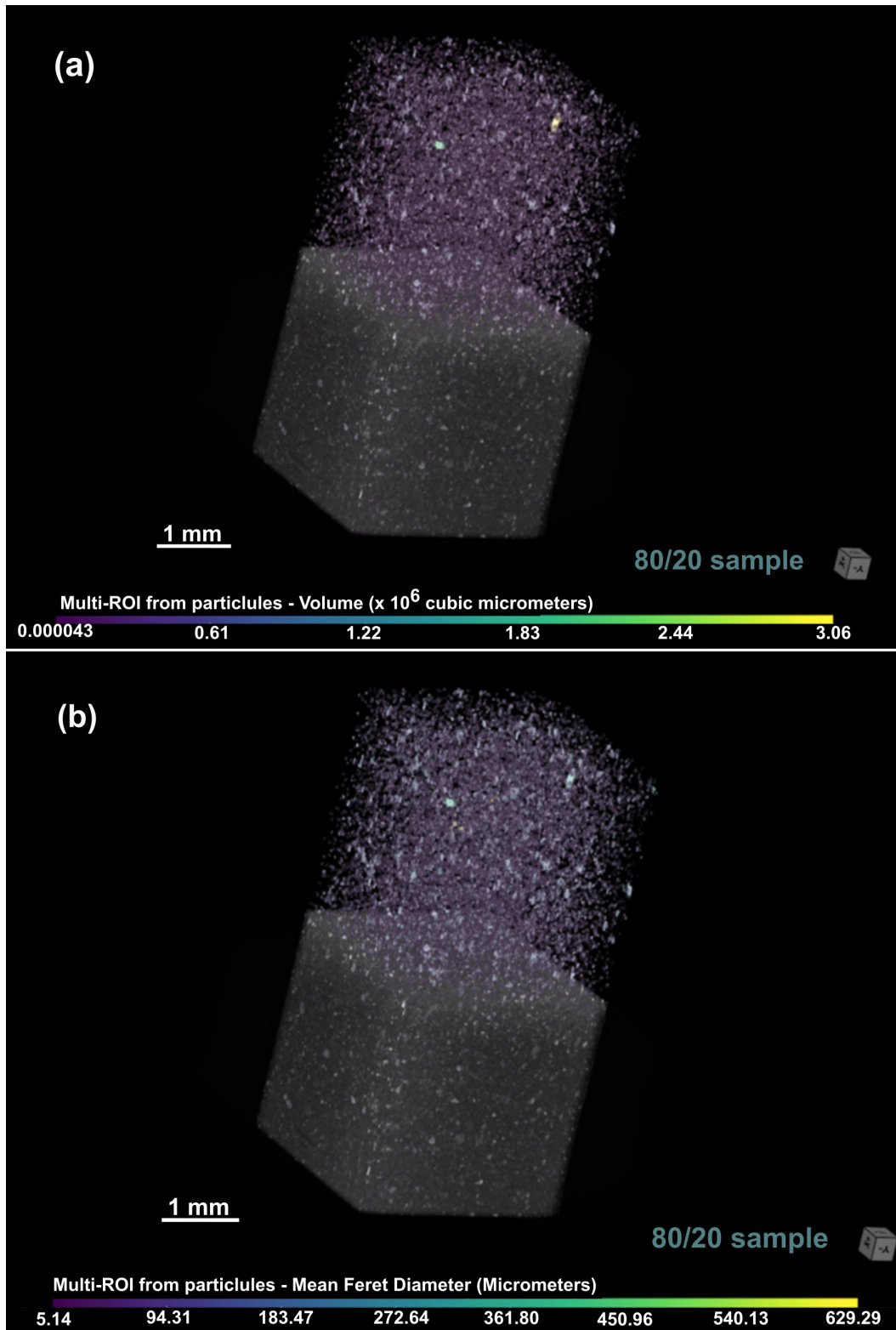


Figure 4.17: 3D rendering of 80/20 composite sample. Images show the particles colored according to (a) volume and (b) mean feret diameter scales. The polymer matrix is shown only on the bottom half in gray color.

The method used in this work does not have enough resolution to identify different particles within a cluster, however an approximation can

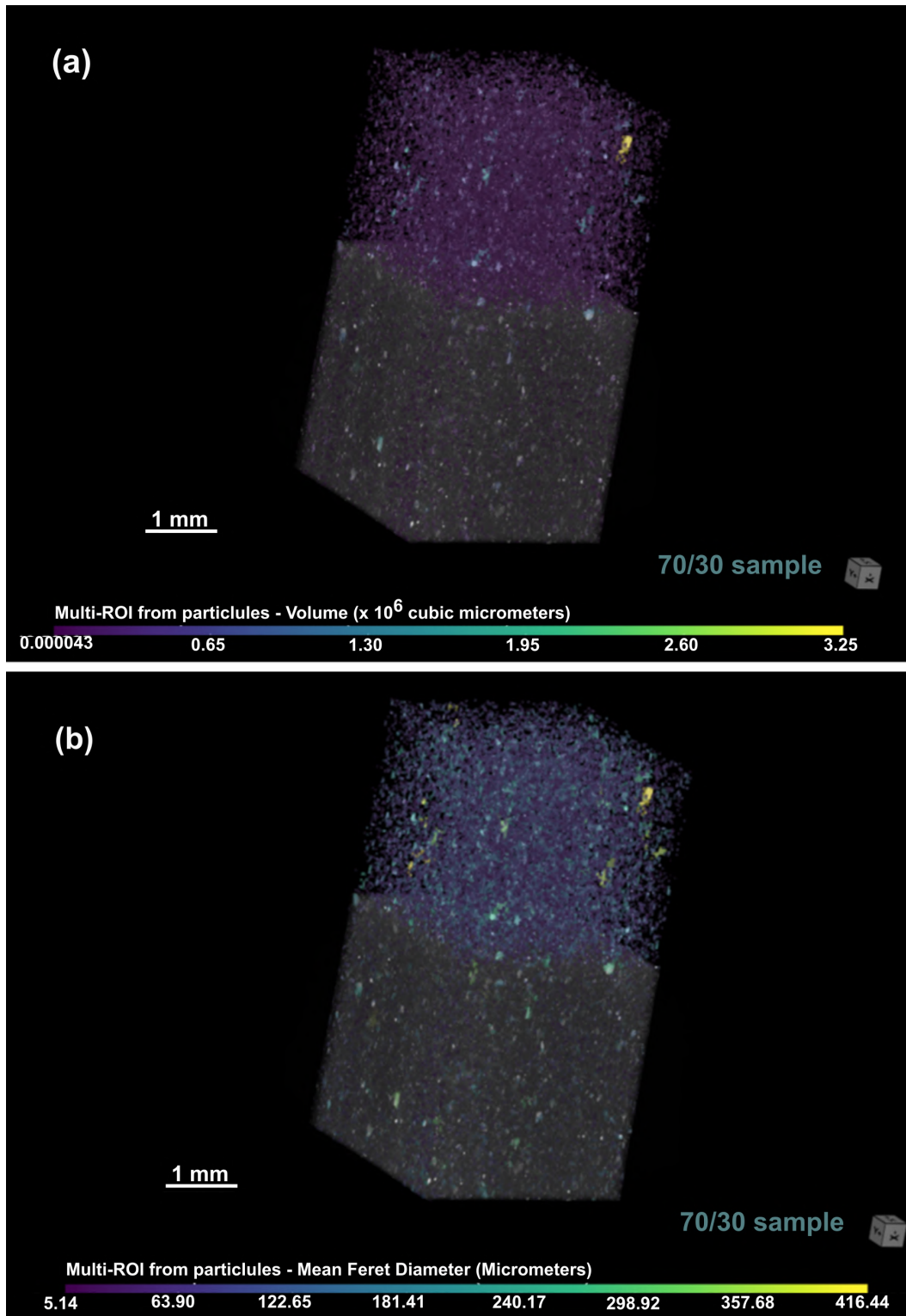


Figure 4.18: 3D rendering of 70/30 composite sample. Images show the particles colored according to (a) volume and (b) mean feret diameter scales. The polymer matrix is shown only on the bottom half in gray color.

be made by analyzing the size of each item identified as soapstone in the composite. Considering the previous analysis performed on the dispersed soapstone powder, reported in Section 4.1.1, in which 99% of the soapstone

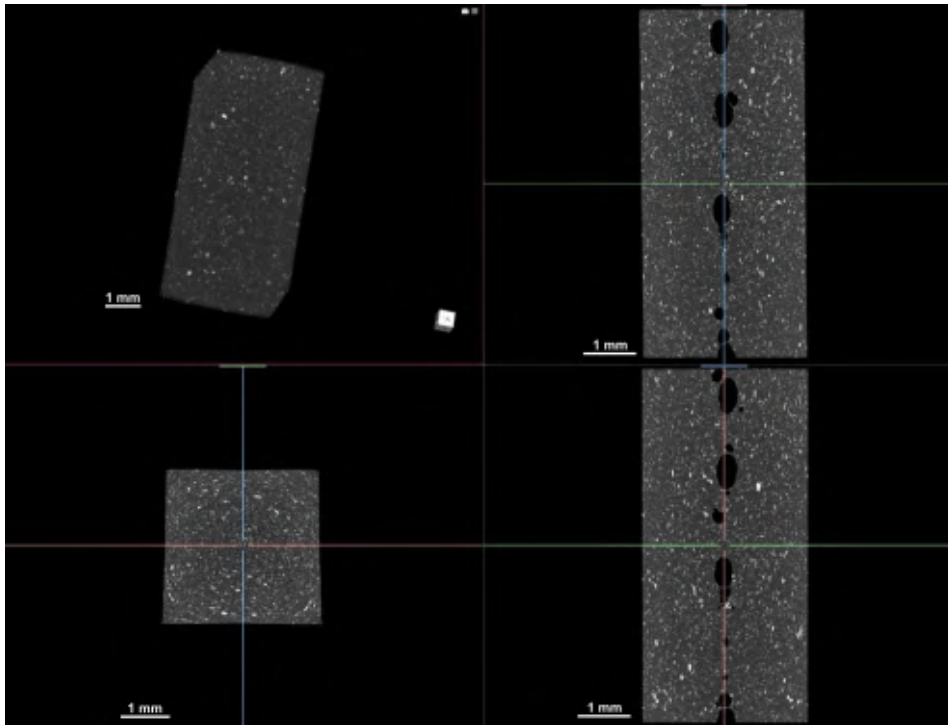


Figure 4.19: 3D rendering with orthogonal views of the 70/30 composite sample. Voids identified in the central region of the sample.

particles had a diameter equal to or smaller than $39.11 \mu\text{m}$, it is reasonable to use this value as an upper limit for the mean feret diameter of individual particles. By analyzing Fig. 4.20, that shows the histogram and descriptive statistics of the mean feret of the soapstone particles in each composite sample, it is possible to conclude that a considerable number of particles had larger diameters than that limiting value, which indicates that the great majority of these items are, in fact, agglomerated particles. Using this approximation, it was possible to classify particles into two categories: individual particles and clusters, as shown in Tab. 4.7. The percentage of particles in clusters increased with filler content, from 10% by number in the 90/10 up to 17% in the 70/30.

Table 4.7: Classification of the soapstone particles in different HDPE composite samples.

Sample	Individual particles		Clusters		Total particles
	Count $\times 10^5$	(%)	Count $\times 10^5$	(%)	Count $\times 10^5$
90/10	4.87	90	0.54	10	5.41
80/20	6.23	86	0.99	14	7.21
70/30	5.47	83	1.10	17	6.57

It is important to note that the percentages listed in Tab. 4.7 might not be precise due to resolution. According to the particle size distribution reported in Section 4.1.1, 40% of the particles had sizes smaller than or equal to $7.41 \mu\text{m}$. Thus, considering the $7 \mu\text{m}$ resolution of the micro CT, it is possible to

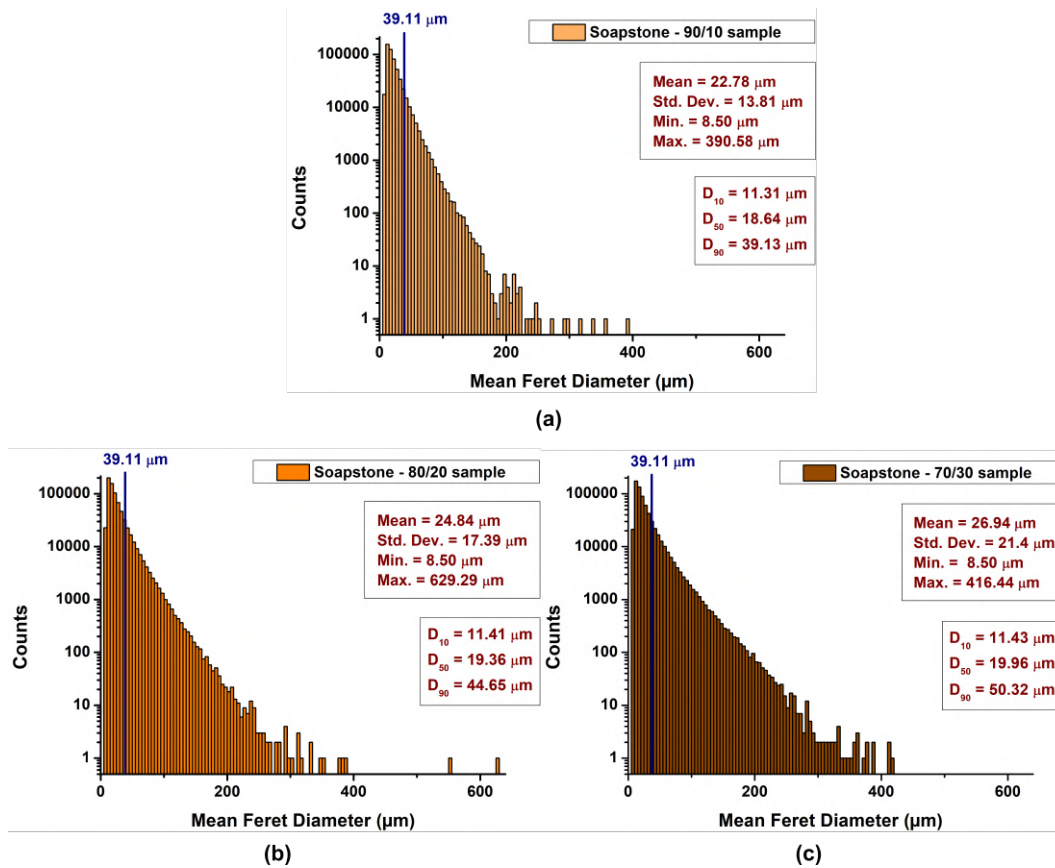


Figure 4.20: Mean feret diameter histograms of the soapstone filler identified in (a) 90/10, (b) 80/20 and (c) 70/30 samples, respectively.

presume that the percentage of individual particles is probably higher in each sample. However, the approach used is reasonable for comparative purposes.

The variability of the amount of reinforcement is better characterized by the the volume fraction and its spatial distribution. Therefore, the volume fraction of particles and voids, as well as the parameters revised in Section 2.5.4.1 were used to quantify the amount of clustering in each composite sample. The resulting values are listed in Tab. 4.8. These results reveal that both the volume fraction of particles in clusters (ζ) and the volume fraction of clusters in the composites (γ) increased as the particle loading increased, which indicates that the soapstone particles have a strong tendency of forming agglomerates in the polyethylene matrix, specially at higher filler loadings. This conclusion is in consonance with findings reported by Leong et al. [11], regarding commercial talc particles in a polypropylene matrix.

The values listed in Tab. 4.8 reveal that void content also increased with particle loading. As mentioned before, this phenomenon is related with increased polymer viscosity during processing. However, the volume fraction of voids was less than 1% for all samples, which is reasonable for most applications [108].

Table 4.8: Particle clustering parameters, void and filler content of the composite samples.

Sample	M_p (%)	Φ_p (%)	Φ_v (%)	ζ (%)	γ (%)
90/10	10	3.29	0.00	55.54	1.82
80/20	20	6.19	0.00	67.75	4.19
70/30	30	7.83	0.64	77.06	6.03

M_p , Φ_p : mass and volume fraction of particles in the composite, respectively; Φ_v : volume fraction of voids.

The uniformity of filler distribution was analyzed by dividing the composite samples into twelve subsets throughout the width and length of the sample, as shown in Fig. 4.21. The volume of the particles in each subset was measured and the local parameters defined in Section 2.5.4.1 calculated. The results are listed in Tab. 4.9, where the local volume fractions were compared with the total volume fraction of particles (Φ_p) in each sample. It is important to note that due to the randomness of the the distribution, some of the smaller particles located at the inner borders of each subset could not be measured properly. However, considering the microscopic scale of these particles the values listed in Tab. 4.9 can be considered as a very reasonable approximation.

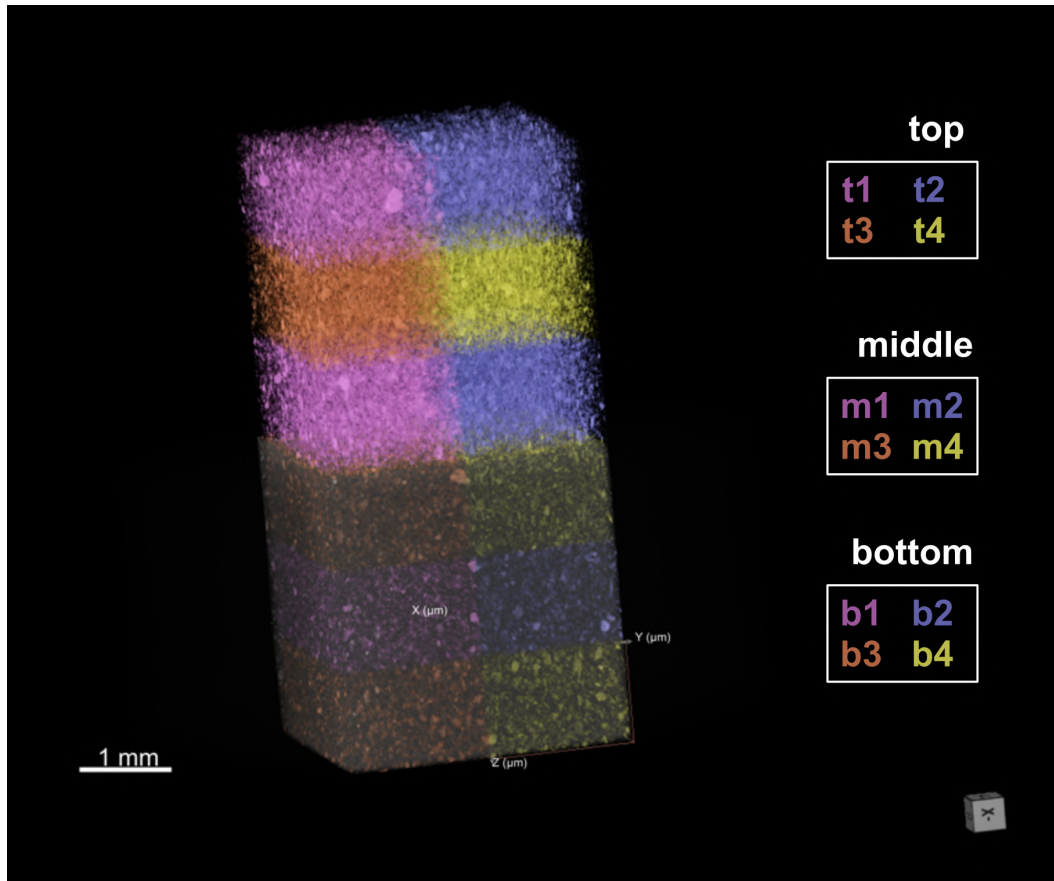


Figure 4.21: 3D rendering of a composite sample divided into twelve equal-sized subsets. The particles are colored according to the nomenclature.

Table 4.9: Comparisons between local fractions and the total volume fraction of particles of the composite samples.

Subset	90/10		80/20		70/30	
	ξ_p^{sub} (%)	Φ_p^{sub} (%)	ξ_p^{sub} (%)	Φ_p^{sub} (%)	ξ_p^{sub} (%)	Φ_p^{sub} (%)
t1	7.90	3.12	8.10	6.02	8.20	7.70
t2	7.93	3.13	8.22	6.10	8.30	7.80
t3	8.31	3.28	8.30	6.17	8.42	7.91
t4	8.10	3.20	8.20	6.09	8.44	7.93
m1	8.50	3.35	8.64	6.42	8.76	8.23
m2	8.61	3.40	8.56	6.36	8.50	7.98
m3	8.30	3.27	8.55	6.35	9.02	8.47
m4	8.43	3.32	8.47	6.29	8.86	8.32
b1	7.81	3.08	8.10	6.01	7.93	7.45
b2	7.96	3.14	8.00	5.94	7.32	6.88
b3	7.30	2.88	7.59	5.63	8.04	7.55
b4	7.61	3.00	7.46	5.54	7.40	6.95
Sample	100	3.29	100	6.19	100	7.83

The chi-square test of homogeneity was used to determine whether the volume distribution of particles is the same for the subsets, i.e., if the filler distribution in the composite samples can be considered statistically homogeneous. This test measures the amount that the observed counts in the samples deviate from the expected counts and determines whether two or more independent samples differ in their distributions on a single variable of interest. The calculations were done according to Franke et al. [109] and are detailed in Appendix A. For the fraction of particles in subset (ξ_p^{sub}) the expected values used were $1/n$ (8.33%), and the p-values obtained were less than 0.05 for all the samples. Thus, considering a 95% confidence level, the hypothesis of homogeneity can be accepted. The same analysis was done for the the local volume fraction of particles (Φ_p^{sub}), using the total volume fraction of particles (Φ_p) in each sample as the expected values. The p-values obtained were also less than 0.05 for all samples. Therefore, the volume distribution of particles in all three composite samples can be considered statistically homogeneous in the two directions studied.

4.2.4

Tensile Tests

Tensile tests were performed on neat HDPE and on the composite specimens to understand the effect of different loadings of soapstone on the mechanical properties of the polymer. Figure 4.22 shows a comparison between the typical stress-strain curves obtained for each material. It is possible to see a loss in ductility and in tenacity as the soapstone content increases, which is consistent with literature predictions. In general, the improvement in mechanical strength by incorporating fillers into thermoplastics is accompanied by a loss in ductility, since the particles cause a reduction in chain mobility, usually decreasing elongation at break [13]. This loss is even more evident at

higher filler loadings. The 80/20 and 70/30 composites presented stress-strain curves characteristic of brittle fracture, in opposition to the ductile behavior characteristic of HDPE [36]. These findings suggest that the presence of higher concentrations of the particles (above 20 wt%) modify the fracture mechanism of HDPE. This transition from ductile to brittle fracture can be associated with the nucleation effect of the mineral filler [110]. In fact, according to differential scanning calorimetry (DSC) results reported in the literature, talc is a strong nucleating agent when incorporated into polyolefins. Leong et al. [11] noted a considerable increase in both crystallization and onset temperatures in PP-talc composites, when compared with the virgin polymer. Similar results were reported for HDPE matrix talc-filled composites [47, 52]. According to Mehrjerdi et al. [47], the addition of talc accelerates the process of crystalline nuclei formation by multiplying the number of crystalline units in the HDPE matrix, generating a greater number of small but more regular crystalline units. This effect results in higher crystallinity, hence the composite is expected to obtain higher rigidity, better dimensional stability and increased strength [11].

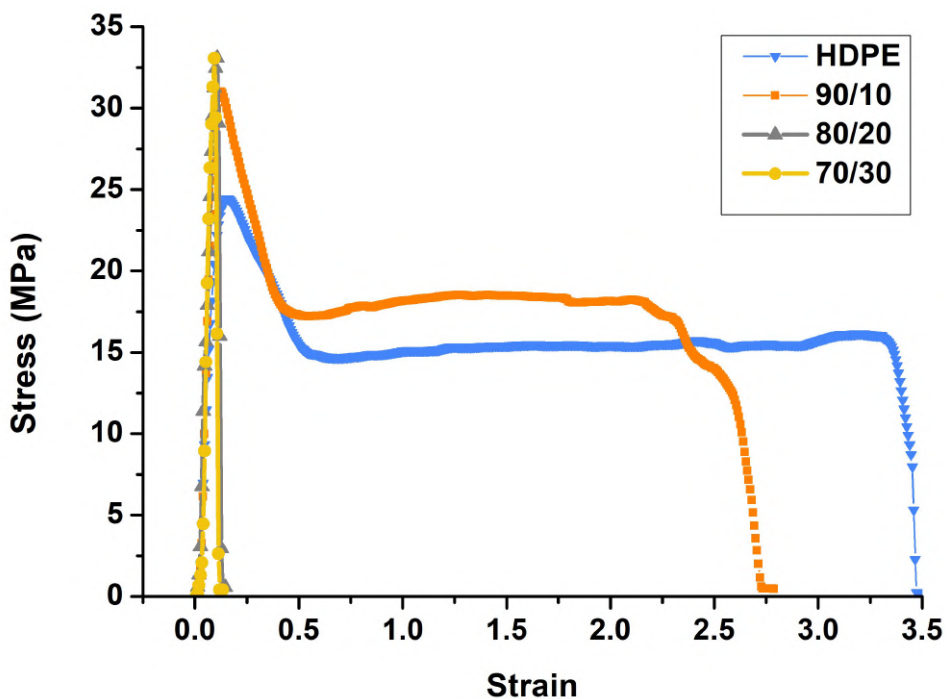


Figure 4.22: Stress-strain curves of a representative specimen of each material (HDPE and 90/10, 80/20 and 70/30 composites).

The mean values of the mechanical properties obtained from each composition are listed in Table 4.10, where SW stands for soapstone waste. Box-plots of some of these properties were also calculated in order to provide better visualization of the data statistics. Yield and tensile strength box-plots are shown in Fig. 4.23, while Fig. 4.24 shows the strain to failure and tenacity box-plots.

Table 4.10: Mechanical properties of unfilled and filled HDPE specimens determined by the tensile test.

SW loading (wt%)	Yield strength (MPa)	Tensile strength (MPa)	Strain to failure (mm/mm)	Tenacity (MJ/m ³)	Resilience (MJ/m ³)
0	25.8 ± 2.2	19.6 ± 3.8	4.4 ± 1.8	88.7 ± 41.6	2.3 ± 0.2
10	29.7 ± 0.6	17.5 ± 0.5	1.6 ± 0.6	44.1 ± 13.0	2.2 ± 0.2
20	32.9 ± 1.4	32.9 ± 1.4	0.1 ± 0.0	3.4 ± 1.6	2.1 ± 0.3
30	33.9 ± 0.8	33.9 ± 0.8	0.1 ± 0.0	1.6 ± 0.2	1.3 ± 0.2

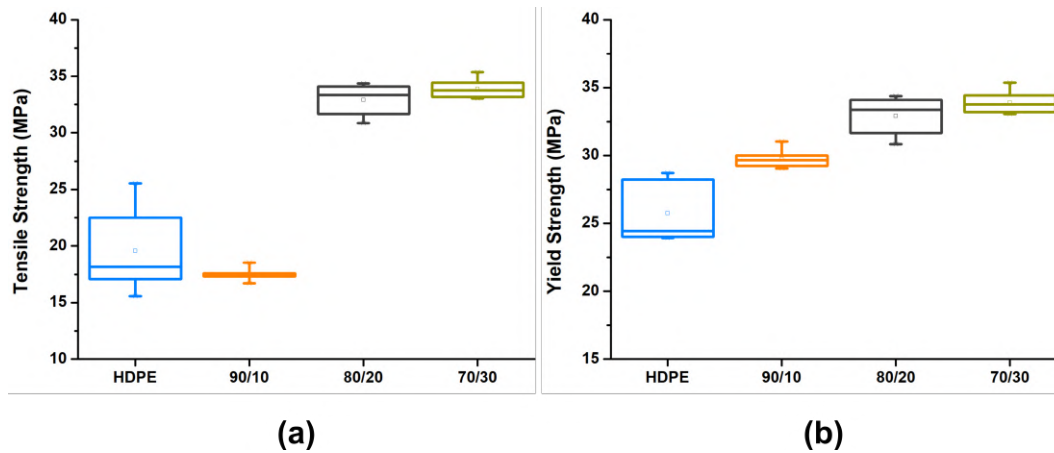


Figure 4.23: (a) Yield and (b) tensile strength box-plots.

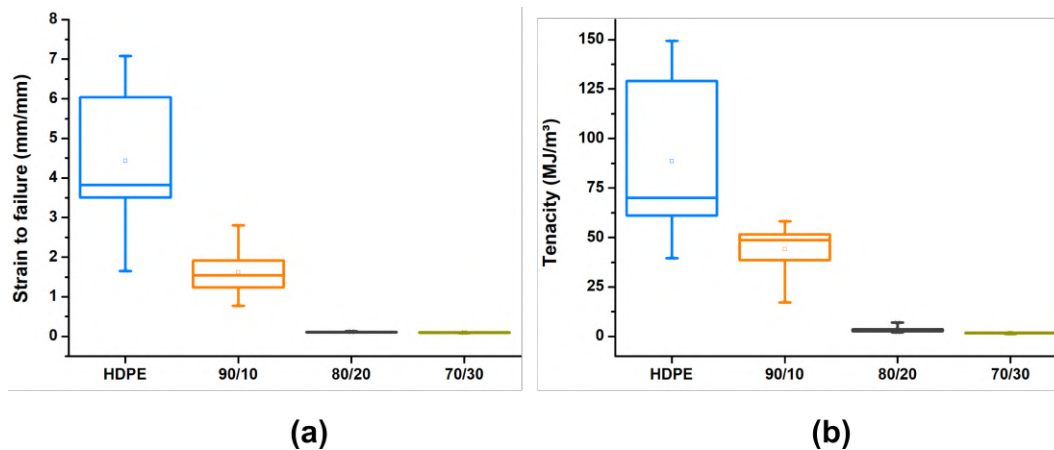


Figure 4.24: (a) Strain to failure and (b) tenacity box-plots.

As can be seen in the box-plots, the soapstone particles increased the yield strength of the polymer for all compositions tested. For the 70/30 composition, an increase of 31% in the mean yield strength and of 73% in the mean ultimate tensile strength was observed. One-way ANOVA analysis [111] was used to evaluate the significance of differences between the mean properties from each composition. The calculations are further detailed on Appendix A.2. The p -values obtained for all the properties listed in Table 4.10 were less than $\alpha = 0.05$, hence the effect of the addition of soapstone observed on the HDPE properties was statistically significant.

The experimental data reported in Tab. 4.10 was used to validate the macro-mechanical models described in Section 2.4. The filler volume fraction (ϕ_p) determined in Section 4.2.3 was used in the calculations.

The machine used to perform the mechanical tests (Fig. 3.9) is commonly referred to as a "soft" machine, which means that the elastic moduli measured in these tests account not only for the modulus of the specimen, but also for the machine's rigidity. However, as all the materials were tested under the same conditions, the effect of the filler on the polymer elastic modulus can be analysed by studying the relative modulus (E_c/E_m). The variation of the relative elastic modulus of HDPE as a function of the soapstone content is shown in Figure 4.25, along with curves corresponding to the theoretical models. The more general equations described in Section 2.4 were used to fit the data and the calculations were performed using the method of least squares. The values of the parameters, as well as the correlation coefficients, r , for each equation are summed up in Fig. 3.9. A value of 1.5 was assumed for the shape parameter A' in Halpin (Eq.2-7) and Nielsen's (Eq. 2-10) equations, considering this as an upper limit for a suspension of rigid spheres in a matrix with Poisson's ratio of approximately 0.50 [71]. Considering the particle analysis results reported in Section 4.1.1, a value of 0.52 was used for the maximum packing fraction (ϕ_{max}), which corresponds to maximum packing of elongated particles with aspect ratio of 1/5 [49]. The remaining parameters were adjusted to the curve within the theoretical limits detailed in Section 2.4.

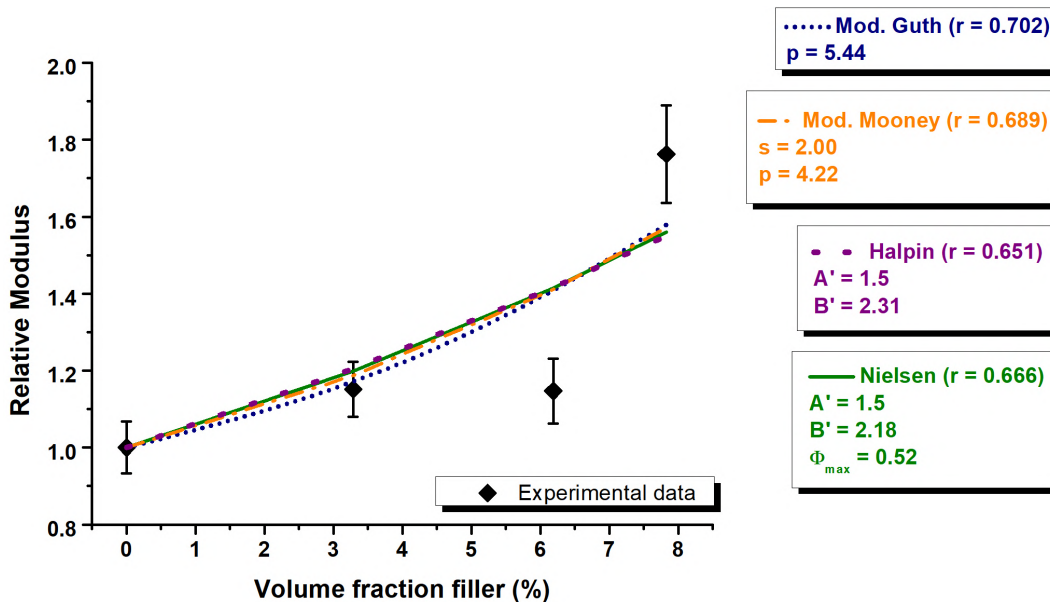


Figure 4.25: Relative E modulus versus filler content of the HDPE/soapstone composites. Error bars represent the 95% confidence interval.

As seen in Figure 4.25, the elastic modulus improved with the addition

of soapstone particles, specially for the 30 wt% (7.83 vol%) loading. However, the data was only reasonably fitted by the models, obtaining correlation coefficients (r) in the 0.651 to 0.702 range. It is important to note that the prediction of the elastic modulus of particulate polymer composites is a challenging approach, since many factors can affect the rigidity of a polymeric matrix. The modulus may vary with particle size and particle distribution. For instance, a more broad size distribution results in more compact packing and, thus, in higher values of the maximum packing fraction (ϕ_{max}) [52]. According to Bigg [49], talc contains a significant percentage of small isotropic particles which fit among the flakes, and increases the maximum packing fraction above the theoretical value. The results from Section 4.1.1 reveal that this is also the case for the soapstone waste particles. In addition, talc's nucleating effect also contributes to the increase in stiffness by enlarging the crystalline fraction of the HDPE matrix, which is not accounted for in these models [52]. The best correlation was obtained by the modified Guth model and the value of 5.44 obtained for the shape parameter (p) indicates that the particles are slightly elongated, which is in accordance with the particle analysis results reported in Section 4.1.1.

Figure 4.26 shows the filler influence on the yield strength of the HDPE/soapstone composites, where Equations (2-12)-(2-14) were used to fit the data. In the Turcsányi equation, the value of the shape parameter (A) was set as 2.5, which is the upper limit considering close packing of spherical particles [41]. The remaining parameters were adjusted to the curve within the theoretical limits detailed in Section 2.4. Calculations were performed using the method of least squares.

As it can be seen in Figure 4.26, the data was well fitted by all the models ($r > 0.97$). The concave downward shape from Equation (2-13) provided the best fit for the experimental data. The value of 1.21 obtained for the a parameter suggests that the particles caused stress concentration in the HDPE matrix. This observation can be linked to the particle clustering effect observed in the tomography analysis reported in Section 4.2.3, since the agglomerated particles can in fact cause stress concentration in the matrix structure [18]. However, the microCT results also revealed that, despite particle clustering, the volumetric distribution of the filler throughout the matrix was uniform, which can explain the effective enhancement in the polymer strength observed in Fig. 4.26. This conclusion can be supported by the value obtained for the b (1.00) parameter in Bigg's equation, which, according to theory, is an indicative that the fracture occurred through the matrix, and not through the interface. In addition, the values of the parameters c and d , in comparison

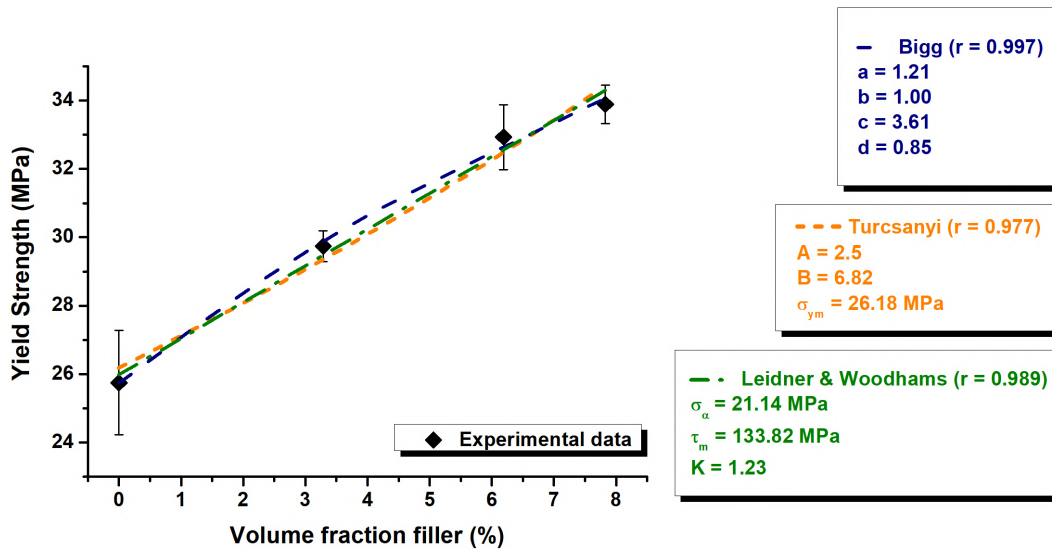


Figure 4.26: Yield tensile strength versus filler content of the HDPE/soapstone composites.

to those reported by Bigg [49] for Noryl/talc and ABS/talc composites (Tab. 2.19), imply that there was some particle-matrix adhesion, which promoted the reinforcement observed.

The Leidner and Woodhams model also provided a good correlation to the yield strength data. The value of 21.14 MPa for the interfacial tensile strength σ_i suggests a efficient interaction mechanism between phases. This conclusion was confirmed by the B parameter in Turcsányi's equation. The adjusted value of 6.82 is a quantitative indicator that there is good interfacial adhesion between the soapstone particles and the HDPE matrix, which resulted in the improvement in yield strength observed experimentally.

4.2.5 Creep Tests

As detailed in Section 3.2.3 the creep tests were performed with maximum duration of 48h, at constant load values, which corresponded to 50% of the material's yield strength determined by the tensile tests (Tab. 4.10). The load values were calculated by measuring the specimen's cross section area, which had small variations between different compositions. The resulting values are listed in Tab. 4.11.

Table 4.11: Creep test conditions.

SW loading		Stress (MPa)	Reference area (mm ²)	Load (N)
(wt%)	(vol %)			
0	0.00	12.90	10.23	132
10	3.29	14.85	10.24	152
20	6.19	16.45	10.56	174
30	7.83	16.95	10.57	179

The specimens after test are shown in Fig. 4.27, where the specimens are identified as S1 to S8. It can be seen that, overall, HDPE presented a ductile behavior, but the amount of creep strain was not uniform throughout the eight specimens. This lack of uniformity can be due to the molecular weight distribution of the polyethylene used, which can lead to small variations in density throughout the specimens. As emphasized by Hin et al. [59], variations in density have a strong effect in the creep response of HDPE. Some tests (for samples S3, S4 and S6) were interrupted before the maximum time duration or specimen rupture because the total elongation achieved was equal to the maximum displacement between grips allowed by the equipment. Therefore, the creep rupture of these specimens could not be evaluated. However, some interesting information can be extracted from the test data. The data obtained can be used to analyse the creep curve of HDPE and to assess the effect of the soapstone filler on the polymer's creep behavior. Figure 4.28 shows the resulting strain-time curves obtained for each composition. Since the curves were plotted in the same scale, it is possible to observe an decrease in both the maximum strain and rupture time with the increase in the soapstone waste loading. These observations are in accordance with the results reported by Ek et al. [63] for HDPE filled with CaCO_3 .

Additionally, the observation of the specimens after test can lead to conclusions regarding the creep mechanism taking place in this material under these tests conditions. These observations, including the classification of the type of failure according to Hin et al. [59] (Section 2.3.3), were summed up in Tab. 4.12, in which are also listed the values for the maximum strain and test duration for each HDPE specimen. It can be noted that, with the exception of S2 that presented only 18% strain (mostly elastic) in a 48h test, all HDPE specimens presented a necking and indications of cold drawing after neck formation.

Table 4.12: HDPE specimens creep response under constant load of 132N, at room temperature (23 ± 2 °C).

Specimen	Maximum strain	Test duration (h)	Characteristics
S1	0.38	11.74	Type A1 failure
S2	0.18	47.94	NR, no tertiary region
S3	0.41	27.43	NR, macro-necking and cold drawing
S4	0.40	13.24	NR, macro-necking and cold drawing
S5	0.39	15.50	Type A1 failure
S6	0.42	20.23	NR, macro-necking and cold drawing
S7	0.38	12.38	Type A1 failure
S8	0.44	46.13	NR, macro-necking and cold drawing

NR - specimen did not ruptured.

In the case of the composites, all specimens presented failure before the maximum test duration. The 90/10 composition specimens presented Type A1 creep failure. As can be seen in Fig. 4.27, the specimens presented

reasonable strain after neck formation. However, when compared with the neat HDPE, there was an overall decrease in strain. This observation was even more expressive for the 80/20 and 70/30 compositions. The 80/20 compositions appear to have failed immediately after the neck formation, thus being classified as Type A2 failure. According to Hin et al. [59], the plane of the fracture surface for Type A2 is approximately a plane perpendicular to the tensile axis but has a more jagged appearance than that demonstrated by Type B or Type C creep rupture. The 70/30 showed fracture surfaces characteristic of brittle failure, with fracture planes perpendicular to the tensile axis, low strain to failure (approximately 13%) and no macro-necking formation. As the specimens presented tertiary creep stages (Fig. 4.28), the failure can be classified as Type B, according to Hin et al. [59].

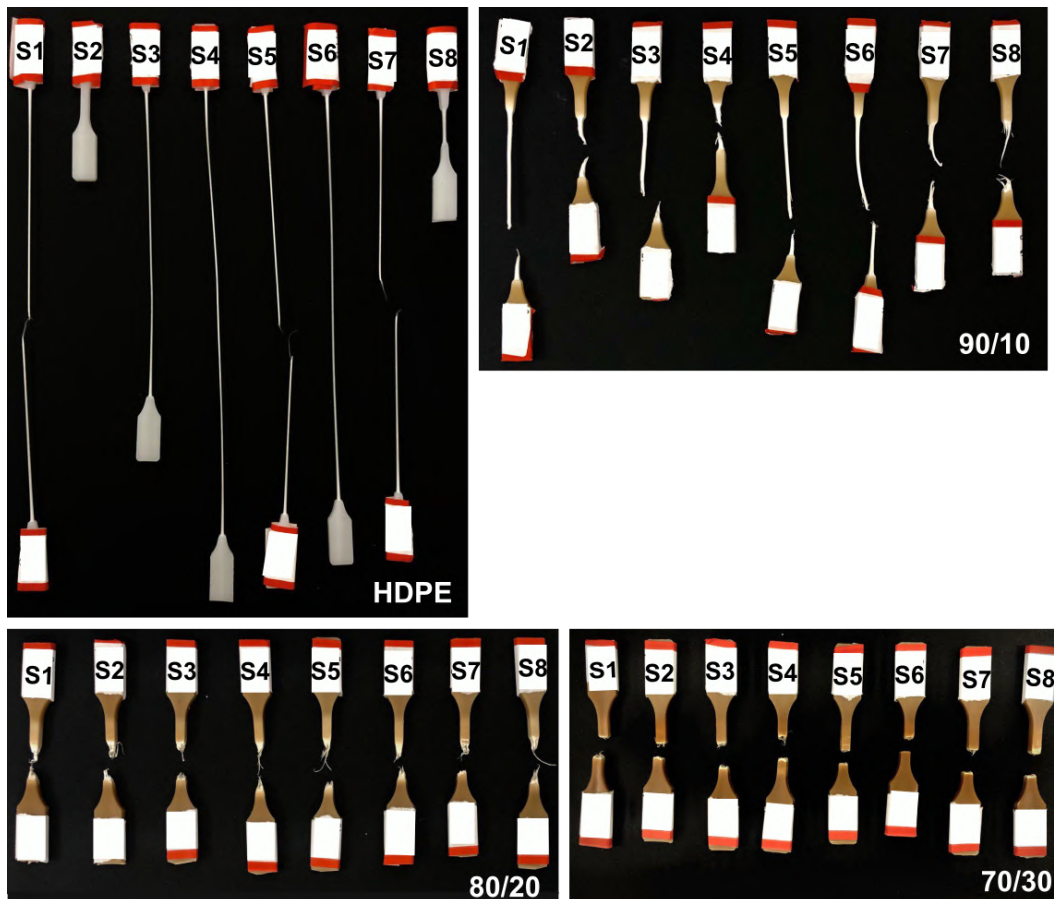


Figure 4.27: Specimens of each composition after creep testing.

In short, these findings are in disagreement with the results reported by Eftekhari et al. [57] for talc-filled polypropylene composites. The addition of higher fractions of soapstone appears to have indeed changed the failure mechanism of HDPE. The addition of 20 wt% of soapstone still resulted in ductile behavior, but the failure changed from Type A1 to Type A2, thus the particles appear to have restricted molecular flow. For the 30 wt% loading,

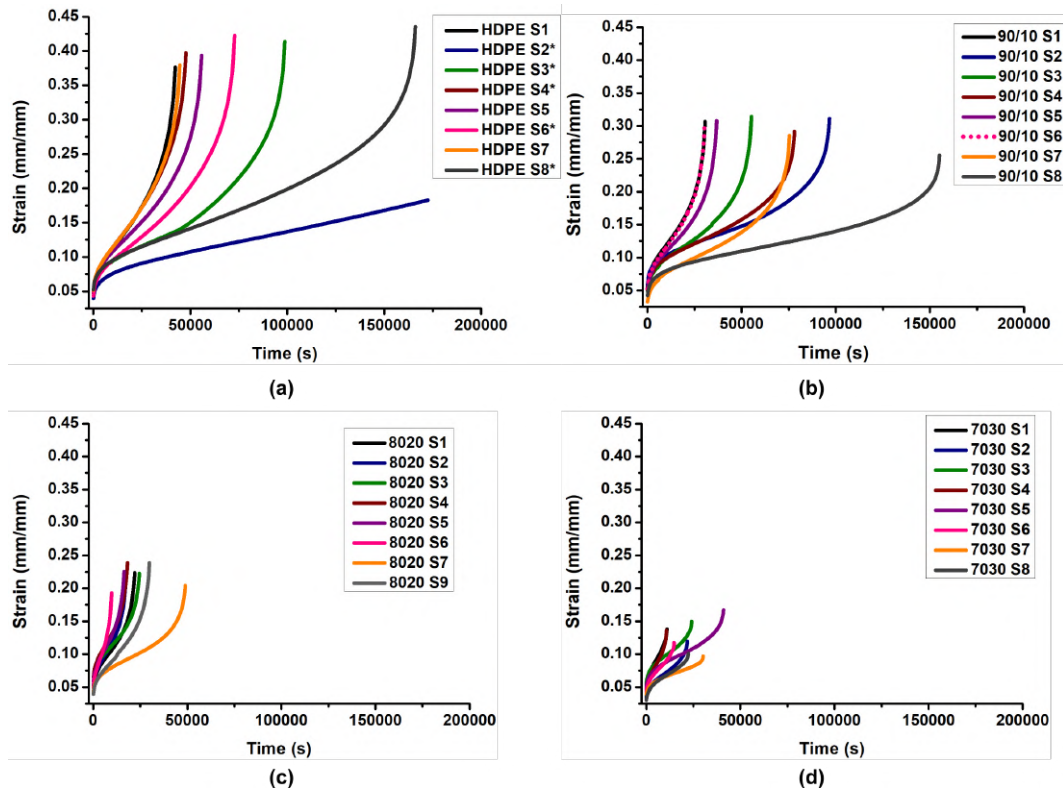


Figure 4.28: Strain-time curves for (a) neat HDPE, (b) 90/10, (c) 80/20 and (d) 70/30 composites. The * symbol was used to indicate that the specimen did not rupture.

this restriction was enough to change the mechanism of failure from ductile to brittle. These changes can also be linked to possible alterations in the polymer's morphology caused by soapstone. Hin et al. [59] pointed out that changes in the lamellar thickness of the spherulites could cause the brittle-ductile transition of the polymer. As previously mentioned, talc and, hence soapstone, has a nucleating effect in high-density polyethylene, which affects the number and size of the crystalline units [43].

The mean values of strain at failure and rupture time for the HDPE/soapstone composites are summed up in Tab. 4.13. It can be noted, that there was, in fact, a considerable decrease in both properties with the increase in the soapstone concentration. When compared with the 90/10 composition, the 70/30 composites presented a decrease of 56.7% in strain at failure and 68.5% in rupture time.

Table 4.13: Mean strain to failure and rupture time for the HDPE/soapstone composites. (Uncertainties indicate the standard deviation).

SW loading (wt%)	Strain to failure (mm/mm)	Rupture Time 1×10^4 (s)	Rupture Time (h)
10	0.30 ± 0.02	6.98 ± 4.22	19.38 ± 11.72
20	0.22 ± 0.02	2.33 ± 1.19	6.48 ± 3.31
30	0.13 ± 0.02	2.20 ± 1.02	6.10 ± 2.84

As mentioned before, the creep curve can be divided into three regions. The distinction between the three regions was done by calculating the first derivative of each strain-time curve, as shown in Fig. 4.29. It is known that the creep rate, $\dot{\epsilon} = d\epsilon/dt$, is minimum in the secondary or stationary creep region, being very close to zero [59]. Thus, by analysing the derivative of each curve it was possible to establish an optimal time interval for the calculation of the steady creep rate, in order to guarantee that all specimens were in fact in the second region in such interval. The results indicated that the 3600s-7200s (1h-2h) range was ideal. Therefore, the mean steady creep rate for each composition was calculated within this time interval and the results are listed in Tab. 4.14.

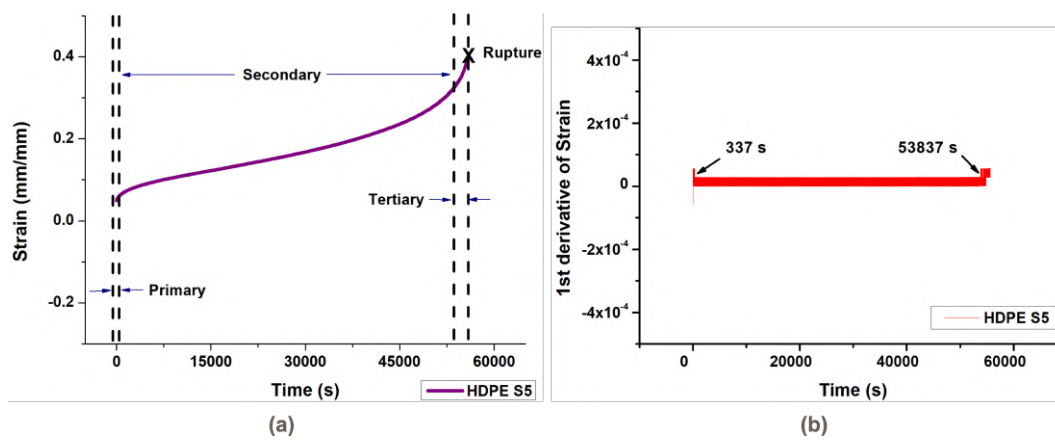


Figure 4.29: Example of determination of the stationary creep region: (a) strain-time curve and (b) first derivative of the strain-time curve indicating the time range in which the creep rate was stationary.

Table 4.14: Mean steady creep rate in the 1h-2h interval for each composition. (Uncertainties represent the standard deviation).

SW loading (wt%)	Creep rate $1 \times 10^{-6} \text{ (s}^{-1}\text{)}$
0	3.55 ± 0.97
10	3.32 ± 0.79
20	4.77 ± 2.30
30	3.06 ± 1.27

The mean steady creep rate obtained for HDPE was in the same order of magnitude as the one reported by Pereira et al. [62] for neat, unaged HDPE. One-way ANOVA was used to determine whether there were statistically significant differences between the mean creep rates. Further details of the calculations can be found in Appendix A.3. Since the p -value obtained (0.11) was higher than 0.05, considering a 95% confidence interval, it is possible to assume that the differences observed between the creep rate means were not statistically significant and only caused by scattering. These results lead to the

conclusion that, even though the soapstone filler decreased total creep strain, it did not affect the stationary creep rate of HDPE in the time interval studied. Since the literature regarding the creep behavior of particulate thermoplastic composites is still very poor, further investigations are required in order to explain the morphological aspect of these findings.

In regard to the practical behavior, the creep tests results revealed that the dimensional stability of HDPE can be improved by the addition of soapstone waste particles, since the total creep strain is considerably reduced. However, the particles also decreased the rupture time and altered the fracture mechanism for higher loadings (above 20%).

The next step in the creep behavior analysis would be to fit the viscoelastic models described in Section 2.4.2 to the experimental data and then extrapolate the creep response to longer periods of time. However, since most specimens ruptured under the conditions used in these tests, the time-extrapolation would not be reasonable. The modeling of the creep response of these materials is left as a suggestion for future works, where creep tests under different loads can be done, leading to more practical analysis and modeling.

5 Conclusions

The present work proposed and evaluated the use of soapstone waste as filler to HDPE composites. First, the waste was characterized using automated image analysis, X-ray diffraction, FTIR, and Raman spectroscopy. The image analysis of the dispersed waste revealed that most particles had a slightly elongated, circular shape and that 99% of them had diameters $\leq 39.11 \mu\text{m}$. Talc was the only mineral identified in the XRD and spectroscopy spectra, which indicated that the waste was mainly constituted of talc and if other minerals were present, their concentration was very low.

Infrared spectroscopy was also used to accomplish the chemical characterization of the composites and the comparisons between the neat polymer and the 30 wt% composition spectra revealed that no chemical reaction occurred between the HDPE and the soapstone particles. Rheological analysis assessed the influence of the soapstone particles on the polymer flow properties. The materials presented a pseudoplastic behavior and the filler had a negligible interference in the polymer shear stress. Only a marginal increase in the shear stress was observed in the 70/30 composites at low shear rates. The effect of the soapstone particles in the polymer viscosity was more expressive in the 80/20 and specially in the 70/30 composites, that presented enhanced viscosities in comparison with the neat polymer and this enhancement was more pronounced at lower shear rates. These results indicate that the addition of higher concentrations of soapstone powder (above 20 wt%) should require different melt conditions for processes that occur at low shear rates. Regarding extrusion and injection molding, the processing conditions can be similar to those of the neat polymer. The exception is the 70/30 ratio, that might require higher pressures in order to completely fill the mold cavity.

X-ray microtomography allowed both qualitative and quantitative analysis of particle distribution, void content and agglomeration in the different composite samples (with 10 wt%, 20 wt% and 30wt% loadings). Micro voids were identified in the 70/30 sample, with 0.64 vol% void fraction, which was due to the increase in viscosity during processing. The value $39.11 \mu\text{m}$ was used to classify the particles identified in the samples as individual particles or clusters. The analysis revealed that the soapstone particles have a tendency

of forming agglomerates in the HDPE matrix, and this tendency increases at higher filler loadings. The variability of reinforcement in the composite samples was analyzed by dividing the samples into twelve subsets throughout the width and length and measuring the volume of the particles in each subset. A statistic test of homogeneity revealed that, despite particle clustering, the distribution of particles can be considered homogeneous for all the composite samples in the direction studied, which is the direction of the applied load in tensile tests.

Tensile tests were used to determine the mechanical properties of the materials. Results revealed that the addition of soapstone particles resulted in more brittle and rigid composites, but with higher values of both yield and tensile strength. The relationship between the microstructure and the macroscopic mechanical behavior was done by fitting tensile test data with micro-mechanical models from the literature. The tensile yield strength of HDPE increased up to 31% with particle loading, which can be linked with the homogeneous filler distribution observed in the composites microstructure. The yield strength was well fitted by the models tested and the analysis of the adjusted parameters lead to the conclusion that there was good interfacial adhesion between the soapstone particles and the HDPE matrix. The elastic modulus improved with the addition of soapstone particles, specially for the 30 wt% (7.83 vol%) loading. However, the data was only reasonably fitted by the literature models.

Additionally, constant load creep tests were performed at room temperature. Results revealed that the addition of soapstone waste particles reduced the creep strain of HDPE, which can lead to better dimensional stability of HDPE of end products. However, the particles also decreased the rupture time and altered the fracture mechanism for higher loadings. The 70/30 composites presented characteristics of brittle fracture in opposition to the ductile behavior observed for the neat HDPE under similar conditions.

Further analysis on the microstructural changes that happen under constant load and at different temperatures are possible approaches for future works regarding these materials. Thermal analysis such as thermogravimetric analysis (TGA) and differential scanning calorimetry (DSC) could be used to confirm the effect of the soapstone on the polymer's thermal stability and crystallinity, respectively. Measurements on the composites density can be done to confirm the void content observed with microtomography. Additionally, a more accurate assessment of particle clustering can be done by using a micro CT with internal microscope. By combining the micro CT with a microscopic lens the resolution can be improved and it might be possible to identify

individual particles inside a cluster.

Overall, the results obtained so far indicate that the soapstone waste is a promising reinforcement for HDPE composites. Since the mechanical strength and the dimensional stability of the polymer improved with filler addition, the material can be a very interesting alternative for pipe applications, for example. Another possible application can be found in the automotive industry, as a dashboard material.

Bibliography

- [1] R. Sahu et al. “Moisture resistant stones waste based polymer composites with enhanced dielectric constant and flexural strength.” In: *Composites Part B: Engineering* 182.4 (2020), p. 107656.
- [2] A Girge et al. “Industrial waste filled polymer composites – A review.” In: *Materials Today: Proceedings* (2021), pp. 2214–7853.
- [3] W A Sadik et al. “Innovative high-density polyethylene/waste glass powder composite with remarkable mechanical, thermal and recyclable properties for technical applications.” In: *Heliyon* 7.4 (2021), e06627.
- [4] Anne Huhta and Aulis Kärki. “A proposal for the definition, nomenclature, and classification of soapstones.” In: *GFF* 140 (2018), pp. 38–43.
- [5] M.L.M Rodrigues and R.M.F Lima. “Cleaner production of soapstone in the Ouro Preto region of Brazil: a case study.” In: *Journal of Cleaner Production* 32 (2012), pp. 149–156.
- [6] D. Sinniah. “Industry and Cosmetic Uses of Talc with their Implication on Health.” In: *IeJSME* 5 (2011), pp. 10–16.
- [7] D. Assis, I. Yoshida, and M. Schiavon. “Caracterização do pó de pedra-sabão produzido em Congonhas (MG) para a preparação de compósitos de matriz cerâmica.” In: *29ª Reunião Anual da Sociedade Brasileira de Química*. Águas de Lindóia, Brasil, 2006, pp. 1–2.
- [8] R. Santos, W. Sousa, and H. Lima. “Estudo da pedra-sabão na região de ouro preto - MG.” In: *XXIII Encontro Nacional de Tratamento de Minérios e Metalurgia Extrativa*. Gramado, Brasil, 2009, pp. 741–748.
- [9] H. P. Faria et al. “Talcosis in soapstone artisans: High-resolution CT findings in 12 patients.” In: *Clinical Radiology* 69 (2014), e136–e139.
- [10] O. M. P. A. Bezerra et al. “Talc pneumoconiosis among soapstone handicraft workers in a rural area of Ouro Preto, Minas Gerais, Brazil.” In: *Cad. Saúde Pública* 19 (2003), pp. 1751–1759.

- [11] Y.W. Leong et al. “Comparison of the Mechanical Properties and Interfacial Interactions Between Talc, Kaolin, and Calcium Carbonate Filled Polypropylene Composites.” In: *J. Appl. Polym. Sci.* 91 (2004), 3315–3326.
- [12] L. Lapcik, Jr. et al. “Effect of the Talc Filler Content on the Mechanical Properties of Polypropylene Composites.” In: *J. Appl. Polym. Sci.* 110 (2008), pp. 2742–2747.
- [13] A.K. Mehrjerdi et al. “Mechanical and Thermo-Physical Properties of High-Density Polyethylene Modified with Talc.” In: *J. Appl. Polym. Sci.* 129 (2013), pp. 2128–2138.
- [14] A.K. Mehrjerdi et al. “Effects of a Titanate Coupling Agent on the Mechanical and Thermo-Physical Properties of Talc-Reinforced Polyethylene Compounds.” In: *J. Appl. Polym. Sci.* 131 (2014), e40449.
- [15] M.R. Kamal and A. Mutel. “Rheological Properties of Suspensions in Newtonian and Non-Newtonian Fluids.” In: *J. Polym. Eng.* 5 (1985), pp. 293–382.
- [16] N.J. Mills. “The Rheology of Filled Polymers.” In: *Journal of Applied Polymer Science* 15 (1971), pp. 2791–2805.
- [17] P. Mederic et al. “Talc Filled Thermoplastic Composites: Melt Rheological Properties.” In: *Applied Rheology* 13 (2003), pp. 297–304.
- [18] J.N. Dastgerdia et al. “Multiscale microstructural characterization of particulate-reinforced composite with non-destructive X-ray micro- and nanotomography.” In: *Composite Structures* 194 (2018), pp. 292–301.
- [19] N. Garcia et al. “Caracterização de talco purificado de resíduos de pedra sabão.” In: *Holos* 3 (2014), 69–77.
- [20] M. Vavro et al. “Soapstone as a locally used and limited sculptural material in remote area of Northern Moravia (Czech Republic).” In: *Environ Earth Sci* 73 (2015), 4557–4571.
- [21] G.J. Rosasco and J.J. Blaha. “Raman Microprobe Spectra and Vibrational Mode Assignments of Talc.” In: *Applied Spectroscopy* 34 (1980), pp. 140–144.
- [22] A.M. Hofmeister and J.E. Bowey. “Quantitative infrared spectra of hydrosilicates and related minerals.” In: *Mon. Not. R. Astron. Soc.* 367 (2006), 577–591.

- [23] M. Rodrigues. “Technological characterization of soapstone waste from craft workshops in the region of Ouro Preto.” Master Thesis (in Portuguese). Ouro Preto: Federal University of Ouro Preto, 2010.
- [24] J.W. Gruner. “The crystal structures of talc and pyrophyllite.” In: *Zeitschrift für Kristallographie – Crystalline Materials* 88 (1934), 412–419.
- [25] K. Momma and F. Izumi. “VESTA 3 for three-dimensional visualization of crystal, volumetric and morphology data.” In: *J. Appl. Crystallogr.* 44 (2011), pp. 1272–1276.
- [26] C. Baita et al. “An integrated Raman and petrographic characterization of Italian mediaeval artifacts in pietra ollare (soapstone).” In: *J. of Raman Spectroscopy* 45 (2014), 114–122.
- [27] R.C.C. Ribeiro and N.F. Castro. “Weathering of soapstone that covers the "Christ Redeemer" statue, Rio de Janeiro, Brazil.” In: *Global Stone Congress*. Borba, Portugal, 2012, pp. 1–7.
- [28] *Mineral Commodity Summaries*. U.S. Geological Survey. Jan. 2020. URL: <https://www.usgs.gov/media/files/talc-and-pyrophyllite-mcs-2019-data-sheet>.
- [29] *Sumário Brasileiro Mineral*. Agência Nacional de Mineração. Apr. 2017. URL: https://www.gov.br/anm/pt-br/centrais-de-conteudo/publicacoes/serie-estatisticas-e-economia-mineral/sumario-mineral/sumariomineral_2017.
- [30] K. Johansson et al. “Industrial minerals and rocks, aggregates and natural stones in the Nordic countries.” In: *Episodes* 31 (2008), pp. 133–139.
- [31] T. Luukkonen et al. “Alkali-activated soapstone waste - Mechanical properties, durability, and economic prospects.” In: *Sustainable Materials and Technologies* 22 (2008), pp. 1–8.
- [32] L. Bunse. “Exploring production and use of soapstone in Norway: Towards an interdisciplinary approach?” In: *AmS-Varia* 58 (2014), pp. 45–59.
- [33] R.M.F. Lima, D.M. Braga, and F.B.R. Silva. “Technological characterization of soapstone from Santa Rita de Ouro Preto/Brazil.” In: *Proceedings of Fifth International Materials Symposium*. Lisbon, Portugal, 2009, p. 8.
- [34] V. Balek et al. “Thermal Behavior of Ground Talc Mineral.” In: *Journal of Mining and Metallurgy* 44 (2008), pp. 7–17.

- [35] L.M. Mota et al. “Soapstone reinforced hydroxyapatite coatings for biomedical applications.” In: *Journal of Applied Polymer Science* 18 (1974), pp. 1639–1654.
- [36] C. Vasile and M. Pascu. *Practical Guide to Polyethylene*. Shawbury: Rapra Technology Limited, 2005.
- [37] Jr. W. D. Callister and D. G. Rethwisch. *Ciência e Engenharia dos Materiais: Uma Introdução*. 8th. Rio de Janeiro: LTC, 2012.
- [38] F.M.B. Coutinho, I.L. Mello, and L.C. de Santa Maria. “Polietileno: Principais Tipos, Propriedades e Aplicações.” In: *Polímeros: Ciência e Tecnologia* 13 (2003), pp. 1–13.
- [39] H.R. Kricheldorf, O. Nuyken, and G. Swift. *Handbook of Polymer Synthesis*. 2nd. New York: Marcel Dekker, 2005.
- [40] K.K. Chawla. *Composite Materials: Science and Engineering*. 3rd. New York: Springer, 2012.
- [41] B. Turcsányi, B. Pukanszky, and F. Tudós. “Composition dependence of tensile yield stress in filled polymers.” In: *Journal of Materials Science Letters* 7 (1988), pp. 160–162.
- [42] S. Ahmed and F.R. Jones. “A review of particulate reinforcement theories for polymer composites.” In: *J. Mater. Sci.* 25 (1990), pp. 4933–4942.
- [43] A. K. Mehrjerdi, T. Bashir, and M. Skrifvars. “Melt rheology and extrudate swell properties of talc filled polyethylene compounds.” In: *Heliyon* 6 (2020), e04060. DOI: <https://doi.org/10.1016/j.heliyon.2020.e04060>.
- [44] N.S.Eiriz, R.C.C. Ribeiro, and M. G. Oliveira. “Próteses Ortopédicas Formadas Por Resíduos de Rochas e Polietileno de Alta Densidade (PEAD).” In: *23^oCBECiMat - Congresso Brasileiro de Engenharia e Ciência dos Materiais*. Foz do Iguaçu, Brasil, 2018, pp. 3688–3694.
- [45] G.V. Vinograov and A.I. Malin. *Rheology of polymers: viscoelasticity and flow of polymers*. Moscow: Springer-Verlag Berlin Heidelberg, 1980.
- [46] R.E. Bretas and M.A. Dávila. *Reologia de Polímeros Fundidos*. 2nd. São Carlos: EdUFSCar, 2005.
- [47] A. K. Mehrjerdi. “Thermally Conductive High-Density Polyethylene Composites for Ground Heat Exchangers.” *Doctoral Thesis*. Borås: Högskolan i Borås, 2020.

- [48] C.H. Suh and J.L. White. “Talc-thermoplastic compounds: particle orientation in flow and rheological properties.” In: *J. Non-Newtonian Fluid Mechanics* 62 (1996), pp. 175–206.
- [49] D. M. Bigg. “Mechanical Properties of Particulate Filled Polymers.” In: *Polymer Composites* 8.2 (1987), pp. 115–122.
- [50] J. Z. Liang and R. K. Y. Li. “Prediction of tensile yield strength of rigid inorganic particulate filled thermoplastic composites.” In: *J. Mater. Process. Technol.* 83 (1998), pp. 127–130.
- [51] J.R.M. d’Almeida and L.H. de Carvalho. “An investigation on the tensile strength of particulate filled polymeric composites.” In: *Journal of Materials Science* 33 (1998), pp. 2215–2219.
- [52] S. Karrad, J.-M. Lopez, and A. Crespy. “Influence of a fine talc on the properties of composites with high density polyethylene and polyethylene/polystyrene blends.” In: *Journal of Materials Science* 33 (1998), pp. 453–461.
- [53] G. Savini and R. L. Oréfice. “Comparative study of HDPE composites reinforced with microtalc and nanotals: high performance filler for improving ductility at low concentration levels.” In: *J Mater Res and Tech* 9 (2020), pp. 16387–16398.
- [54] R. M. Guedes. *Creep and fatigue in polymer matrix composites*. Cambridge, UK: Woodhead Publishing Limited, 2011.
- [55] J. Lai and A. Bakker. “Analysis of the non-linear creep of high-density polyethylene.” In: *Polymer* 36 (1995), pp. 93–99.
- [56] M. Amjadi and A. Fatemi. “Creep behavior and modeling of high-density polyethylene (HDPE).” In: *Polymer Testing* 94 (2021), p. 107031.
- [57] M. Eftekhari and A. Fatemi. “Creep behavior and modeling of neat, talc-filled, and short glass fiber reinforced thermoplastics.” In: *Composites Part B* 97 (2016), pp. 68–83.
- [58] K. Nitta and H. Maeda. “Creep behavior of high density polyethylene under a constant true stress.” In: *Polymer Testing* 29 (2010), pp. 60–65.
- [59] T. S. Hin and B. W. Cherry. “Creep rupture of a linear polyethylene: 1. Rupture and pre-rupture phenomena.” In: *Polymer* 25 (1984), pp. 727–734.

- [60] C. R. López-Barrón et al. “Molecular Alignment in Polyethylene during Cold Drawing Using In- Situ SANS and Raman Spectroscopy.” In: *Macromolecules* 50.9 (2017), 3627–3636.
- [61] G.A.S. Silva. “Development and Characterization of HDPE/PA12 Blends.” Master Thesis (in Portuguese). Rio de Janeiro: Pontifical Catholic University of Rio de Janeiro, 2018.
- [62] A.A.C. Pereira, J.R.M. d’Almeida, and T.M.L. Castro. “Evaluation of Short-term Creep Behavior of PE-HD After Aging in Oil Derivatives.” In: *Polymers and Polymer Composites* 26 (2018), pp. 1–8.
- [63] C.-G. Ek, J. Kubát, and M. Rigdahl. “Stress relaxation, creep, and internal stresses in high density polyethylene filled with calcium carbonate.” In: *Rheologica Acta* 26 (1987), pp. 55–63.
- [64] A. Einstein. *Investigation on theory of Brownian motion*. New York: Dover, 1956.
- [65] E. Guth. “Theory of filler reinforcement.” In: *Journal of Applied Physics* 16.1 (1945), pp. 20–25.
- [66] S.-Y. Fu et al. “Effects of particle size, particle/matrix interface adhesion and particle loading on mechanical properties of particulate–polymer composites.” In: *Composites: Part B* 39 (2008), 933–961.
- [67] M. Mooney. “The viscosity of a concentrated suspension of spherical particles.” In: *J. Colloid. Sci.* 6 (1951), pp. 162–170.
- [68] J. G. Brodnyan. “The Concentration Dependence of the Newtonian Viscosity of Prolate Ellipsoids.” In: *Transactions of the Society of Rheology* 3 (1959), pp. 61–68.
- [69] J. C. Halpin. “Stiffness and expansion estimates for oriented short fiber composites.” In: *J. Composites Materials* 3.4 (1969), 732–734.
- [70] P. A. Mahanwar, S. Bose, and A. V. Tirumalai. “The Influence of Interfacial Adhesion on the Predicted Young’s Modulus of Mica-Reinforced Nylon-6.” In: *Polymer-Plastics Technology and Engineering* 45.5 (2006), pp. 597–600.
- [71] L.E. Nielsen. “Generalized Equation for the Elastic Moduli of Composite Materials.” In: *Journal of Applied Physics* 41 (1970), pp. 4626–4627.
- [72] L.E. Nielsen. “Simple Theory of Stress-Strain Properties of Filled Polymers.” In: *Journal of Applied Polymer Science* 10 (1966), pp. 97–103.

- [73] J.R.M. d'Almeida, F.L. Ribeiro, and I.G. Alves. "Wear behavior of a polymer-matrix composite reinforced with residues from a hydrometallurgical process." In: *Polymer-Plastics Technology and Engineering* 48 (2009), 1304–1309.
- [74] J. Leidner and R.T. Woodhams. "Strength of polymeric composites containing spherical fillers." In: *Journal of Applied Polymer Science* 18 (1974), pp. 1639–1654.
- [75] R.J. Young and P. A. Lovell. *Introduction to Polymers*. 3rd. Boca Raton: CRC Press, 2011.
- [76] A.A.C. Pereira, L.R. Souza, and J.R.M. d'Almeida. "Análise do comportamento à fluência de polímeros e compósitos poliméricos submetidos a envelhecimento por ação de fluidos." In: *13^o Congresso Brasileiro de Polímeros*. Natal, Brasil, 2015, pp. 1–5.
- [77] D.H. Hamer, F.R. Rolle, and J.P. Schelz. "Characterization of talc and associated minerals." In: *American Industrial Hygiene Association Journal* 37 (1976), pp. 296–304.
- [78] B.Y. Shekunov et al. "Particle Size Analysis in Pharmaceutics: Principles, Methods and Applications." In: *Pharmaceutical Research* 24 (2006), pp. 203–227.
- [79] K. Leschonski. "Representation and Evaluation of Particle Size Analysis Data." In: *Part. Charact.* 1 (1984), pp. 89–95.
- [80] F.M. Etzler and M.S. Sanderson. "Particle Size Analysis: a Comparative Study of Various Methods." In: *Part. Part. Syst. Charact.* 12 (1995), pp. 217–224.
- [81] D.J. Burgess et al. "Particle Size Analysis: AAPS Workshop Report, Cosponsored by the Food and Drug Administration and the United States Pharmacopeia." In: *The AAPS Journal* 6 (2004), pp. 1–12.
- [82] Malvern Instruments Limited. *A basic guide to particle characterization*. Technical Note. 2015 (accessed October 14, 2020). URL: https://www.cif.iastate.edu/sites/default/files/uploads/Other_Inst/Particle%20Size/Particle%20Characterization%20Guide.pdf.
- [83] HORIBA Instruments Inc. *Particle Size Result Interpretation: Number vs. Volume Distributions*. TN154. Technical Note. 2008 (accessed July 5, 2020). URL: https://www.horiba.com/en_en/static-light-scattering-sls-particle-size-result-interpretation/.

- [84] U. Ulusoy and I. Kursun. “Comparison of different 2D image analysis measurement techniques for the shape of talc particles produced by different media milling.” In: *Minerals Engineering* 24 (2011), pp. 91–97.
- [85] A.P.F. Albers et al. “Um método simples de caracterização de argilominerais por difração de raios X.” In: *Cerâmica* 48 (2002), pp. 34–37.
- [86] N. Kasai and M. Kakudo. *X-Ray Diffraction by Macromolecules*. Tokyo: Kodansha Ltd. and Springer, 2005.
- [87] M. Wesolowski. “Thermal decomposition of talc: A review.” In: *Thermochimica Acta* 78.1 (1984), pp. 7–17.
- [88] S. B. Hendricks. “On the Crystal Structure of Talc and Pyrophyllite.” In: *JeJSME* 99.1 (1938), pp. 264–274.
- [89] B. D. CULLITY. *Elements of X-ray diffraction*. Reading: Addison-Wesley, 1956.
- [90] RRUFF. *Talc R050058*. Database (accessed June 09, 2020). URL: <https://rruff.info/all/chemistry/asc/R050058>.
- [91] J.J. Blaha and G.J. Rosasco. “Raman Microprobe Spectra of Individual Microcrystals and Fibers of Talc, Tremolite, and Related Silicate Minerals.” In: *Analytical Chemistry* 50 (1978), pp. 892–896.
- [92] J. Coates. “Interpretation of Infrared Spectra, A Practical Approach.” In: *Encyclopedia of Analytical Chemistry*. Chichester, 2000, pp. 10815–10837.
- [93] Q. Zhanga et al. “Biochar filled high-density polyethylene composites with excellent properties: Towards maximizing the utilization of agricultural wastes.” In: *Industrial Crops and Products* 146 (2020), p. 112185.
- [94] D.L. Pavia et al. *Introduction to Spectroscopy*. 4th. Belmont: Cengage Learning, 2009.
- [95] N.B. Colthup, L.H. Daly, and S.E. Wiberley. *Infrared and Raman Spectroscopy*. 3rd. San Diego: Academic Press, Inc., 1990.
- [96] J. Barnes and B. Fanconi. “Critical Review of Vibrational Data and Force Field Constants for Polyethylene.” In: *J. Phys. Chern. Ref. Data* 7 (1978), pp. 1309–1321.
- [97] B. Wunderlich. *Macromolecular Physics, 1, Crystal structure, Morphology, Defects*. New York: Academic Press, 1973.

- [98] J.-L. Xu et al. “FTIR and Raman imaging for microplastics analysis: State of the art, challenges and prospects.” In: *Trends in Analytical Chemistry* 119.4 (2019), p. 115629.
- [99] M.R. Kakar et al. “Analysis of waste polyethylene (PE) and its by-products in asphalt binder.” In: *Construction and Building Materials* 280 (2021), p. 122492.
- [100] N. Landis and D.T. Keane. “X-ray microtomography.” In: *Materials Characterization* 61 (2010), pp. 1305–1316.
- [101] L. Salvo et al. “X-ray micro-tomography an attractive characterisation technique in materials science.” In: *Nuclear Instruments and Methods in Physics Research Section B: Beam Interactions with Materials and Atoms* 200 (2003), pp. 273–286.
- [102] D. Karimi and A.S. Milani. “SRVE modeling of particulate polymer matrix composites with irregularly shaped inclusions: Application to a green stone composite.” In: *Composite Structures* 228 (2019), p. 111331.
- [103] *High Density Polyethylene IA59U3*. Data Sheet. Braskem. 2018.
- [104] A. Buades, B. Coll, and J.-M. Morel. “A non-local algorithm for image denoising.” In: *IEEE Computer Society Conference on Computer Vision and Pattern Recognition (CVPR’05)*. Vol. 2. 2005, pp. 60–65.
- [105] Carl Zeiss X ray Microscopy Germany. *Resolution of a 3D X-ray Microscope: Defining Meaningful Resolution Parameters for XRM*. Technical Note. 2013.
- [106] H. Münstedt. *Rheological and Morphological Properties of Dispersed Polymeric Materials*. Munich: Hanser, 2016.
- [107] C. D. Han. *Rheology and processing of polymeric materials*. Vol. 1. New York: Oxford University Press, 2007.
- [108] D. Saenz-Castillo et al. “Effect of processing parameters and void content on mechanical properties and NDI of thermoplastic composites.” In: *Composites Part A: Applied Science and Manufacturing* 121 (2019), pp. 308–320.
- [109] T.M. Franke, T Ho, and C.A. Christie. “The Chi-Square Test: Often Used and More Often Misinterpreted.” In: *American Journal of Evaluation* 33 (2012), pp. 448–458.
- [110] J.M. Schultz. “Microstructural aspects of failure in semi-crystalline polymers.” In: *Polym. Eng. and Sci.* 24.10 (1984), pp. 770–785.

- [111] R. M. Heiberger and E. Neuwirth. *R Through Excel: A Spreadsheet Interface for Statistics, Data Analysis, and Graphics*. New York, NY: Springer New York, 2009, pp. 165–191.

A

Statistical Analysis

A.1

Test of Homogeneity: variability of reinforcement on composites

The Karl Pearson family of chi-square tests measures the amount that the observed counts in the samples deviate from the expected counts, according to the formula:

$$\chi^2 = \frac{\sum_{i=1}^n (\text{observed} - \text{expected})^2}{\text{expected}} \quad (\text{A-1})$$

where n is the number of cells in the table. The obtained test statistic is compared against a critical value from the chi-square distribution with $(\text{rows} - 1)(\text{columns} - 1)$ degrees of freedom (df).

Particularly, the Karl Pearson chi-square test of homogeneity determines whether two or more independent samples differ in their distributions on a single variable of interest. This test is often used to compare two or more populations (or subgroups of a population) on a categorical outcome.

The null hypothesis (H_0) states that the distribution of the categorical variable is the same for the populations (or subgroups). A low value of χ^2 is an indicator of homogeneity, while a significant value of χ^2 would indicate that the null hypothesis can not be accepted, hence the groups differ on the distribution of the variable of interest. However, the test does not indicate which of the groups are different or where the groups differ.

In the present work this test was used to determine whether the proportions of filler distribution can be considered the same across 12 equal-sized subsets in the composite samples. Two parameters were used to analyse the particle distribution: the fraction of particles in subset (ζ_p^{sub}) and the local volume fraction of particles (Φ_p^{sub}). The values for both parameters were organized in two-way tables, as the ones shown in Tab. A.1, where (Φ_{not}^{sub}) accounts for the volume fraction of the other phases present in the material, in this case the polymeric matrix and possible micro-voids. Similar tables were made for the ζ_p^{sub} parameter.

Taking the hypothesis of homogeneity into account, the expected values used for ζ_p^{sub} were $1/n$ (in this case, $1/12 = 8.33\%$). For Φ_p^{sub} the expected values used were the total volume fractions of particles (Φ_p) in each sample. The calculations

Table A.1: Two-way tables for the local volume fraction of particles in each composite sample.

Subset	90/10		80/20		70/30	
	ϕ_p^{sub}	ϕ_{not}^{sub}	ϕ_p^{sub}	ϕ_{not}^{sub}	ϕ_p^{sub}	ϕ_{not}^{sub}
t1	0.0312	0.9688	0.0602	0.9398	0.0770	0.9230
t2	0.0313	0.9687	0.0610	0.9390	0.0780	0.9220
t3	0.0328	0.9672	0.0617	0.9383	0.0791	0.9209
t4	0.0320	0.9680	0.0609	0.9391	0.0793	0.9207
m1	0.0335	0.9665	0.0642	0.9358	0.0823	0.9177
m2	0.0340	0.9660	0.0636	0.9364	0.0798	0.9202
m3	0.0327	0.9673	0.0635	0.9365	0.0847	0.9153
m4	0.0332	0.9668	0.0629	0.9371	0.0832	0.9168
b1	0.0308	0.9692	0.0601	0.9399	0.0745	0.9255
b2	0.0314	0.9686	0.0594	0.9406	0.0688	0.9312
b3	0.0288	0.9712	0.0563	0.9437	0.0755	0.9245
b4	0.0300	0.9700	0.0554	0.9446	0.0695	0.9305

were performed according to Eq. (A-1) the results are shown in Tables A.2 and A.3 for ξ_p^{sub} and Φ_p^{sub} , respectively. The p-values were obtained comparing the resulting χ^2 with the chi-square distribution with 11 degrees of freedom.

Table A.2: Test of homogeneity considering the fraction of particles in subset (ξ_p^{sub}) as measurement of filler distribution.

Sample	χ^2	p-value	H_0
90/10	0.0033	1.73E-18	accepted
80/20	0.0023	2.56E-19	accepted
70/30	0.0040	5.68E-18	accepted

Table A.3: Test of homogeneity considering the local volume fraction of particles (Φ_p^{sub}) as measurement of filler distribution.

Sample	χ^2	p-value	H_0
90/10	0.0012	7.73E-21	accepted
80/20	0.0016	4.38E-20	accepted
70/30	0.0038	3.90E-18	accepted

Considering the low values obtained for χ^2 and the p-values $\ll 0.01$, the null hypothesis can be accepted in all three cases, that is, the proportions of filler distribution are equal across the 12 subsets in all three samples. Thus, the volumetric distribution of filler can be considered as homogeneous for all the composite samples analysed.

A.2

One-way ANOVA: differences between mechanical properties

One-way analysis of variance (ANOVA) is a statistical test used to determine whether there are statistically significant differences between the means of three or more independent groups. This technique is based on the observed sample means and is a generalization of the two-sample t-test. The null hypothesis states that the means between the groups of interest are the same. While, the alternative hypothesis states that at least two group means are significantly different from each other.

If the one-way ANOVA returns a statistically significant result, i.e., a p -value that is significant at a reasonable level of significance, the null hypothesis is rejected and alternative hypothesis accepted instead.

In the present work this test was used to determine whether the mean mechanical properties between the polymer and the different composite materials were significant. In other words, the test was used to determine how likely it is that the changes in the mechanical properties of the polymer were caused by the addition of the filler and not by chance. Eight specimens of each of the four group of materials (neat polymer and 90/10, 80/20 and 70/30 composites) were tested. Thus, the degrees of freedom between and within groups were, respectively, 3 and 28. The analysis was performed using Excel and the results are listed in Tab. A.4. Since the p -values were significant for any reasonable confidence level, it can be concluded that at least two group means are statistically significantly different from each other. In other words, it is extremely unlikely that the changes in the properties observed with the incorporation of the filler happened by chance. Thus, it can be concluded that the filler did in fact alter the properties of the polymer.

Table A.4: One-way ANOVA results: significance of difference between the mean mechanical properties. Degrees of freedom between groups: 3; degrees of freedom within groups: 28.

Property	F ratio	p
Yield strength	55.53	6.58E-12
Tensile strength	138.10	6.98E-17
Strain to failure	35.12	1.26E-09
Resilience	33.23	2.29E-09
Tenacity	28.52	1.17E-08
Young Modulus	53.87	9.44E-12

A.3

One-way ANOVA: differences between creep rates

One-way ANOVA test was also used to determine whether the mean creep rate between the different composite compositions and the neat polymer were the same. Table A.5 shows the creep values obtained for each specimen.

Table A.5: Creep rate values for each specimen of each composition. Degrees of freedom between groups: 3; degrees of freedom within groups: 28.

Specimen	HDPE	90/10	80/20	70/30
S1	4.59E-06	4.34E-06	4.06E-06	4.96E-06
S2	2.15E-06	2.46E-06	4.90E-06	2.40E-06
S3	2.84E-06	3.62E-06	3.31E-06	2.59E-06
S4	4.49E-06	2.68E-06	4.84E-06	5.09E-06
S5	3.99E-06	3.74E-06	5.40E-06	2.34E-06
S6	3.31E-06	4.27E-06	9.83E-06	3.12E-06
S7	4.43E-06	3.31E-06	2.34E-06	1.68E-06
S8	2.59E-06	2.12E-06	3.49E-06	2.28E-06

The resulting F ratio and p -value were, respectively, 2.1881 and 0.1116. Thus, the null hypothesis can be accepted considering any reasonable confidence

interval. Therefore, it can be stated that the differences between the creep rate means are not statistically significant.